ANALYSIS OF THE PERFORMANCE CHARACTERISTICS OF AEROSTATIC AND HYBRID JOURNAL BEARINGS

by

EDWIN GEORGE PINK M. Phil.

A THESIS

SUBMITTED AS PARTIAL REQUIREMENTS FOR THE DEGREE OF DOCTOR OF PHILOSOPHY (C.N.A.A.)

LEICESTER POLYTECHNIC

August 1981

in Collaboration with

GENERAL ELECTRIC COMPANY, WHETSTONE

Analysis of the Performance Characteristics of Aerostatic and Hybrid Journal Bearings

by

E. G. Pink

SUMMARY

The work presented in this thesis concerns investigations into the performance characteristics of orifice compensated gas journal bearings.

Various analyses are presented which predict the pressure loss through the restrictor. The results from these analyses are compared with existing experimental data which relate to centrally fed circular thrust bearings. From this work, the significance of secondary effects which are normally neglected in the analyses, such as inertia flow and supersonic flow in the bearing film, are determined. It is shown that these effects have little impact on the overall bearing performance

A study has been made of the theoretical treatments for the prediction of the pressure loss through the clearance. The simplified one dimensional analysis is presented from which the concept of bearing optimisation is demonstrated from a mathematical standpoint. The complex potential theory has been investigated and the application to externally pressurised bearings is given. This method is used to predict the pressure loss between inlets and to demonstrate this method, streamlines and isobars for typical bearing geometries are presented. The line feed model, corrected to account for dispersion losses by using the complex potential theory, is presented. It is shown that this model provides a convenient analysis for the presentation of design data.

The finite difference method for the evaluation of film pressures is also presented. This method takes into account the discrete nature of the feeding regions and also the aerodynamic effects in hybrid bearings.

Theoretical results applicable to typical bearing configurations are presented to indicate the significance of various design parameters on both the aerostatic and hybrid modes of operation.

Throughout the thesis, theoretical results are compared with experimental data in order to deduce the accuracy and validity of the various theoretical models. This includes film pressure profiles, mass flow rates, load capacity and tilt stiffness. The experimental data used for comparison has been obtained from existing published results and from experimental data obtained from this study relating to hybrid bearings.

ACKNOWLEDGEMENTS

The Author is greatly indebted to numerous persons for their guidance and encouragement during the period of this study.

Particular gratitude is due to his supervisors, Dr. K.J. Stout and Mr. H.H. Heath (Mechanical Engineering Laboratory, G.E.C., Whetstone) for their guidance and advice given throughout the project.

Thanks are also due to Professor D.J. Picken, Head of the School of Mechanical and Production Engineering at Leicester Polytechnic, and to the Technical Staff, in particular, Mr. L.A. Tibbs, Mr. B. Burdett and Mr. A. Brown for the construction of the test rig.

The Author will always be grateful for the advice and encouragement given by numerous colleagues engaged in gas bearing research. In particular, Mr. R.W. Woolley and Mr. A.J. Munday at Southampton University and also to researchers overseas who have corresponded with the Author over a number of years. Their discussions have been both stimulating and useful.

Finally, the Author would like to thank his wife Linda, for her help in typing this thesis and also for her kind understanding and moral support throughout the period of this study.

THE AUTHOR

Mr. Pink embarked upon a career in engineering with English Electric, Luton as an engineering student apprentice in 1964. Mr. Pink obtained an Ordinary National Certificate in 1967 and a Higher National Diploma in 1970 at Luton College of Technology. Subsequent employment included C.E. Johansson Ltd., Dunstable as a trainee work study engineer and Lucas Ltd., Willesden Junction., London N.W.10.

A post was taken up in 1972 at Southampton University in the Department of Mechanical Engineering as Junior Research Fellow. The work, which had the financial backing from the Science Research Council, involved the evaluation of existing design methods for externally pressurised gas bearings. The results of this work were presented by the Author at the 1974 and 1976 International Gas Bearing Symposium at Southampton University and Cambridge University.

A move to Leicester Polytechnic followed in 1976 as Research Assistant in the School of Mechanical and Production Engineering. The research, with the financial backing of the Science Research Council, concerned investigations into gas bearing characteristics. Mr. Pink was awarded the degree of Master of Philosophy for his work on the comparison of orifice compensated and slot entry journal bearings in 1978.

LIST OF CONTENTS

LIST OF FIGURES

LIST OF TABLES

LIST OF PLATES

NOMENCLATURE

a	-	distance from orifice to edge of bearing
a'	-	distance between sources
A	-	flow area
b	-	pocket depth
b_R	-	projection of burr at edge of pocket
Cd	-	coefficient of discharge
C_d*	-	coefficient of discharge at choked conditions
CORF	-	correction factor to account for entrance loss effects
C_n	-	compressibility number $\frac{6\eta\,\omega r^2}{p_a\,h_o^2}$
d	-	inlet diameter
d_f	-	inherently compensated orifice diameter
d_o	-	pocketed orifice diameter
d_R	-	pocket diameter
D	-	bearing diameter
D_i	-	bearing inner diameter
D_o	-	bearing outer diameter
e	-	bearing/journal eccentricity
e_x	-	eccentricity along load line
e_y	-	eccentricity orthogonal to load line
e_{res}	-	resultant eccentricity
FLI	-	non-dimensional flow rate through bearing
FLO	-	non-dimensional flow rate from pocket
G	-	mass flow rate through bearing
$\overline{G}$	-	non-dimensional mass flow rate through bearing $G\frac{6\eta RT}{\pi p_o^2 h_o^3}\xi$
GA	-	axial grid spacing/circumferential grid spacing
GARI	-	flow factor for radial flow from pocket in i direction
GARJ	-	flow factor for radial flow from pocket in j direction
GARJI	-	flow factor for radial flow from pocket in i and j directions (diagonal direction)
GFI	-	non-dimensional flow in i direction
GFJ	-	non-dimensional flow in j direction
GFJI	-	non-dimensional flow in i and j directions (diagonal direction)
h	-	local film thickness

h_o - radial clearance

$\overline{h}$ - h/h_o

$\overline{H}$ - $\overline{h}^3$

i - circumferential grid position or $\sqrt{-1}$

IDIV - divisions of bearing circumference

j - axial grid position

JDIV - divisions of bearing length

JSPAN - divisions of half the bearing length

k - integer

k' - empirical factor for hybrid journal bearings

K - radial stiffness

K_A - angular stiffness

K' - loss coefficient

K_{go} - bearing pressure ratio at $\varepsilon = 0$; $\frac{p_{d_o} - p_a}{p_o - p_a}$

$\overline{K}$ - non-dimensional radial stiffness $\frac{K h_o}{LD(p_o - p_a)}$

$\overline{K_A}$ - non-dimensional angular stiffness $\frac{K_A h_o}{L^2 D^2 (p_o - p_a)}$

L - bearing length

$\dot{m}$ - mass flow rate

$\dot{m}_o$ - mass flow rate through orifice

$\dot{m}_T$ - mass flow rate through bearing

n - number of entries per row

N - total number of entries in bearing.

p - bearing film pressure

p_c - theoretical static pressure at entrance to bearing film

p_l - bearing film pressure on high clearance side

p_h - bearing film pressure on low clearance side

p_t - static pressure at throat of orifice

p_u - pressure at throat of orifice area $\pi d_f^2/4$

p* - critical pressure

P_a - ambient pressure

P_d - pressure immediately downstream of restrictor

P_{do} - pressure immediately downstream of restrictor at $\varepsilon = 0$

P_i - pressure at edge of pocket assuming purely viscous flow

P_L - equivalent line pressure (to give correct mass flow rate)

P_m - mean film pressure

P_o - supply pressure

P_p - pocket pressure

$\overline{p}$ - p/P_a

$\overline{P}$ - $\overline{p}^2$

r - radius $D/2$

r_c - critical radius for reverse transition

r' - integer

r - non-dimensional radius

R - annular thrust bearing radius

R' - relaxation factor

R_c - pitch circle radius

R_e - Reynolds' Number at entrance to bearing film

R_i - annular thrust bearing inner radius

R_o - annular thrust bearing outer radius

$\mathcal{R}$ - gas constant

T - absolute temperature

T_q - bearing torque

$\overline{T}_q$ - non-dimensional bearing torque $\dfrac{T_q}{L D^2 (p_o - p_a)}$

U - surface speed

u,v - co-ordinates in ζ plane

$\overline{v}$ - gas velocity

$\overline{v}_m$ - mean gas velocity across bearing film

$\overline{v}_t$ - gas velocity at throat of orifice

$\overline{u},\overline{v},\overline{w}$ - velocities in x,y and z directions

W - bearing load

W_A - aerodynamic load

W_A' - corrected aerodynamic load $k' W_A$

W_s - aerostatic load

$\overline{W}$ - non-dimensional bearing load $\dfrac{W}{L D (p_o - p_a)}$

x,y - co-ordinates in $\mathcal{Z}$ plane

$\overline{x},\overline{y}$ - non-dimensional co-ordinates x,y

$\mathcal{Z}$ - complex variable

z - co-ordinate

α - angle

γ - ratio of specific heats

δ_L - inherent compensation factor

$$\frac{1}{4}\left[\left(\frac{d_o^2}{d_L h}\right)^2 + \left(\frac{d_o}{b+h}\right)^2\right]^{\frac{1}{2}}$$ for pocketed orifices

$$\frac{df}{4h}$$ for inherently compensated

δ_o - inherent compensation factor at $\varepsilon = 0$

$$\frac{1}{4}\left[\left(\frac{d_o^2}{d_L h_o}\right)^2 + \left(\frac{d_o}{b+h_o}\right)^2\right]^{\frac{1}{2}}$$ for pocketed orifices

$$\frac{df}{4h_o}$$ for inherently compensated

ε - eccentricity ratio

ε_c - eccentricity ratio at bearing centreplane

ε_T - tilt eccentricity ratio

ε_{res} - resultant eccentricity ratio

ζ - complex variable

η - dynamic viscosity

θ - angle

λ - line feed correction factor $\dfrac{p_d^2 - p_a^2}{p_L^2 - p_a^2}$

$\lambda_s \xi$ - feeding parameter (see Equation 3.8)

ξ - bearing shape factor

L/D single plane admission journal bearings

2a/D double plane admission journal bearings

$\dfrac{\ln(R_o/R_i)}{2}$ annular thrust bearings

ρ - gas density

ρ_o - gas density at supply conditions

ρ_t - gas density at throat of orifice

τ - shear stress

ϕ - attitude angle

ϕ' - velocity potential

ψ - stream function

ω - angular velocity

ω' - complex potential function

PART A

INTRODUCTION

PART A - INTRODUCTION

1. INTRODUCTION

1.1 General Introduction to Gas Lubrication

1.1.1 Brief History

Since the early experimental work of the 1800's (Refs. 1.1 - 1.3), gas bearing technology has steadily progressed to the present day. Since these early pioneering days, significant progress has been made in the understanding of bearing characteristics. This has been principally due to the requirements of the nuclear power and military fields which rapidly expanded during the post-war years. More recently other industries have taken advantage of this technology. The most notable of these can be found in the field of manufacturing engineering, where air bearings have been incorporated in both process and inspection machines (Ref. 1.4). With the ever increasing requirements of higher speeds, greater accuracy and environmental awareness it is likely that gas lubrication will be more extensively used to solve the new challenges that lie ahead.

Previous work which relates to this study is referenced in the appropriate sections of this thesis.

1.1.2 Advantages

Fluid film bearings can support loads by utilising either one or a number of the load carrying properties of fluid films. For gas lubricated bearings, two main properties are used, i.e. the aerodynamic and aerostatic characteristics to support the load. Unlike liquid bearings, gas lubrication offers

relatively little squeeze film damping due to the compressibility of the gas film and consequently it is often neglected during analysis.

The main advantages that gas lubrication affords over conventional systems may be classified as follows:-

(a) Low Friction — The low viscosity of gases produces low friction losses. This allows high speeds to be obtained and also provides low static friction torque.

(b) Wide Operating Temperature Range — Gases which are used as lubricants are inherently stable over a wide temperature range and their viscosities are substantially constant.

(c) Minimal Contamination to Surroundings — In many process industries gas bearings are used in order that bearing systems do not expel lubricants detrimental to the processes with which they are being used.

(d) Averaging Action of Surface Finish and Geometric Deviations — In aerostatic bearings, this feature enables high orders of rotational accuracy to be achieved.

(e) Zero Wear — In aerostatic bearings, zero wear is experienced during running and hence infinite life is expected providing there is no wear.

1.1.3 Aerodynamic Bearings

Aerodynamic bearings generate their own internal pressure differentials due to the relative motion of their surfaces. Many types of bearings employ this principle including plain cylindrical, tilting pad bearings and foil bearings.

The major disadvantage of these bearings is that their load capacity is relatively small - of the order of a few Newtons per square centimeter of the bearing area. As these bearings only support loads at speed, their application is usually confined to operating conditions involving continual running. If many stop-start cycles are required, the bearing materials have to be chosen such that minimum wear occurs during start up and stopping. Other problems concern their manufacture. The very small running clearance to achieve the necessary aerodynamic pressures require careful manufacture and precise alignment of assemblies. Whirl instabilities can also present problems, requiring careful design in order to achieve a satisfactory bearing performance.

1.1.4 Aerostatic Bearings

Aerostatic, or externally pressurised gas bearings, require an external source of pressurised gas. Load capacity is produced from the pressure differential across the bearing achieved by the use of restrictors at the inlet of the bearing. The major disadvantage of these bearings is that an external source of pressurised gas is required. This is most commonly provided by a compressor, but sometimes gas cylinders are employed. However, all the disadvantages of aerodynamic bearings mentioned previously can be overcome by the use of the externally pressurised type. High stiffness at zero speed can be achieved. Thus the selection of bearing

materials is less critical than for those selected for aerodynamic bearings. Also, higher bearing clearances can be employed which eases their manufacturing requirements as tolerances may be relaxed. The higher bearing stiffnesses that are obtainable, aid the suppression of whirl instabilities, and also reduce bearing deflections.

The basic principles of operation of externally pressurised journal bearings are illustrated in Figure 1.1. Pressurised gas, normally air, at supply pressure P_o is fed to an annular plenum chamber around the bearing. The gas is admitted into the bearing clearance by restrictors which reduce the gas pressure to P_d at the inlet. The gas subsequently flows into the bearing clearances, its pressure reducing at atmospheric pressure P_a at the outlet of the bearing. For concentric conditions, $\varepsilon = 0$, the inlet pressures at the restrictors are normally equal and designated P_{do}.

When the bearing is loaded, an eccentricity is caused. The eccentricity leads to increased flow resistance in the low clearance side and hence lower flow through the respective restrictor. Thus the inlet pressure in the low clearance P_{d_l} increases. Conversely, in the high clearance side the inlet pressure P_{dh} decreases. The pressure differential across the bearing produces load capacity. Thus for a given loading an eccentricity is produced for which the product of bearing pressure and the projected area balances the applied loading.

The role of the restrictors is to reduce the pressure at the inlet to the bearing, and to provide bearing stiffness. These effects can be achieved by using many types of compensating devices, as classified overleaf:-

(a) Pocketed orifice

(b) Annular orifice or Inherent compensation

(c) Slot entry

(d) Restricting land

(e) Porous linear

(f) Porous plug

(g) Capillary

The present work will be confined to bearings employing orifice restrictors. These types of bearings, being the easiest to produce by established manufacturing methods, are presently used extensively in industrial applications. Other types of compensation devices are less widely employed as many manufacturing and operating problems have still to be fully resolved.

Figure 1.2 illustrates typical designs for both pocketed and annular orifices. In this case the gas is admitted at essentially point sources around the bearing circumference, usually in the range of six to sixteen entries per row. These restrictors are turbulent flow devices - the pressure drop that occurs is due to the acceleration of the gas as it expands. The pocketed orifice design shown is one using a pierced insert, press-fitted into a reamed hole to an appropriate depth below the surface of the bearing bore. The annular orifice shown is provided by simply drilling the walls of the bearing using an appropriate sized drill.

1.2 The Present Study

In Part B of this thesis, various theoretical models are presented which predict the pressure loss through both the inlet restrictor and the bearing clearance.

These theoretical models have been applied to aerostatic journal bearings in Part C and to hybrid journal bearings in Part D. This has been done to prevent repetition of the theoretical models common to both types of bearings.

In both Parts C and D, a literature review is presented and the limitations of the existing design methods indicated. Also, the results from the theoretical models are compared with each other and, where appropriate, experimental data are compared with these predictions.

PART B

ANALYSIS OF EXTERNALLY PRESSURISED GAS BEARINGS

PART B - ANALYSIS OF EXTERNALLY PRESSURISED GAS BEARINGS

2. ANALYSIS OF RESTRICTOR LOSSES

2.1 Introduction

The accurate prediction of the performance of an externally pressurised bearing is largely dependent upon the analysis employed to account for the pressure loss through the restrictor.

Various restrictor loss analyses are presented for both inherently compensated and pocketed compensated bearings. From these analyses, working equations are developed to take account of all known pressure drops from supply pressure to the boundary pressure applicable for the solution of the Reynolds' equation in the bearing film. Results from the various theoretical models are compared with each other in order to illustrate the effect of various analytical refinements. Also, experimental pressure profiles and load capacities are compared with the results from various theoretical models. From these comparisons conclusions are made concerning the validity of the analytical models. The analyses presented can be applied to any type of externally pressurised bearing which employ restrictors in the form of discrete orifices.

2.2 Isentropic Flow Through an Orifice

The equations which describe the flow through a restrictor are presented. It is assumed that isentropic (i.e. reversible adiabatic) flow occurs during the expansion of the gas from supply pressure to the throat pressure of the orifice.

The mass flow rate through an orifice can be expressed:-

$$\dot{m}_o = A \, \overline{v_t} \, \rho_t \qquad \ldots\ldots (2.1)$$

where A = flow area

$\overline{v_t}$ = velocity at the throat

ρ_t = gas density at the throat

By considering Newtons 2nd law, which equates the total force to change in momentum, leads to Euler's equation which may be defined as:-

$$\overline{v} \, d\overline{v} = - \frac{dp}{\rho}$$

Assuming that the gas expands from an initial state where the velocity may be considered negligible, Euler's equation upon integration gives:-

$$\frac{\overline{v_t}^2}{2} = - \int \frac{dp}{\rho}$$

Assuming the flow is adiabatic:

$$\frac{p}{\rho^{\gamma}} = \text{Constant}$$

gives:-

$$\frac{\overline{v_t}^2}{2} = \frac{\gamma}{\gamma - 1} \left[\frac{p_o}{\rho_o} - \frac{p_t}{\rho_t} \right]$$

The equation above shows that the kinetic energy is equal to the enthalpy drop. As an adiabatic process has been considered, and zero friction has been assumed in Euler's equation, the expansion is assumed to be isentropic.

Further substitution and rearranging gives:-

$$\overline{v_t} = \left[\frac{2\gamma}{(\gamma-1)}\frac{p_o}{\rho_o}\left\{1 - \frac{p_t}{p_o}\frac{\rho_o}{\rho_t}\right\}\right]^{1/2}$$

$$\frac{\rho_o}{\rho_t} = \left(\frac{p_t}{p_o}\right)^{-1/\gamma}$$

$$\therefore \quad \overline{v_t} = \left[\frac{2\gamma}{(\gamma-1)}\frac{p_o}{\rho_o}\left\{1 - \left(\frac{p_t}{p_o}\right)^{\frac{\gamma-1}{\gamma}}\right\}\right]^{\frac{1}{2}} \qquad \ldots\ldots (2.2)$$

Substituting Equation (2.2) into Equation (2.1) and rearranging gives:-

$$\dot{m}_o = A\,\rho_o\left[\frac{2\gamma}{(\gamma-1)}\frac{\rho_t^2}{\rho_o\rho_o}\left\{1 - \left(\frac{p_t}{p_o}\right)^{\frac{\gamma-1}{\gamma}}\right\}\right]^{\frac{1}{2}}$$

Using the identities:

$$\rho_o = \rho_o \mathcal{R} T \quad \& \quad \left[\frac{\rho_t}{\rho_o}\right]^2 = \left[\frac{p_t}{p_o}\right]^{2/\gamma}$$

Where T is the absolute temperature of the supply conditions, gives:-

$$\dot{m}_o = A\,\rho_o\left[\frac{2\gamma}{(\gamma-1)\mathcal{R}T}\left\{\left(\frac{p_t}{p_o}\right)^{2/\gamma} - \left(\frac{p_t}{p_o}\right)^{\frac{\gamma+1}{\gamma}}\right\}\right]^{\frac{1}{2}}$$

..... (2.3)

The maximum flow rate per unit area at the throat can be found by differentiating Equation (2.3) with respect to P_t and equating to zero. The resultant pressure ratio is:-

$$\frac{p_t}{p_0} = \frac{p^*}{p_0} = \left(\frac{2}{\gamma+1}\right)^{\frac{\gamma}{\gamma-1}} \quad \ldots\ldots (2.4)$$

Equation (2.4) gives the critical pressure ratio. For downstream pressures equal to and below this value, choking occurs and the static pressure at the throat is defined by Equation (2.4) . The mass flow rate then for all conditions of subsonic and supersonic flow is given by:-

$$\dot{m}_0 = A\, p_0 \left[\frac{2\gamma}{(\gamma-1)RT}\left\{\left(\frac{p_t}{p_0}\right)^{2/\gamma} - \left(\frac{p_t}{p_0}\right)^{\frac{\gamma+1}{\gamma}}\right\}\right]^{\frac{1}{2}}$$

$$\text{where } \frac{p_t}{p_0} = \left[\frac{2}{\gamma+1}\right]^{\frac{\gamma}{\gamma-1}} \text{ for choked conditions} \quad \ldots\ldots (2.5)$$

The application of Equation (2.5) with either discharge coefficients and/or other loss coefficients for gas bearings will be discussed in the following text.

2.3 Inherent Compensation

2.3.1 Introduction

The gas flow path through a typical inherently compensated restrictor is shown in Figure 2.1 with the resultant experimental pressure profile obtained by the Author (Ref. 2.1). The pressure profile shown has been obtained in the clearance of a journal bearing by traversing a pressure

transducer across an orifice. This enables pressure variations over small distances to be identified, which is particularly significant in the feeding region around the restrictor..

The pressure changes are identified and briefly discussed. Immediately under the orifice feeding area, supply pressure was recorded. This pressure corresponded exactly to that obtained from the supply conditions in the inlet manifold (Ref. 2.2), which indicated that no pressure loss occurred down the supply hole. (If the hole is made excessively long, a viscous pressure loss could be expected to occur similar to the pressure loss in capillary restrictors). At the inlet to the bearing film, the gas accelerates through the curtain area $\pi d f h$ from the supply pressure P_o and as a consequence, its static pressure reduces. In the case of choked flow with high Mach Numbers, the static pressure recorded immediately downstream of the throat can be much lower than atmospheric pressure as conventional aerothermodynamic theory indicates. As the flow continues, the gas recovers some of its static pressure and viscous losses prevail to the atmospheric boundary.

The prediction of the exact pressure profile, taking into account the pressure loss and subsequent recovery has been the subject of investigations by Mori et. al. (Refs. 2.3 - 2.5) and Poupard and Drouin (Ref. 2.6).

Vohr (Ref. 2.7) and McCabe et. al. (Ref. 2.8) proposed the use of a pressure loss coefficient derived from the results of extensive experimentation. The value of the loss coefficient was found to be dependent upon Reynolds Number at the throat of the restrictor. This approach was theoretically substantiated by the use of energy and momentum considerations by Hagerup (Ref. 2.9). Lowe (Ref. 2.10) however, demonstrated that the entrance pressure loss was also a function of bearing

clearance to orifice diameter ratio, supply pressure ratio and film entrance pressure ratio.

In the following text, various theoretical models are considered and the relevant working equations are derived.

2.3.2 The Application of Discharge Coefficients

The equations given in Section 2.2 can be used with a discharge coefficient C_d to account for the departure from the idealised flow conditions.

Equation (2.5) can be modified (with $A = \pi d f h$) thus:-

$$\dot{m}_o = \pi d f h \, C_d \, \rho_o \left[\frac{2\gamma}{(\gamma-1) RT} \left\{ \left(\frac{p_t}{p_o} \right)^{2/\gamma} - \left(\frac{p_t}{p_o} \right)^{\frac{\gamma+1}{\gamma}} \right\} \right]^{\frac{1}{2}}$$

$$\text{where } \frac{p_t}{p_o} = \left[\frac{2}{\gamma+1} \right]^{\frac{\gamma}{\gamma-1}} \text{ for choked conditions} \qquad \ldots\ldots (2.6)$$

The method of modifying the flow in this manner largely accounts for the vena contracta effect on the entrance to the bearing film as shown below:-

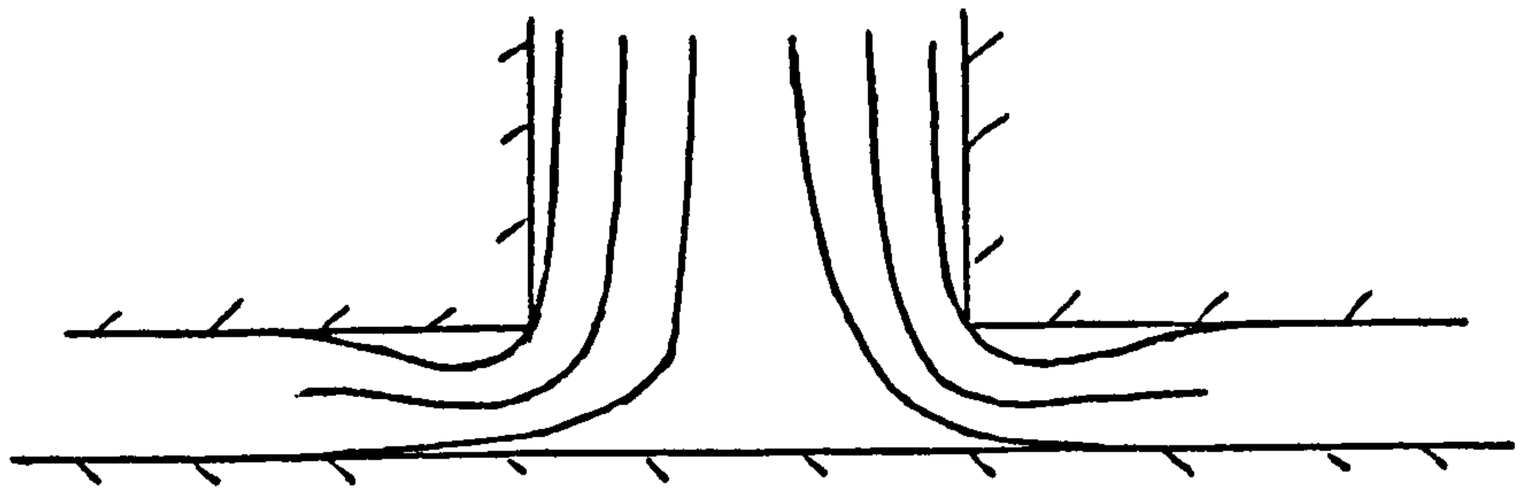

The values used for C_d are dependent upon such effects as the sharpness of the corner around which the flow passes. For exact values of C_d, experimental results of flow rate are required. In the case of the Author's experimental work relating to journal bearings (Ref. 2.2), empirical

values of C_d could only be obtained accurately for choked conditions. For unchoked flow, Equation (2.6) contains two unknowns - the value of C_d and P_t/P_o. It was found that attributing a value of P_t/P_o from pressure profiles recorded in the bearing film as shown typically by Figure 2.1 , was almost impossible due to entrance effects local to the throat. For choked conditions however, the mass flow rate is given by:-

$$\dot{m}\ (\text{choked flow}) \propto C_d^* \, \alpha_f \, h \, P_o$$

where C_d^* is the coefficient of discharge for choked conditions.

Values of C_d^* obtained experimentally by the Author are shown in Table 2.1(a) For comparison, experimental data obtained by Mori and Miyamatsu (Ref. 2.4) obtained from studies for thrust bearings have been analysed and are shown in Table 2.1(b). It can be seen that for both sets of results, the values obtained are similar for a wide range of supply pressure ratios, orifice diameters and bearing clearances. It can be seen that a typical average value for C_d^* would be in the order of 0.8. The mass flow rate for choked conditions can be adequately accounted for by the use of a discharge coefficient. However, the question arises whether or not discharge coefficients can be applied in an appopriate manner to subsonic flow conditions. A detailed discussion of this is given in following sections with reference to experimental data.

2.3.3 Pressure Losses Upstream of the Curtain Flow Area

The isentropic flow through the orifice flow area $\pi d_f^2/4$ is given by:

$$\dot{m}_o = C_d \, \frac{\pi d_f^2}{4} \, P_o \left[\frac{2\gamma}{(\gamma-1)RT} \left\{ \left(\frac{p_u}{P_o}\right)^{2/\gamma} - \left(\frac{p_u}{P_o}\right)^{\frac{\gamma+1}{\gamma}} \right\} \right]^{\frac{1}{2}} \quad \ldots\ldots (2.7)$$

where p_u = theoretical pressure at the throat of the orifice area

By equating Equations (2.7) and (2.6) , an expression relating the mass flow rate to an effective flow area and the overall pressure drop can be expressed as:

$$\dot{m}_o = \frac{C_d \pi d_f h}{\sqrt{1 + 1/\delta_L^2}} \rho_o \left[\frac{2\gamma}{(\gamma-1)RT} \left\{ \left(\frac{p_L}{p_o}\right)^{2/\gamma} - \left(\frac{p_L}{p_o}\right)^{\frac{\gamma+1}{\gamma}} \right\} \right]^{\frac{1}{2}} \quad \ldots\ldots (2.8)$$

The derivation of Equation (2.8) is given in Appendix A1 where incompressible flow has been assumed to obtain the effective flow area. It has also been assumed that the coefficient of discharge has the same value for both restrictor areas.

The parameter δ_L is the ratio of the orifice flow area $\pi d_f^2/4$ to the curtain flow area $\pi d_f h$ thus:

$$\delta_L = \frac{\pi d_f^2}{4} \frac{1}{\pi d_f h} = \frac{d_f}{4h}$$

In practice, the value of δ_L at concentric conditions is usually much greater than unity for this orifice geometry. For typical designs used the secondary restrictor has little effect on the overall flow analysis. M.T.I. for example in Reference 2.11 have not included the influence of f in their orifice flow analysis. However, its effect can be included if necessary using the above analysis.

2.3.4 The Use of Loss Coefficients

It has been suggested by Vohr (Ref. 2.7) and McCabe et.al. (Ref. 2.8) that an alternative method to using discharge coefficients in the isentropic flow equation is the use of loss coefficients. The reasoning behind this approach is that the film pressure can recover some static pressure as the flow decelerates from the throat of the restrictor as it enters the bearing film.

The analysis presented by McCabe et.al. and Vohr was to account for the pressure loss of the restrictor in the following form:-

$$p_o - p_i = K'(p_o - p_c)$$

The pressure loss of the restrictor ($P_o - P_i$) is expressed in terms of a loss coefficient (K') and the dynamic pressure at the throat ($P_o - P_c$).

The dynamic pressure is calculated assuming that the flow completely fills the bearing clearance. Thus in Equation (2.8) , $C_d = 1.0$ and $p_t = p_c$.

The value of the loss coefficient was found by experimentation to be dependent upon the Reynolds Number at the throat of the restrictor. Elrod and Glanfield (Ref. 2.12) have analysed the experimental data which relates K to R_e thus:-

$$Re \leq 2000 \; ; \quad K' = 0.16 + 0.0002\, Re$$

$$2000 < Re < 4000 \; ; \quad K' = 0.685 + 0.155y - 0.19y^2$$

$$\left(\text{where } y = \frac{Re - 3000}{2000}\right)$$

$$Re > 4000 \; ; \quad K' = 0.715$$

The Reynolds Number is calculated at the throat of the restrictor by :-

$$Re = \frac{\overline{v_t}\, \rho_t\, 2h}{\eta}$$

Substituting for $\overline{v_t}\, \rho_t = \dfrac{\dot{m}_o}{\pi d f h}$

$$Re = \frac{2\dot{m}_o}{\pi d f \eta}$$

The above analysis is used to obtain the value of P_i and hence the pressure distribution. The analysis predicts total pressures within the bearing and further refinements can be made to account for the dynamic head due to inertia effects.

2.3.5 Reverse Transition

The flow through the throat of the restrictor is turbulent whilst the flow in the bearing clearance some way downstream is laminar. Thus a change in the nature of the flow occurs. This is known as reverse transition. Flows which undergo this change are inherently unstable and defy exact analysis. However, downstream from the transition area the gas is subjected to viscous losses and the flow stabilises. The critical radius inside which reverse transition occurs has been determined by Kreith (Ref. 2.13); where

$$r_c = 0.14 \sqrt{\frac{2 \dot{m}_o h}{\eta}}$$

Substituting for Reynolds Number gives:-

$$r_c = 0.14 \sqrt{\frac{df \, Re \, h}{2}}$$

2.3.6 Choked Conditions

If a restrictor is choked both the mass flow rate per unit flow area and the throat pressure are fixed, as given by Equation (2.8) , regardless of downstream conditions.

As the gas flows from the throat into the local bearing clearance, the expansion continues, with static pressure reducing and velocity increasing.

This is given by classical aerothermodynamic theory. This expansion continues until a shock wave occurs (or a series of shocks) which changes the flow to subsonic conditions. The post-shock pressure can be predicted from the conventional aerothermodynamic theory. The pressure distribution of the expansion and the post shock pressures are shown in Figure 2.2 by curves (a) and (b) respectively. It is assumed that the expansion is adiabatic and frictionless and that a single normal shock wave occurs.

The effect of friction is to increase the supersonic pressures. Its effect is also to modify the pressure rise through a shock wave to a gradual increase rather than a step function. This has been studied by Mori and others in Refs. 2.3 and 2.5 where appropriate friction factors were used in the theoretical solutions. In Ref. 2.5 it was shown that theoretical pressure profiles correlate well with experiment both for the supersonic flow region and for the pressure rise through the shock wave.

The post shock pressure and its position are determined by the intersection of the post shock pressures and the laminar pressure distribution. This is shown in Figure 2.2 (which relates to a normal shock wave and zero friction) by the intersection of curve (b) with a typical laminar profile shown by curve (c).

2.3.7 Inertia Effects

The effect of the inertia (or kinetic energy) of the gas is to reduce static pressure. This can be evaluated by assuming a parabolic velocity distribution across the bearing film and integrating to find the total kinetic energy. This gives the pressure loss as a function of density and velocity as shown below:

$$p_{inertia} = 0.6 \rho \bar{v}_m^2 \quad \ldots\ldots (2.9)$$

where ρ is the local gas density and $\bar{v}_m$ is the mean local gas velocity

2.3.8 Comparison of Various Theoretical Models With Experiment

Figure 2.3 compares the results of various theoretical models with experimental pressure profiles obtained by Mori (Ref. 2.4) for a circular thrust bearing. Two pressure profiles are considered - one for subsonic conditions at the throat of the restrictor and one for choked conditions.

The comparison for the subsonic conditions is shown for h=29μm for which results relating to three theoretical models are shown:

1. Constant value of C_d (equal to 0.8), neglecting inertia effects.

2(i) Loss coefficient model as given by Vohr and McCabe et.al. neglecting inertia effects.

2(ii) As 2(i) with inertia effects taken into account.

It can be seen that the analysis including inertia effects [2 (ii)] correlates well with the experimental pressure profile, whilst the simplified analysis (1) give generally lower pressures.

The case for supersonic flow is shown by h=90μm. Five theoretical models are considered thus:

1. Constant value of C_d (equal to 0.8), neglecting the supersonic flow domain and inertia effects.

2(i) Loss coefficient model as given by Vohr and McCabe et.al. neglecting the supersonic flow domain and inertia effects.

2(ii) As 2(i) with account taken of the supersonic flow domain (zero friction).

2(iii) As 2(i) with account taken of the supersonic flow domain (zero friction) and inertia.

2(iv) As 2(i) with account taken of the supersonic flow domain, inertia, and friction (friction factor = 0.003).

The loss coefficient model given by Vohr and McCabe et.al. suggests that for choked flow conditions, C_d equal to unity should be used in the isentropic flow equation.

The refined analysis given by 2(ii) accounts accurately for the pressure distribution. Even greater refinement can be obtained by accounting for inertia effects and also by employing a friction factor in the analysis for the supersonic flow region as proposed by Mori and Ezuka (Ref. 2.5), as given by 2(iv).

The effects of each refinement on the theoretical load capacity are tabulated below and compared with the experimental values as deduced from the experimental pressure profiles.

Subsonic Flow Case	W Newtons
<u>Analysis</u>	
1. C_d = 0.8	180
2(i) Loss coefficient model	199
2(ii) Loss coefficient model with inertia effects	195
<u>Experiment</u>	189

Supersonic Flow Case	W Newtons
Analysis	
1. $C_d = 0.8$	27.3
2(i) $C_d = 1.0$	33.9
2(ii) $C_d = 1.0$ with account made for supersonic domain (zero friction).	29.2
2(iii) $C_d = 1.0$ with account made for supersonic domain (zero friction) and inertia effects.	26.1
2(iv) $C_d = 1.0$ with account made for supersonic domain (friction factor = 0.003) and inertia effects.	25.7
Experiment	26.5

The model which uses $C_d = 0.8$ gives better agreement for load capacity than the flow models suggested by Vohr and McCabe if both inertia and the supersonic flow region (where applicable) are neglected. The best correlation for the prediction of load capacity is obtained by the refined loss coefficient model, which takes into account both inertia and supersonic flow domain (in the case of choked flow conditions).

The inclusion of a friction factor in the analysis for the choked flow case modifies the predicted load capacity by only 2%. It can be seen that this effect is only marginal. This is because the pressure differences act over a small region compared with the overall bearing area.

2.3.9 Conclusions

It has been shown that reasonably accurate predictions of bearing performance can be obtained from either the use of discharge coefficients or from the use of loss coefficients. The two methods give substantially the same results for both load and flow rate (within 10%). This has also been found by Vohr in Ref. 2.14 (It was also shown that the results from the two theoretical models agreed well with experimental data).

For the prediction of bearing pressures, greater accuracy can be obtained by the use of the loss coefficient model taking into account inertia effects. In the case of choked flow conditions, the supersonic flow domain can be approximated by assuming zero friction. For a more exact prediction of the pressure profile for the supersonic flow domain and the subsequent shock wave profile, the theoretical analysis by Mori and Ezuka given in Ref. 2.5 can be employed using suitable friction factors. However, it has been shown that this refinement has little effect on the predicted bearing performance and probably does not justify the complexity involved, if only the performance characteristics of a bearing are required.

2.4 Pocketed Compensation

2.4.1 Introduction

The gas flow path through a typical pocket compensated restrictor is shown in Fig. 2.4 with the resultant experimental pressure profile (Ref. 2.2). The pressure profile, recorded continuously in the bearing clearance local to a pocket enables pressure variations over small distances to be identified. The pressure changes that can be observed are briefly discussed. The pressure in line with the centre of the feeding hole was found to be

slightly less than supply conditions. This is because the jet stream recovers most of its kinetic head as it impinges onto the bearing surface. In the pocket, away from the jet stream, the gas settles down to attain a pocket pressure P_p. If the flow is unchoked at the throat area $\pi d_o^2/4$, recovery can be expected, whilst if the flow is choked the nature of the pressure change is dependent upon downstream conditions. In the case of subsonic flow, the gas attains a steady state pocket pressure which is essentially at a stagnation condition. That is to say, away from the jet stream the kinetic head in the pocket is small compared to its static pressure head. At the edge of the pocket, the gas further expands through a secondary restrictor given by a curtain area $\pi d_R h$, where a vena contracta occurs as the gas enters the bearing film.

The gas subsequently recovers dynamic pressure as its velocity reduces and eventually viscous losses prevail in the bearing clearance.

2.4.2 The Application of Discharge Coefficients

The isentropic flow equation given by Equation (2.5) can be used in conjunction with a discharge coefficient C_d to account for the departure from idealised flow, where $A = \frac{\pi d_o^2}{4}$:

$$\dot{m}_o = C_d \frac{\pi d_o^2}{4} \rho_o \left[\frac{2\gamma}{(\gamma-1)RT} \left\{ \left(\frac{p_b}{p_o}\right)^{2/\gamma} - \left(\frac{p_b}{p_o}\right)^{\frac{\gamma+1}{\gamma}} \right\} \right]^{\frac{1}{2}}$$

where $\frac{p_b}{p_o} = \left[\frac{2}{\gamma+1}\right]^{\frac{\gamma}{\gamma-1}}$ for choked conditions

..... (2.10)

The mass flow rate is expressed in terms of the pocket pressure P_p, rather than the throat pressure P_t, in order to allow correlation of C_d with the experimental pressure profiles. The throat pressure P_t cannot be easily measured, whilst P_p is directly obtainable from the pressure profiles. The effect of expressing $\dot{m}$ in these terms is that C_d values obtained from experimentation by definition include the effects of pressure recovery within the pocket.

Figure 2.5 shows the experimental spread of the coefficient of discharge C_d^* at choked conditions. These results obtained by the Author (Ref. 2.2) relate to the watch-makers 'ruby' jewels by allowing the orifices to free-jet to atmospheric conditions. It was found that when the orifices were used to feed gas into a bearing clearance at choked conditions the values of C_d^* obtained were the same as those given in Figure 2.5 . The variation of C_d^* shown in Figure 2.5 for a given orifice diameter ranges between 3% and 15% and may be related primarily to deviations in orifice dimensions from the nominal values stated by the manufacturers. The mean C_d^* value ranges from approximately 0.7 to 0.9, depending upon the size of the hole diameter.

Figure 2.6 shows the dependence of C_d with P_p/P_o compared with choked flow. It can be seen that as P_p/P_o increases from the choked flow case, the coefficient of discharge reduces. Similar trends have been reported by Arnberg (Ref. 2.15), Grace et.al. (Ref. 2.16), Marsh et.al. (Ref. 2.17) and Markho et.al. (Ref. 2.18).

The correlation obtained by the Author (Ref. 2.2) is:

$$C_d = C_d^* \left[1.19 - 0.36 \left(\frac{P_p}{P_o} \right) \right] \quad \ldots\ldots (2.11)$$

When brass bushes are used, Marsh et.al. (Ref. 2.17) found that severe distortion of the hole diameter could occur when the orifices were press-fitted. The experiments conducted indicated that the coefficient of discharge could vary by a ratio of 2:1 for the same orifice sizes. A possible cause of this variation was attributed to small geometric differences and/or surface roughness effects. The value of C_d^* obtained were in the range between 0.5 and 0.92, with the trend of increasing C_d^* with increased orifice diameter. It must be noted however that the problems encountered by Marsh et.al. on the deformation of hole geometries cannot occur with watch-makers jewels. This is because the jewels,unlike brass bushes, cannot deform or burr and if excessive stresses are caused, then the jewels crack. In addition, as jewels are translucent, any cracking that occurs is easily detectable by the use of a microscope.

2.4.3 Pressure Losses Downstream of the Orifice Flow Area

Two pressure losses can occur downstream of the throat of the orifice flow area $\pi d_o^2/4$. The first occurs at the orifice curtain area $\pi d_o (b+h)$ and the second at the entrance to the bearing film flow area $\pi d_R h$. The equations which relate these pressure drops to the mass flow rate are now developed.

The isentropic flow through the edge of the pocket is given by:

$$\dot{m} = C_d \pi d_R h \rho_p \left[\frac{2\gamma}{(\gamma-1)RT} \left\{ \left(\frac{p_\ell}{p_o}\right)^{2/\gamma} - \left(\frac{p_\ell}{p_o}\right)^{\frac{\gamma+1}{\gamma}} \right\} \right]^{\frac{1}{2}} \quad \ldots\ldots (2.12)$$

where p_ℓ = theoretical static pressure at the curtain area

By equating Equations (2.10) and (2.12), an expression relating the mass flow rate to the effective flow area and the overall pressure drop can be expressed as:

$$\dot{m}_o = C_d \frac{\pi d_o^2}{4\sqrt{1+\delta_L^2}} \rho_o \left[\frac{2\gamma}{(\gamma-1)RT} \left\{ \left(\frac{p_t}{p_o}\right)^{2/\gamma} - \left(\frac{p_t}{p_o}\right)^{\frac{\gamma+1}{\gamma}} \right\} \right]^{\frac{1}{2}} \quad \ldots\ldots (2.13)$$

The derivation of Equation (2.13) is given in Appendix A1 where incompressible flow has been assumed, to obtain the effective flow area. It has also been assumed that the coefficient of discharge has the same value for both restrictor areas.

If only the orifice throat area $\pi d_o^2/4$ and the curtain flow area $\pi d_R h$ are considered the value of δ_L is defined as:

$$\delta_L = \frac{\pi d_o^2}{4} \cdot \frac{1}{\pi d_R h} = \frac{d_o^2}{4 d_R h} \quad \ldots\ldots (2.14)$$

The analysis given by the above Equations (2.13) and (2.14) is identical to that given by M.T.I. (Ref. 2.11) to account for the effective flow area and the influence this has on both the mass flow rate and the feeding parameter.

If the orifice curtain flow area $\pi d_o (b+h)$ is considered in addition to those mentioned above then the value of δ_L is given by:

$$\delta_L = \frac{1}{4}\left[\left(\frac{d_o^2}{d_R h}\right)^2 + \left(\frac{d_o}{b+h}\right)^2 \right]^{\frac{1}{2}} \quad \ldots\ldots (2.15)$$

The equation above is that given by Markho et.al. (Ref. 2.19).

2.4.4 The Use of Loss Coefficients

The entrance loss data obtained by Vohr (Ref. 2.7) and McCabe et.al. (Ref. 2.8) can be employed to account for the pressure recovery in the bearing film. To apply the data correctly, it is assumed that the flow completely fills the bearing clearance at the entrance to the bearing film. In practice, this means that the value of the coefficient of discharge at the entrance to the bearing film is considered unity. Equation (2.13) is modified in the following manner:

$$\dot{m}_o = C_d \frac{\pi d_o^2}{4\sqrt{1+\delta_L^2 C_d^2}} \rho_o \left[\frac{2\gamma}{(\gamma-1)RT} \left\{ \left(\frac{p_c}{\rho_o}\right)^{2/\gamma} - \left(\frac{p_c}{\rho_o}\right)^{\frac{\gamma+1}{\gamma}} \right\} \right]^{\frac{1}{2}} \quad \ldots\ldots (2.16)$$

where δ_L is defined by Equations (2.14) or (2.15)

The data obtained by Vohr (Ref. 2.7) and McCabe et. al. (Ref. 2.8) can be used with the assumption that the pocket pressure P_p is a stagnation pressure. This has been shown to be correct from experimental pressure profiles.

The analysis given in Section 2.3.4 can be adapted thus:

$$\rho_f - \rho_i = K'(\rho_f - p_c)$$

where $K' = f_n(Re)$

and $Re = \frac{2\dot{m}_o}{\pi d_k \eta}$

Expressing the flow through the restrictors in terms of P_i we have:

$$\dot{m}_o = (CoRF)\ C_d\ \frac{\pi d_o^2}{4}\ \rho_o \left[\frac{2\gamma}{(\gamma-1)RT}\left\{\left(\frac{p_i}{p_o}\right)^{2/\gamma} - \left(\frac{p_i}{p_o}\right)^{\frac{\gamma+1}{\gamma}}\right\}\right]^{\frac{1}{2}}$$

$$\text{where}\quad CoRF = \left[\frac{1}{1 + K' \delta_L^2 C_d^2}\right]^{\frac{1}{2}} \qquad \ldots\ldots (2.17)$$

The derivation of Equation (2.17) is given in Appendix A2.

2.4.5 Choked Conditions

If choked conditions exist in the orifice then the effects of restrictor losses, apart from C_d^*, are of little consequence in the overall bearing analysis. Unlike inherently compensated bearings, the flow through the entire film is considered as totally subsonic. Reverse transition occurs in the pocket where the flow settles down prior to entering the bearing film, with comparatively smaller entrance losses and inertia effects. The mass flow rate is fixed and can be used directly in the isothermal Reynolds' equation to calculate the pressure profile within the bearing film..

The choked flow is given by:

$$\dot{m}_o = C_d^*\ \frac{\pi d_o^2}{4\sqrt{1+\delta_L^2}}\ \rho_o \left[\frac{2\gamma}{(\gamma-1)RT}\left\{\left(\frac{p^*}{p_o}\right)^{2/\gamma} - \left(\frac{p^*}{p_o}\right)^{\frac{\gamma+1}{\gamma}}\right\}\right]^{\frac{1}{2}}$$

$$\text{where}\quad \frac{p^*}{p_o} = \left[\frac{2}{\gamma+1}\right]^{\frac{\gamma}{\gamma-1}} \qquad \ldots\ldots (2.18)$$

2.4.6 Inertia Effects

This has already been discussed in Section 2.3.7 for which the pressure loss due to inertia effects is given by Equation (2.9) . For typical bearing designs, inertia effects for pocketed orifices have less impact on the pressure profile and the load capacity than is the case for inherently compensated bearings.

2.4.7 Comparison of Various Theoretical Models with Experiment

The results from different theoretical models with varying degrees of refinements are compared with experimental data obtained by Mori and Miyamatsu (Ref. 2.4) for circular thrust bearings.

The following experimental parameters were used:-

$$2R_o/d_R = 7.5$$

$$d_o = 0.8 \text{ mm}$$

$$d_R = 8.0 \text{ mm}$$

$$b = 1.0 \text{ mm}$$

$$P_o/P_a = 3.0$$

Two clearances have been considered - one which gives choked conditions at the throat of the orifice and the other resulting in subsonic conditions.

(a) Subsonic Flow

The various theoretical models that have been considered are tabulated overleaf with the results for both theoretical and experimental load capacity. It can be seen that all the theoretical models considered give load capacities of a similar value, the variation being of the order of only 7%. The highest load capacity is for case (1) which uses the pocket

SUBSONIC FLOW CASE						W Newtons
Case	Analysis					
	Secondary pressure loss at entrance to bearing film. Equations (2.13) &(2.14)	Secondary pressure losses at orifice curtain area and at entrance to bearing film. Equations (2.13), (2.15)	Pressure recovery in bearing film. Equation (2.17)	Inertia losses accounted for. Equation (2.9)	Boundary pressure to bearing film.	
1	No	No	No	No	P_p	152
2	Yes	No	No	No	P_t	146
3	No	Yes	No	No	P_t	142
4	Yes	No	Yes	No	P_i	150
5	No	Yes	Yes	No	P_i	146
6	Yes	No	Yes	Yes	P_i	148
7	No	Yes	Yes	Yes	P_i	144
Experiment						142

pressure P_p as the boundary condition to the bearing film, as per Equation (2.10). This model neglects secondary pressure losses, pressure recovery in the bearing film and inertia losses.

Compared with the simplified analysis given by case (1), the effects of the various refinements are to reduce the theoretical load capacity.

The effect of taking into account the pressure loss at the curtain flow area $\pi d_o (b+h)$, [compare cases (2) with (3), (4) with (5), and (6) with (7)] is to reduce the theoretical load capacity by less than 3%.

The theoretical pressure profiles are compared with experiment in Figure 2.7. The theoretical results are shown for the case (1) where secondary pressure losses, pressure recovery and inertia effects are neglected, case (4) where secondary pressure losses, pressure recovery are accounted for but inertia effects are neglected and case (6) where secondary pressure losses, pressure recovery and inertia are considered.

(b) Choked Flow

The various theoretical models are tabulated overleaf with the theoretical and experimental load capacities. The various theoretical models predict load capacities to within 15% of experiment. As can be expected, the greater inertia effects are present for the case of higher clearance, although quantitively it is relatively small when compared to the overall load capacity. The effect of taking into account the pressure loss at the edge of the orifice curtain flow area $\pi d_o (b+h)$ [compare case (2) with (3), (4) with (5)] is to reduce load capacity by less than 1%.

The theoretical pressure profiles are shown in Figure 2.7 , for case (1) which neglects secondary pressure losses and inertia, case (2) which

CHOKED FLOW CASE					W Newtons
Case	Analysis				
	Secondary pressure loss at entrance to bearing film. Equations (2.18) & (2.14)	Secondary pressure losses at orifice curtain area and at entrance to bearing film. Equations (2.18), (2.15)	Inertia losses accounted for. Equation (2.9)	Boundary pressure to bearing film.	
1	No	No	No	P_p	16.0
2	Yes	No	No	P_t	15.2
3	No	Yes	No	P_t	15.1
4	Yes	No	Yes	P_t	14.0
5	No	Yes	Yes	P_t	13.9
Experiment					14.2

includes secondary pressure losses but neglects inertia, and case (4) which accounts for both secondary pressure losses and inertia.

2.4.8 Conclusions

It has been shown that the effects of the restrictors in series needs to be taken into account in the analysis of the restrictor losses. It has also been shown that the analysis which neglects pressure recovery gives results which compare well with pressure profiles and load capacity and is a valid approximation. For greater accuracy, the analysis given which includes both pressure recovery and inertia can be employed but the improvement probably would not justify the effort for typical bearing designs.

For the choked flow case, the refinement in the analysis to account for the orifice curtain area $\pi d_o(b+h)$ has been shown to have little effect on overall bearing performance. For the unchoked case, this refinement in conjunction with the secondary pressure loss gives the best agreement with experiment.

2.5 General Conclusions

The simplified analysis which employs a coefficient of discharge in the isentropic flow equation gives results which correlate well with experiment. In the case of pocketed bearings, it has been shown that the most accurate flow model is that which accounts for both the pocket curtain area $\pi d_R h$ and the orifice curtain area $\pi d_o(b+h)$. The latter flow area has the least effect on overall bearing performance.

The advantage to be gained from neglecting pressure recovery, inertia effects and supersonic flow domains is that generalised design data can be obtained. However, to account for these effects, the relevent equations

have been presented. In such cases, knowledge of many other variables is necessary such as the bearing clearance and feeding diameter in order to calculate local Reynolds' Number, inertia effects and where applicable positions of shock waves.

3. ONE DIMENSIONAL FLOW MODEL

3.1 Introduction

The early design methods for externally pressurised bearings considered that a row of orifices could be represented by a line source. This, the simplest analytical model, assumed that the number of orifices in the row is sufficiently large to approximate to a continuous line source. Such an approach was adopted in the formulation of design data presented by Tang and Gross (Ref. 3.1) and Holster (Ref. 3.2).

In this section, the analysis of the one dimensional model is presented and it is shown how bearings can be optimised to achieve a maximum stiffness condition with reference to the analysis.

3.2 Viscous Flow Analysis

The simplified line feed solution provides an idealised case for which dispersion is neglected. The results from the analysis yield the maximum load carrying capacity and stiffness conditions that can be achieved.

The basic assumptions are:

(a) The flow in the bearing clearance is assumed to be normal to the feeding plane. This implies one dimensional flow with pressure constant across the film and clearance constant throughout the bearing.

(b) For double admission bearings, the pressure between the inlet planes is assumed constant.

(c) The flow through the bearing clearance is assumed to be purely viscous without slip at the boundaries. This means that the gas inertia is neglected, a valid assumption for low Reynolds' Numbers.

The flow equations relating to the above assumptions are presented from first principles. Consider the flow element shown in Figure 3.1.

Force due to pressure on face 2zx = -2zxdP

Shear force on faces xdy = 2xdy τ

Equating forces gives:

$$\tau = -\frac{dp}{dy} \cdot z \quad \text{(shear stress)}$$

but:

$$\tau = \eta \frac{d\bar{v}}{dz}$$

Substituting gives:

$$d\bar{v} = -\frac{dp}{dy}\frac{z}{\eta}\, dz$$

Integrating across the film with $\bar{v} = 0$ at $z = h/2$ gives :

$$\bar{v} = \frac{1}{2\eta} \cdot \frac{dp}{dy}\left[\frac{h^2}{4} - z^2\right]$$

This gives a parabolic velocity distribution across the bearing film.

The mean velocity across the film is obtained by integrating the velocity profile across the film and dividing by the film thickness h to give :

$$\bar{v}_{mean} = \frac{h^2}{12\eta} \cdot \frac{dp}{dy} \qquad \ldots\ldots (3.1)$$

The mass flow rate can be expressed as:

$$\dot{m} = A \rho \overline{V}_{mean} \qquad \ldots\ldots (3.2)$$

Substituting Equation (3.1) into (3.2), assuming that the flow is isothermal (i.e. $\rho = P/RT$) and substituting A = hx :

$$\dot{m} = \frac{\rho h^3}{12 \eta R T} \cdot \frac{dp}{dy} \cdot x \qquad \ldots\ldots (3.3)$$

Introducing the boundary conditions of P_d at y = 0 and P_a at y = Y :

$$p_d^2 - p_a^2 = \frac{12 \eta R T \dot{m}}{\pi h^3} \int_0^{y=Y} \frac{2\pi}{x} dy \qquad \ldots\ldots (3.4)$$

For two sides of the inlet plane (or planes), the total mass flow rate G is given by:

$$G = 2\dot{m}$$

$$p_d^2 - p_a^2 = \frac{6 \eta R T G}{\pi h^3} \int_0^{y=Y} \frac{2\pi}{x} dy \qquad \ldots\ldots (3.5)$$

The shape factor ξ defines how the flow length dy varies with flow width x, thus :

$$\xi = \int_0^{y=Y} \frac{2\pi}{x} dy \qquad \ldots\ldots (3.6)$$

Therefore the total mass flow rate through the bearing clearance from the inlet planes to the atmospheric boundaries is given by :

$$G = \left[\left(\frac{p_d}{p_0}\right)^2 - \left(\frac{p_a}{p_0}\right)^2 \right] \frac{\pi h^3 p_0^2}{6 \eta R T \xi} \qquad \ldots\ldots (3.7)$$

3.3 Equating Flows to Evaluate P_d

The mass flow rate through an orifice is given by Equations (2.8) and (2.13). The total flow rate through all orifices in a bearing, with account made for C_d and resistances in series, is given by:

$$G = \frac{C_d \pi d_o^2}{4\sqrt{1+\delta_o^2}} N \rho_o \left\{ \frac{2\gamma}{(\gamma-1)RT} \left[\left(\frac{p_E}{\rho_o}\right)^{2/\gamma} - \left(\frac{p_E}{\rho_o}\right)^{\frac{\gamma+1}{\gamma}} \right] \right\}^{\frac{1}{2}}$$

for pocketed orifices

$$G = \frac{C_d \pi d_f h_o}{4\sqrt{1+1/\delta_o^2}} N \rho_o \left\{ \frac{2\gamma}{(\gamma-1)RT} \left[\left(\frac{p_E}{\rho_o}\right)^{2/\gamma} - \left(\frac{p_E}{\rho_o}\right)^{\frac{\gamma+1}{\gamma}} \right] \right\}^{\frac{1}{2}}$$

for inherently compensated orifices

where $\frac{p_E}{\rho_o} = \left[\frac{2}{\gamma+1}\right]^{\frac{\gamma}{\gamma-1}}$ for choked conditions

and N = total number of orifices

= n for single plane admission

= 2n for double plane admission

Equating flow rates:

$$1_s \xi C_d \left\{ \frac{2\gamma}{\gamma-1} \left[\left(\frac{p_E}{\rho_o}\right)^{2/\gamma} - \left(\frac{p_E}{\rho_o}\right)^{\frac{\gamma+1}{\gamma}} \right] \right\}^{\frac{1}{2}} = \left(\frac{p_d}{\rho_o}\right)^2 - \left(\frac{p_a}{\rho_o}\right)^2 \quad \ldots\ldots (3.8)$$

where $1_s \xi$ =

$\frac{6\eta\sqrt{RT}\, N d_o^2}{4 p_o h_o^3 \sqrt{1+\delta_o^2}} \xi$ for pocketed orifices

$\frac{6\eta\sqrt{RT}\, N d_f}{p_o h_o^2 \sqrt{1+1/\delta_o^2}} \xi$ for inherently compensated orifices

and p_t/p_o =

$\frac{p_d}{p_o}$ for subsonic flow

$\left[\frac{2}{\gamma+1}\right]^{\frac{\gamma}{\gamma-1}}$ for choked flow

3.4 Feeding Parameter $\Lambda_s\xi$ and Pressure Ratio K_{go}

The term $\Lambda_s\xi$ is commonly called the feeding parameter and has been defined by M.T.I. (Ref. 2.11). This parameter gives a measure of the ratio of the pressure drop through the orifices against the pressure drop through the bearing clearance at concentric conditions. The value indicates the degree of matching of the flow resistances. An alternative method is to express the pressure drops as K_{go} thus:

$$K_{go} = \frac{P_{do} - P_a}{P_o - P_a}$$

For a given bearing design, the calculation of $\Lambda_s\xi$ is comparatively simpler than K_{go} . Also, depending upon the restrictor loss analysis employed, differing values of K_{go} can be attributed to the same bearing. In addition, the effect of dispersion further complicates the analysis. These considerations make the selection of K_{go} for a particular bearing design an arbitrary matter. By contrast, $\Lambda_s\xi$ is defined directly from the bearing geometry and is therefore a purely independent variable.

The solution of Equation (3.8) for P_d/P_o has been obtained by numerical techniques. The computational procedure employed was the Newton-Raphson iteration. A value of P_d/P_o equal to 0.999 is initially assigned and the iteration commenced. This is done in order to ensure that numerical instabilities are prevented and that the solution converges correctly. A convergency test where values repeat to within 1×10^{-4} was found to be satisfactory in order to achieve an accurate solution.

The relationship between $\Lambda_s\xi$ and K_{go} is shown in Figure 3.2 for C_d=0.8 and γ=1.4. It can be seen that for a wide range of P_d/P_o ratios, the value of K_{go} varies only slightly for a given $\Lambda_s\xi$.

P_d/P_o is plotted against $\Lambda_s \Xi$ in Figure 3.3 , for $C_d = 0.8$ and $\gamma = 1.4$ for various supply pressure ratios.

3.5 Flow Rate

Non-dimensionalising mass flow rate to the following form:

$$\overline{G} = G \frac{6\gamma R T}{\pi P_o^2 h_o^3} \Xi$$

gives a measure of the pressure drop through the bearing film as, from Equation (3.7) , $\overline{G}$ can be expressed by:

$$\overline{G} = \left(\frac{p_d}{p_o}\right)^2 - \left(\frac{p_a}{p_o}\right)^2$$

also from Equation (3.8)

$$\overline{G} = \Lambda_s \Xi C_d \left[\frac{2\gamma}{(\gamma-1)RT}\left\{\left(\frac{p_t}{p_o}\right)^{2/\gamma} - \left(\frac{p_t}{p_o}\right)^{\frac{\gamma+1}{\gamma}}\right\}\right]^{\frac{1}{2}}$$

Figure 3.4 shows non-dimensional mass flow $\overline{G}$ plotted against $\Lambda_s \Xi$ for $C_d = 0.8$ and $\gamma = 1.4$.

Low Values of $\Lambda_s \Xi$

For choked flow $\frac{p_t}{p_o} = \left[\frac{2}{\gamma+1}\right]^{\frac{\gamma}{\gamma-1}}$ thus $\overline{G}$ is linear with $\Lambda_s \Xi$:

$$\overline{G}\ (\gamma = 1.4) = 0.685\, C_d^* \Lambda_s \Xi$$

High Values of $\Lambda_s \Xi$

$$As\ \Lambda_s \Xi \to \infty,\ \frac{p_d}{p_o} \to 1,\ \overline{G} \to \left\{1 - \left(\frac{p_a}{p_o}\right)^2\right\}$$

3.6 Stiffness

The film stiffness is primarily dependent upon the variation of P_d with h i.e. dPd / dh. A small eccentricity analysis has been performed in conjunction with the Newton Raphson iteration techniques mentioned previously. The results are shown in Figure 3.5 for a selection of P_o/P_a values. It can be seen that an optimum $\Lambda_s\xi$ exists for which the sensitivity of the orifice downstream pressure P_d (with respect to film clearance) maximises. At this optimum condition, maximum stiffness at concentric conditions would be obtained. The values shown are applicable to the one-dimensional model for which dispersion losses are neglected and therefore the values given correspond to the maximum obtainable for bearings employing orifice restrictors. The concept of optimisation is clearly demonstrated from a purely theoretical standpoint.

Maximum stiffness conditions (neglecting dispersion) are shown below for C_d = 0.8 and γ = 1.4 :-

P_o/P_a	Theoretical optimum $\Lambda_s\xi$ for maximum stiffness (neglecting dispersion)
2	0.825
3	0.817
4	0.795
5	0.778
8	0.754
10	0.747

3.6.1 The Effect of Resistances in Series on Bearing Stiffness

In Sections 2.3.3 and 2.4.3 it was shown that the effect of resistances in series was to modify the flow area as follows:

$$\frac{1}{\sqrt{1+\delta_o^2}}$$ for pocketed orifices

$$\frac{1}{\sqrt{1+1/\delta_o^2}}$$ for inherently compensated orifices

where $\delta_o = \frac{d_o^2}{4 d_R h_o}$ for pocketed orifices $(b - h_o) >> d_o$

$\delta_o = \frac{d_f}{4 h_o}$ for inherently compensated orifices

In Appendix B the analysis is given which determines the effect of δ_o on the bearing stiffness at concentric conditions. The result is that :-

$$R = \frac{K(\delta_o = 0)}{K(\delta_o \neq 0)} = \frac{1+\delta_o^2}{1+\frac{2}{3}\delta_o^2} \quad \ldots\ldots (3.9)$$

As $\delta_o \rightarrow 0$ (purely pocketed compensated) ; $R \rightarrow 1$

As $\delta_o \rightarrow \infty$ (purely inherently compensated); $R \rightarrow 3/2$

This means that bearings with pocketed orifices yield greater stiffness than those with inherently compensated orifices by a factor of up to 1.5. The exact value of this factor is given by Equation (3.9) above, and is dependent upon the orifice geometry employed. This is identical to that given by M.T.I. (Ref. 2.11)

3.7 Conclusions

The analysis presented in this section assumed a line feed model for which dispersion losses were ignored. To achieve this, an infinite number of sources are required around the feeding plane or a small groove is employed to connect the orifices. However, when discrete orifice restrictors are employed without a connecting groove, a pressure loss occurs between the inlet sources. The theory is inapplicable and the results over-estimate the bearing performance. However, the results presented for load capacity, stiffness, flow rate and downstream pressure provide a theoretical idealised solution.

4. THE APPLICATION OF COMPLEX POTENTIAL THEORY TO EXTERNALLY PRESSURISED GAS BEARINGS

4.1 Introduction

Using complex potentials, expressions can be obtained which describe the streamlines and the velocity potentials for any flow network. Typical references to this theory can be found in References 4.1 and 4.2.

In this section, potential flow theory is described and used to obtain expressions for streamlines and velocity potentials for two dimensional, compressible viscous flow. Typical bearing configurations are considered and the flow networks relating to these are illustrated.

4.2 Analysis

A complex potential ω' is an expression which describes the flow in terms of a complex variable $\mathcal{Z}$ (where $\mathcal{Z} = x + iy$). The real part of ω' gives the velocity potential ϕ' and the imaginary part gives the stream function ψ.

$$\text{i.e.} \quad \omega' = \phi'(x,y) + i\psi(x,y)$$

Consider a flow cube in rectangular co-ordinates as shown in Figure 4.1 The density at the centre is ρ and the velocities in the x, y and z directions are given by $\bar{u}$, $\bar{v}$ and $\bar{w}$ respectively. The mass flow rates per unit area are shown. The net mass outflow in the x, y and z directions are given by :

$$x \text{ direction} : \frac{\partial}{\partial x}(\rho\bar{u}) \; dx\, dy\, dz$$

$$y \text{ direction} : \frac{\partial}{\partial y}(\rho\bar{v}) \; dx\, dy\, dz$$

$$z \text{ direction} : \frac{\partial}{\partial z}(\rho\bar{w}) \; dx\, dy\, dz$$

Neglecting squeeze film terms (i.e. assuming mass inside the control volume independent of time), the total mass flow rate out of the cube for the conservation of mass is :

$$\frac{\partial(\rho\bar{u})}{\partial x} + \frac{\partial(\rho\bar{v})}{\partial y} + \frac{\partial(\rho\bar{w})}{\partial z} = 0$$

Neglecting flow in the z direction, i.e. assuming zero flow across the film thickness :

$$\frac{\partial(\rho\bar{u})}{\partial x} + \frac{\partial(\rho\bar{v})}{\partial y} = 0$$

4.2.1 Stream Function

Defining a continuous function ψ (the stream function) as :

$$\rho\bar{u} = \frac{\partial\psi}{\partial y} \quad \text{and} \quad \rho\bar{v} = -\frac{\partial\psi}{\partial x} \qquad \ldots\ldots (4.1)$$

For any flow network :

$$d\psi = \frac{\partial\psi}{\partial x}\,dx + \frac{\partial\psi}{\partial y}\,dy$$

Thus the equation of a streamline ($d\psi = 0$) is given by :

$$0 = \frac{\partial\psi}{\partial x}\,dx + \frac{\partial\psi}{\partial y}\,dy$$

which reduces to:

$$\left.\frac{dy}{dx}\right|_{\psi = \text{Constant}} = -\frac{\partial\psi/\partial x}{\partial\psi/\partial y} = \frac{\overline{v}}{\overline{u}} \qquad \ldots\ldots (4.2)$$

4.2.2 Velocity Potential and Pressure Distribution

Defining a continuous function ϕ'(velocity potential) as:

$$\rho\overline{u} = \frac{\partial\phi'}{\partial x} \quad \text{and} \quad \rho\overline{v} = \frac{\partial\phi'}{\partial y} \qquad \ldots\ldots (4.3)$$

For any flow network:

$$d\phi' = \frac{\partial\phi'}{\partial x}dx + \frac{\partial\phi'}{\partial y}dy$$

Thus the equation of constant velocity potential ($d\phi' = 0$) is given by:

$$0 = \frac{\partial\phi'}{\partial x}dx + \frac{\partial\phi'}{\partial y}dy$$

which reduces to:

$$\left.\frac{dy}{dx}\right|_{\phi' = \text{constant}} = -\frac{\partial\phi'/\partial x}{\partial\phi'/\partial y} = -\frac{\overline{u}}{\overline{v}} \qquad \ldots\ldots (4.4)$$

Comparing Equations (4.2) and (4.4) it can be seen that the slope of a streamline at any point is the negative reciprocal of the slope of the velocity potential.

For viscous flow:

$$\bar{u} \propto \frac{\partial p}{\partial x} \qquad \bar{v} \propto \frac{\partial p}{\partial y} \qquad \ldots\ldots (4.5)$$

For incompressible flow, Equations (4.3) and (4.5) gives:

$$\phi' = K_1 + K_2 p$$

$$p = K_3 + K_4 \phi'$$

For compressible, isothermal flow Equations (4.3) and (4.5) gives:

$$\frac{\partial \phi'}{\partial x} \propto \rho \frac{\partial \rho}{\partial x} \; ; \quad \frac{\partial \phi'}{\partial y} \propto \rho \frac{\partial \rho}{\partial y}$$

$$\phi' = K_1 + K_2 \rho^2$$

$$\rho^2 = K_3 + K_4 \phi' \qquad \ldots\ldots (4.6)$$

The constants K_1, K_2 , K_3, and K_4 are dependent upon the boundary conditions at the edge of the bearing, the boundary conditions at the source and upon the bearing geometry.

For both the incompressible and compressible case, lines of constant velocity potential correspond to lines of equal pressure. For incompressible flow ϕ' is linear with P whereas for compressible flow

ϕ' is linear with P^2. In practice this means that for any flow network lines of equal velocity potential can be interpreted as being either linear with pressure for incompressible flow, or linear with pressure squared for the compressible case.

Streamlines however are unaffected by compressibility. For any flow network the streamlines are identical whether the flow be incompressible or compressible.

4.2.3 Complex Potential

The combination of the stream function and the velocity potential gives the complex potential thus:

$$\omega' = \phi' + i\psi \qquad \ldots\ldots (4.7)$$

where $$\frac{d\omega'}{dz} = \frac{\partial\phi'}{\partial x} + i\frac{\partial\psi}{\partial x} = \rho(\bar{u} - i\bar{v}) \qquad \ldots\ldots (4.8)$$

To obtain the stream function and velocity potential, an appropriate expression of the complex potential ω' needs to be obtained in terms of z for particular flow networks. Subsequently, one of two methods can be employed. The first method is to differentiate ω' with respect to z and equate the real and imaginary parts with u and v respectively using Equation (4.8). The stream function ψ can then be obtained by integration of Equation(4.1) and the velocity potential ϕ' by integration of Equation (4.3).

An alternative method is to equate the real and imaginary parts of ω' with ϕ' and ψ respectively using Equation(4.7) . This method has been used in the formulation of the equations in the next sections.

4.2.4 Limitations

The analysis presented is only applicable to the case of a constant film thickness z. This is directly applicable then to the case of thrust bearings without tilt and to journal bearings at the concentric condition without tilt (no external load).

4.3 Simple Flow Arrangements

Two simple flow arrangements are considered and expressions obtained for streamlines and the velocity potential.

4.3.1 Source at Centre of Circular Thrust Bearing

The complex potential is given by:

$$\omega' = \frac{m}{2\pi} \ln(R) = \frac{m}{2\pi} \ln(x + iy)$$

where m is the source strength

The real and imaginary parts of a logarithmic function of a complex number can be found by:

$$\ln(x+iy) = \frac{1}{2} \ln(x^2+y^2) + i \tan^{-1}(y/x) \quad \ldots\ldots (4.9)$$

By using the relationship $\omega = \phi' + i\psi$

$$\phi' = \frac{m}{4\pi} \ln(x^2+y^2) \quad \text{or} \quad x^2 + y^2 = e^{\frac{4\pi}{m}\phi'}$$

$$\psi = \frac{m}{2\pi} \tan^{-1}[y/x]$$

Thus a constant velocity potential is given by circular lines at radius $e^{\frac{4\pi}{m}\phi'}$ and streamlines represented by straight lines from the centre of the source.

4.3.2 Two Sources Close to Each Other

Two point sources of equal strength m are considered which are separated by a distance a' from each other. Fluid from the two sources is admitted into a small clearance between two infinitely large rigid surfaces. The flow configuration described gives the same solution as the case of a source at a distance a'/2 from a rigid boundary by using the method of images.

The complex potential is found by superposition of flows (where $m = 2\pi$)

$$\omega' = \ln z + \ln [x - (a' - y)i]$$

$$= \ln z + \ln (z - a'i).$$

By equating real and imaginary parts:

$$\psi = \tan^{-1}(y/x) + \tan^{-1}\left(\frac{y - a'}{x}\right)$$

$$\phi' = \frac{1}{2} \ln \left\{ [x^2 + y^2] [x^2 + (y - a')^2] \right\}$$

The flow network is illustrated in Figure 4.2 and shows streamlines drawn at increments of $\pi/8$ radians around the sources and lines of constant velocity potential.

Having examined simple flow arrangements the method outlined is now extended for cases of typical bearing configurations with compressible flow. To calculate pressure levels, boundary conditions are included at the sources and at the edge of the bearing.

4.4 Single Admission Journal Bearings

The arrangement of sources and sinks which satisfies the boundary conditions is shown in Figure 4.3(a). The inlets are positioned at half stations (i.e. $a/L = 0.5$) and are shown at position $r' = 0$. To obtain the appropriate boundary conditions, rows of sinks and sources are positioned alternately as shown. Sinks are positioned at a distance $\pm L$ from the inlets ($r' = \pm 1$), sources at a distance $\pm 2L$ from the inlets ($r' = \pm 2$) and so on.

i.e. sources at $r' = 0, \pm 2, \pm 4, \ldots\ldots$

sinks at $r' = \pm 1, \pm 3, \pm 5, \ldots\ldots$

The number of sources and sinks along each line ($r' =$ constant) is considered infinite. This arrangement satisfies the boundary conditions which are that the streamlines at $x = \pm L/2$ (the edge of the bearing) intercept the boundary at right angles. Also, the journal bearing is considered as an infinitely long plate in the plane of the sources with an infinite number of sources along its length. In doing so, identical pressure distributions are obtained between adjacent sources.

Summing the complex potentials of the sources ($r' = 0, -\infty \leq k \leq \infty$) gives:

$$\omega' = \frac{m}{2\pi}\left\{\ln z + \ln\left[z^2+(a')^2\right] + \ln\left[z^2+4(a')^2\right] + \ln\left[z^2+9(a')^2\right] + \ldots\right\} \quad \ldots(4.10)$$

Equation(4.10) can be re-written by subtracting:

$$\frac{n}{2\pi}\left\{\ln\frac{a'}{\pi}+\ln(a')^2+\ln 4(a')^2+\ln 9(a')^2+\ldots\right\}$$

to give:

$$\omega' = \frac{n}{2\pi}\left\{\ln\frac{\pi z}{a}+\ln\left[1+\frac{z^2}{(a')^2}\right]+\ln\left[1+\frac{z^2}{4(a')^2}\right]+\ln\left[1+\frac{z^2}{9(a')^2}\right]\ldots\right\}$$

$$= \frac{n}{2\pi}\ln\left\{\frac{\pi z}{a'}\prod_{k=1}^{\infty}\left[1+\frac{z^2}{k^2(a')^2}\right]\right\}$$

The term: $$\frac{\pi z}{a'}\prod_{k=1}^{\infty}\left[1+\frac{z^2}{k^2(a')^2}\right] = \sinh\left[\frac{\pi z}{a'}\right] \quad \ldots\ldots (4.11)$$

The derivation of Equation(4.11) is given in Appendix C.

From sources ($r' = 0, -\infty \leq k \leq \infty$) :

$$\omega' = \frac{n}{2\pi}\ln\sinh\left[\frac{\pi z}{a'}\right]$$

By extending this method of superposition to an infinite number of lines of alternating sources and sinks as shown in Figure 4.3(a) :

$$\omega' = \frac{n}{2\pi}\sum_{r'=-\infty}^{\infty}(-1)^{r'}\ln\sinh\left[\frac{\pi}{a'}(z+\iota r')\right] \quad \ldots\ldots (4.12)$$

where $\sinh\left[\frac{\pi}{a'}(z+Lr')\right]$

$$= \sinh\frac{\pi}{a'}(x+Lr')\cos\frac{\pi}{a'}y + i\cosh\frac{\pi}{a'}(x+Lr')\sin\frac{\pi}{a'}y \quad \ldots\ldots (4.13)$$

4.4.1 Velocity Potential

Using the identities given by Equation (4.7) and (4.9) and substituting Equation (4.13) into (4.12) along with:

$$\cosh^2\frac{\pi}{a'}(x+Lr') = 1+\sinh^2\frac{\pi}{a'}(x+Lr')$$

$$\cos^2\frac{\pi}{a'}y = 1-\sin^2\frac{\pi}{a'}y$$

gives:

$$\phi' = \frac{n}{4\pi}\sum_{r'=-\infty}^{\infty}(-1)^{r'}/n\left\{\sinh^2\frac{\pi}{a'}(x+Lr')+\sin^2\frac{\pi}{a'}y\right\}$$

Further substitution of

$$2\sinh^2\frac{\pi}{a'}(x+Lr') = \cosh\frac{2\pi}{a'}(x+Lr')-1$$

$$2\sin^2\frac{\pi}{a'}y = 1-\cos\frac{2\pi}{a'}y$$

and rearranging gives:

$$\phi' = \frac{n}{4\pi}\sum_{-\infty}^{\infty}(-1)^{r'}/n\left\{\cosh\frac{\pi L}{a'}\left[\frac{x}{L/2}+2r'\right]-\cos\frac{2\pi}{a'}y\right\}$$

4.4.2 Film Pressures

From Equation (4.6) :

$$p^2 = K_3 + K_4 \phi'$$

Substituting $P = P_a$ at $x = L/2$ and $y = 0$ gives :

$$p^2 = P_a^2 - \frac{K_4 m}{4\pi} \sum_{-\infty}^{\infty} (-1)^{r'/n} \left\{ \frac{\cosh \frac{\pi L}{a'}(1+2r') - 1}{\cosh \frac{\pi L}{a'}\left(\frac{x}{L/2} + 2r'\right) - \cos \frac{2\pi}{a'} y} \right\} \quad \ldots\ldots(4.14)$$

Substituting $P = P_d$ at $x = 0$ and $y = d/2$ gives :

$$K_4 = \frac{4\pi}{m}\left(P_d^2 - P_a^2\right) \sum_{-\infty}^{\infty} (-1)^{r'/n} \left\{ \frac{\cosh \frac{\pi L}{a'}(2r') - \cos \frac{\pi d}{a'}}{\cosh \frac{\pi L}{a'}(1+2r') - 1} \right\} \quad \ldots\ldots(4.15)$$

Substituting Equation(4.15) into (4.14) gives :

$$p^2 = P_a^2 + \left(P_d^2 - P_a^2\right) \frac{\sum_{-\infty}^{\infty} (-1)^{r'/n} \left\{ \frac{\cosh N\xi(1+2r') - 1}{\cosh N\xi(\bar{x}+2r') - \cos \pi \bar{y}} \right\}}{\sum_{-\infty}^{\infty} (-1)^{r'/n} \left\{ \frac{\cosh N\xi(1+2r') - 1}{\cosh N\xi(2r') - \cos \frac{n\alpha}{\lambda}} \right\}} \quad \ldots(4.16$$

where: $N = n$, $\xi = L/D$, $\bar{x} = \frac{x}{L/2}$, $\bar{y} = \frac{2n}{\pi D} y$, $a' = \frac{\pi_D}{n}$

4.4.3 Stream Function

Using the identities given by Equations (4.7) and (4.9) and substituting Equation (4.13) into (4.12) gives :

$$\psi = \frac{n}{2\pi} \sum_{-\infty}^{\infty} (-1)^{r'} \tan^{-1} \left\{ \frac{\tan \frac{\pi}{2} \bar{y}}{\tanh \frac{N\xi}{2}(\bar{x}+2r')} \right\}$$

4.4.4 Computation

A suite of programs have been developed relating to this work. A discussion of the computation method employed is given in Section 4.7 and some examples of the computer programs used are given in Section 4.8.

4.4.5 Flow Net

Figure 4.3(b) shows the flow network as a result of the above analysis. The bearing parameters relating to the flow network shown are:-

$$L/D = 1$$

$$a/L = 0.5$$

$$n = 6$$

$$P_d/P_a = 5$$

$$nd/D = 0.1$$

Figure 4.3(b) has been plotted by an X-Y plotter under the control of a computer so that errors and resultant distortion due to the quantization levels are minimised. Although the flow net is symmetrical about both centre lines, the total flow net has been drawn for one complete source. This has been done to present a clearer picture of the flow configuration to the reader. In practice only one quarter of the net is necessary.

Streamlines are illustrated at every $\pi/12$ radians around the source. The transformation of purely radial flow from the source to axial flow at the outer edges is clearly demonstrated. Isobars are drawn every 0.2 P_a from the source to the edge of bearing. The isobars can be seen to change from circles at the source, transforming to a form that becomes parallel with the edge of the bearing.

4.5 Annular Thrust Bearing

The geometry of the bearing is shown in Figure 4.4. The number of holes are equally-spaced on a pitch circle radius R_c where:-

$$R_c = \sqrt{R_o R_i}$$

For this condition minimum flow occurs. Unlike the previous example where sources and sinks were taken directly from the bearing geometry, a conformal transformation is applied to obtain a rectangular mesh of source and sink arrangements.

The appropriate conformal transformation necessary is:-

$$\zeta = h(z)$$

where $\zeta = u + iv$; $Z = x + iy$

This transforms the complex variable z into another complex variable ζ and is shown graphically in Figure 4.5 .

The transformation gives:-

$$u = \ln(R) \quad ; \quad v = \theta$$

$$\text{where} \quad R = \sqrt{x^2 + y^2} \quad ; \quad \theta = \tan^{-1}(y/x)$$

Therefore a source positioned in the Z plane at $R = R_c$, and at $2\pi/n$ with the x axis transforms to $u = \ln(R_c)$ and $v = 2\pi/n$ in the ζ plane.

$R_c - R_i$ transforms to $\ln(R_c/R_i) = \xi$

$R_o - R_c$ " $\ln(R_o/R_c) = \xi$

The solution is now similar to the case of the single admission journal bearing dealt with previously. The arrangement of sources and sinks which satisfy the boundary conditions is shown in Figure 4.6(a).

By the method of sources and sinks

$$\omega' = \frac{n}{2\pi} \sum (-1)^{r'} \lambda \sin\lambda \frac{\pi}{2} \left[\xi - \ln R_c + 2r'\xi \right] \quad \ldots\ldots (4.17)$$

4.5.1 Velocity Potential

Using Equation (4.17) with the identities given by Equations (4.7) and (4.9) and rearranging gives:-

$$\phi' = \frac{n}{4\pi} \sum_{-\infty}^{\infty} (-1)^{r'} \lambda \left\{ \sin\lambda^2 \frac{\pi}{2} \left(\ln \frac{R'}{R_c} + 2r'\xi \right) + \sin^2 \frac{\pi}{2} \bar{\theta} \right\}$$

Further substitution gives:-

$$\phi' = \frac{n}{4\pi} \sum_{-\infty}^{\infty} (-1)^{r'} \lambda \left\{ \cos\lambda N\xi \left[\frac{\ln (R'/R_c)}{\xi} + 2r' \right] - \cos \pi\bar{\theta} \right\}.$$

4.5.2 Film Pressures

Substituting the boundary conditions:

$$P = P_a, \qquad R = R_o, \qquad \bar{\theta} = 0$$

$$P = P_d, \qquad R = R_c, \qquad \bar{\theta} = \frac{dn}{2R_c\pi}$$

$$P^2 = P_a^2 + (P_d^2 - P_a^2) \frac{\sum_{-\infty}^{\infty} (-1)^{r'} \lambda \left\{ \dfrac{\cos\lambda N\xi (1+2r') - 1}{\cos\lambda N\xi (\bar{r} + 2r') - \cos \pi\bar{\theta}} \right\}}{\sum_{-\infty}^{\infty} (-1)^{r'} \lambda \left\{ \dfrac{\cos\lambda N\xi (1+2r') - 1}{\cos\lambda N\xi (2r') - \cos \dfrac{n\alpha}{2}} \right\}} \quad \ldots(4.18)$$

where: $N = n$, $\xi = \dfrac{\ln(R_o/R_i)}{2}$, $\bar{r} = \dfrac{\ln (R/R_c)}{\xi}$, $\bar{\theta} = \dfrac{n\theta}{\pi}$, $D = 2R_c$

4.5.3 Stream Function

Using Equation (4.17) with the identities given by Equations (4.7) and (4.9) and rearranging gives:-

$$\psi = \frac{n}{2\pi} \sum_{-\infty}^{\infty} (-1)^{r'} \tan^{-1} \left\{ \frac{\tan \bar{r}/2 \; \bar{\theta}}{\tanh \frac{n\xi}{2} (\bar{r} + 2r')} \right\}$$

The form of the equations which describe the streamlines and isobars are similar in form to that obtained for the single admission journal bearing. The only difference is that non-dimensional angle $\bar{\theta}$ replaces non-dimensional distance $\bar{y}$ and non-dimensional radius $\bar{r}$ replaces non-dimensional distance $\bar{x}$.

4.5.4 Computation

A discussion of the computation method employed is given in Section 4.7 and some examples of the computer programs used are given in Section 4.8.

4.5.5 Flow Net

Figure 4.6(b) shows the resultant flow network as a result of the above analysis for the following bearing parameters:

$$R_o/R_i = 2$$

$$n = 12$$

$$P_d/P_a = 5$$

$$n/2R_c = 0.2$$

Figure 4.6(b) has been plotted by a computer on an X-Y plotter so that drawing errors are minimised. The total flow net applicable to one complete source is shown, although it is symmetrical about a radial centreline as in the previous example. Again, this has been done to

present to the reader a complete picture of the flow from one source. Streamlines are illustrated every $\pi/12$ radians around the source. In this case, the radial flow from the source transforms to radial flow both towards or away from the centre of the bearing as it approaches the outer edges.

4.6 Double Admission Journal Bearing

Figure 4.7(a) shows the arrangement of sources and sinks which satisfy the boundary conditions for any a/L ratio. Two rows of inlets are positioned at a distance 'a' from the edge towards the centre of the bearing. To obtain the necessary boundary conditions, pairs of sources and sinks are positioned alternately from the inlet planes as shown.

By the method of sources and sinks as before:

$$\omega' = \frac{m}{2\pi} \sum (-1)^r \left\{ \ln \sin L\left[Z + r'L - \frac{L}{2} + a \right] + \ln \sin L\left[Z + r'L + \frac{L}{2} - a \right] \right\} \quad \ldots\ldots (4.19)$$

4.6.1 Velocity Potential

Using Equation (4.19) with the identity given by Equations (4.7) and (4.9) and rearranging gives:-

$$\phi' = \frac{m}{4\pi} \sum_{-\infty}^{\infty} (-1)^{r'} \left\{ \ln \left[\cos L \frac{\pi L}{D} \left(\bar{x} + 2r' - 1 + \frac{2a}{L} \right) - \cos \pi \bar{y} \right] + \ln \left[\cos L \frac{\pi L}{D} \left(\bar{x} + 2r' + 1 - \frac{2a}{L} \right) - \cos \pi \bar{y} \right] \right.$$

4.6.2 Film Pressures

Substituting the boundary conditions:

$$p = p_a, \quad \bar{x} = 1 \quad ; \quad \bar{y} = 0$$

$$p = p_d, \quad \bar{x} = 1 - \frac{2a}{L}, \quad \bar{y} = \frac{d_n}{\pi D}$$

gives:

$$p^2 = p_a^2 + (p_d^2 - p_a^2) \frac{\sum_{-\infty}^{\infty} (-1)^{r'} (X - Y)}{\sum_{-\infty}^{\infty} (-1)^{r'} (X - Z)} \quad \ldots\ldots (4.20)$$

where $X = \ln \left\{ \cosh \frac{n L}{D} \left[2r' + \frac{2a}{L} \right] - 1 \right\}$

$$+ \ln \left\{ \cosh \frac{n L}{D} \left[2r' + 2 - \frac{2a}{L} \right] - 1 \right\}$$

$$Y = \ln \left\{ \cosh \frac{n L}{D} \left[\bar{x} + 2r' - 1 + \frac{2a}{L} \right] - \cos \pi \bar{y} \right\}$$

$$+ \ln \left\{ \cosh \frac{n L}{D} \left[\bar{x} + 2r' + 1 - \frac{2a}{L} \right] - \cos \pi \bar{y} \right\}$$

$$Z = \ln \left\{ \cosh \frac{n L}{D} (2r') - \cos \frac{n d}{D} \right\}$$

$$+ \ln \left\{ \cosh \frac{n L}{D} \left(2r' + 2 - \frac{4a}{L} \right) - \cos \frac{n d}{D} \right\}$$

4.6.3 Stream Function

Using Equations (4.19),(4.7) and (4.9) with rearranging gives:

$$\psi = \frac{n}{2\pi} \sum_{-\infty}^{\infty} (-1)^{r'} \left\{ \tan^{-1} \left[\frac{\tan \frac{\pi}{2} \bar{y}}{\tanh \frac{n L}{D} \left(\bar{x} + 2r' - 1 + \frac{2a}{L} \right)} \right] \right.$$

$$\left. + \tan^{-1} \left[\frac{\tan \frac{\pi}{2} \bar{y}}{\tanh \frac{n L}{D} \left(\bar{x} + 2r' + 1 - \frac{2a}{L} \right)} \right] \right\}$$

4.6.4 Computation

A discussion of the computation method is given in Section 4.7 and some examples of computer programs used are given in Section 8.

4.6.5 Flow Net

Figure 4.7(b) shows the resultant flow network as a result of the above analysis. The bearing parameters relating to the flow network shown in Figure 4.7(b) are:-

$L/D = 1$

$a/L = 0.25$

$n = 6$

$P_d/P_a = 5$

$nd/D = 0.1$

Similar to Figures 4.6(b) and 4.3(b) , Figure 4.7(b) has been plotted using a computer to drive an X-Y plotter to minimise drawing errors. The flow net applicable to an axial segment is shown and shows symmetry about the axial bearing centreline and the centreline through the sources.

Streamlines are illustrated at increments of $\pi/12$ radians around the sources and isobars are shown every 0.2 P_a from the source to the edges of the bearing. The isobars take a similar form to those discussed previously.

4.7 Computation

The question arises of how many summing terms are necessary to approximate closely to the equations given. In order to preserve the symmetry of the arrangement of sources and sinks, the ends of the series chosen must be a source in the case of a single row of inlets or a pair of sources for two plane admission.

Mori and Yabe (Ref. 4.3) suggest that for annular thrust bearings most cases can be solved by using only the $r' = 0$ term. Lund (Ref. 4.4) also suggests that only the $r' = 0$ term is significant for single admission journal bearings if $d/D \ll 1$. It has been found that this approximation is not adequate for the ranges below:-

$$1 \leqslant N\xi \leqslant 100$$

$$0.01 \leqslant nd/D \leqslant 1$$

Figure 4.8 shows the calculated pressure in line with the orifices ($\bar{x} = 0$) at a position half-way between them ($\bar{y} = 1$), for single admission journal bearings as per Equation (4.16). It can be seen that as $N\xi$ reduces more terms are necessary to achieve satisfactory convergence. It has been found that an adequate range for the number of terms is $r' = \pm 6$. For this number of terms, the values obtained for the film pressure converge to at least eight decimal places over the entire ranges given above for a source pressure of 5 atmospheres.

4.8 Computer Programs

A suite of computer programs have been developed for this work and are listed below:

CP1 - Calculates film pressures for single or double plane admission.

Input : $N\xi$, a/L, nd/D, P_d/P_a, $\bar{x}$, $\bar{y}$

Output: Film pressure

CP2 - Calculates $\bar{y}$ at the intersection of an isobar with the $\bar{x}$ axis for single admission bearings.

Input : $N\xi$, nd/D, P_d/P_a, film pressure

Output: $\bar{y}_{max}$

CP3 - Plots isobars and streamlines for single admission bearings.

Input : $N\xi$, nd/D, P /P , $\overline{y}$ from CP2, L/D or R_o/R_i, L or R_i

Output: Streamlines at increments $\pi/12$ and isobars at increments $0.2P_a$

CP4 - Plots isobars and streamlines for double admission bearings.

Input : $N\xi$,nd/D , P_d/P_a, a/L, L/D, L

Output: As per CP3

4.8.1 Computer Program for Plotting Isobars and Streamlines

To demonstrate the techniques employed, the computer program CP3 is described. For plotting both the streamlines and the isobars, iterative methods have been used to find co-ordinates $\overline{x}$ and $\overline{y}$ for particular values of either ψ or pressure.

Figure 4.9 shows the flow chart applicable to a single admission bearing (either journal or collar thrust) and demonstrates the method used. A given streamline (ψ = constant) is defined by α, the angle subtended by the streamline with the $\overline{x}$ axis. For this streamline, $\overline{x}$ is incremented and the corresponding values of $\overline{y}$ are calculated and stored in an array until the boundary is reached. A plotting subroutine is called and the streamline is plotted. The streamline is mirrored about the $\overline{x}$ axis and $\overline{y}$ axis as appropriate.

In the case of an isobar, its shape can either be a closed form around the inlet or a form nominally parallel with the bearing boundary. The intersection of the $\overline{y}$ axis as calculated by CP2 defines the range for which corresponding values of $\overline{x}$ are calculated for the isobars. If the isobar

does not intersect the $\bar{y}$ axis, values of $\bar{x}$ are required for the complete width i.e. $\bar{y} = 0 \rightarrow 1$. The values of $\bar{x}$ and $\bar{y}$ are stored in an array and are plotted in a similar manner as that described for the streamlines.

The iterative method employed is the Newton Raphson iteration. To illustrate this method, the equations derived relating to a single admission journal bearing are given below.

For a given streamline (ψ = constant) and $\bar{x}$:

$$(\bar{y}\pi)_{NEW} = (\bar{y}\pi)_{OLD} - \frac{Y}{dY/d(\bar{y}\pi)}$$

where $$Y = \psi - \sum_{-\infty}^{\infty} (-1)^{r'} \tan^{-1} \left\{ \frac{\tan \pi/2\, \bar{y}}{\tanh(P3)} \right\}$$

$$\frac{dY}{d(\bar{y}\pi)} = \sum_{-\infty}^{\infty} (-1)^{r'} \frac{\sec^2 \pi/2\, \bar{y}}{2 \tanh(P3) \left\{ 1 + \frac{\tan^2 \pi/2\, \bar{y}}{\tanh^2(P3)} \right\}}$$

$$P3 = \frac{N\xi}{2} (\bar{x} + 2r')$$

For a given pressure (ϕ' = constant) and $\bar{y}$:

$$(\bar{x})_{NEW} = (\bar{x})_{OLD} - \frac{K}{dk/d(\bar{x})}$$

where $$K = \frac{\rho^2 - \rho_a^2}{\rho_d^2 - \rho_a^2} - \frac{\sum_{-\infty}^{\infty} (-1)^{r'}/n \left\{ \frac{\cosh N\xi(1+2r') - 1}{\cosh N\xi(\bar{x}+2r') - \cos n\bar{y}} \right\}}{\sum_{-\infty}^{\infty} (-1)^{r'}/n \left\{ \frac{\cosh N\xi(1+2r') - 1}{\cosh N\xi(2r') - \cos \frac{n\alpha}{\beta}} \right\}}$$

$$\frac{dK}{d\bar{x}} = \frac{\sum_{-\infty}^{\infty} (-1)^{r'} \frac{N\xi \sinh N\xi(\bar{x}+2r')}{\cosh N\xi(\bar{x}+2r') - \cos \pi\bar{y}}}{\sum_{-\infty}^{\infty} (-1)^{r'} \ln \left\{ \frac{\cosh N\xi(1+2r') - 1}{\cosh N\xi(2r') - \cos \frac{n\alpha}{D}} \right\}}$$

A full listing of the computer program CP3 used for plotting the streamlines and isobars is given in Appendix D.

4.8.2 Hyperbolic Functions

Cosh and sinh terms appear frequently in the computation. Often it is required to find the cosh and sinh of large numbers (> 50) which result in very large numbers ($> 2 \times 10^{21}$). To prevent overflow in the computer the following approximations were used where B > 50.

$$\left.\begin{array}{l} \operatorname{csch}^2(B) = 0.0 \\ \ln\{\cosh B - 1\} \\ \ln\{\cosh B - \cos \pi\bar{y}\} \\ \ln\{\cosh B - \cos \frac{n\alpha}{D}\} \end{array}\right\} B - \ln 2$$

$$\frac{N\xi \sinh B}{\cosh B - \cos \pi\bar{y}} = N\xi$$

These approximations give very little error. Using a desk scientific calculator, which gives numerical values down to 10^{-100} the calculated errors are zero.

4.9 Conclusions

The use of complex potential theory provides a means to obtain analytically the film pressures within a fluid film bearing. The examples considered were the single and double admission journal bearings as well as annular thrust bearings.

The results from the complex potential theory provide a means to test approximate theoretical models, where tilt or non-parallel surfaces are excluded. These tests are conducted in preceding sections for the results obtained by the finite difference solution for journal bearings at $\varepsilon = 0$.

5. LINE FEED SOLUTION CORRECTED TO ACCOUNT FOR DISPERSION

5.1 Introduction

The one dimensional flow model presented in Section 3 is now extended to account for the dispersion losses that occur between the discrete sources, as shown in Figure 5.1. By the use of complex potential theory it is shown how an appropriate line feed correction factor can be deduced from the salient bearing parameters. As a consequence of the dispersion losses that occur, it is shown how bearing performance is derated from the results applicable to the one dimensional model.

The method used is that which has been previously suggested by Lund (Ref. 4.4) for journal bearings and from which the design data presented by M.T.I. (Ref. 2.11) is based. This method involves relating the line source pressure P_L to the orifice downstream pressure P_d, as shown in Figure 5.1 , by the factor $\frac{1}{\lambda}$ thus:-

$$\frac{1}{\lambda} = \frac{\rho_L^2 - \rho_a^2}{\rho_d^2 - \rho_a^2} \quad \ldots\ldots (5.1)$$

5.2 Determination of $1/\lambda$ Factor

To obtain the value of $1/\lambda$ for a given bearing geometry, use is made of the equations derived from the complex potential theory given in Section 4. The pressure distribution around an inlet circumference for the case of a single admission journal bearing is considered.

Equation (4.16) is written, with $\overline{x} = 0$, as:-

$$\rho^2 - P_a^2 = (P_d^2 - P_a^2) \frac{\sum_{-\infty}^{\infty} (-1)^{r'} I_n \left\{ \frac{\cosh N\xi(1+2r') - 1}{\cosh N\xi(2r') - \cos \pi \bar{y}} \right\}}{\sum_{-\infty}^{\infty} (-1)^{r'} I_n \left\{ \frac{\cosh N\xi(1+2r') - 1}{\cosh N\xi(2r') - \cos \frac{n\alpha}{D}} \right\}}$$

..... (5.2)

Substituting the average value of $P^2 - P_a^2$ for the plane $\overline{x} = 0$, Equation (5.2) is written as:-

$$\frac{I}{\lambda} = \int_{\frac{n\alpha}{\pi D}}^{1} \frac{\sum_{-\infty}^{\infty} (-1)^{r'} I_n \left\{ \frac{\cosh N\xi(1+2r') - 1}{\cosh N\xi(2r') - \cos \pi \bar{y}} \right\}}{\sum_{-\infty}^{\infty} (-1)^{r'} I_n \left\{ \frac{\cosh N\xi(1+2r') - 1}{\cosh N\xi(2r') - \cos \frac{n\alpha}{D}} \right\}} \, d\bar{y}$$

$$+ \frac{n\alpha}{\pi D} \qquad \text{.....(5.3)}$$

5.2.1 Approximate Solution

Lund (Ref. 4.4) suggests that if $d/D \ll 1$, only the first term of the series given by Equation (5.3) (i.e. $r' = 0$) is significant. The integral becomes:

$$\frac{I}{\lambda} \simeq \frac{I_n(\cosh N\xi - 1) - \int_0^1 I_n(1 - \cos \pi \bar{y})}{I_n(\cosh N\xi - 1) - I_n(1 - \cos \frac{n\alpha}{D})}$$

$$\simeq \frac{I_n(\cosh N\xi - 1) + I_n 2}{I_n(\cosh N\xi - 1) - I_n(1 - \cos \frac{n\alpha}{D})}$$

Furthermore, if $N\Sigma \geq 3$ then

$$\ln(\cosh N\Sigma - 1) + \ln 2 \simeq N\Sigma$$

with an error of less than 4%

$$\therefore \frac{1}{\lambda} \simeq N\Sigma \ln\left\{\frac{1-\cos \pi d/D}{\cosh N\Sigma - 1}\right\} \quad \ldots\ldots (5.4)$$

The above equation is that quoted by Lund in Ref. 4.4 , and gives an approximate value of $1/\lambda$ factor. The design charts given by M.T.I are based on the line feed correction factor $1/\lambda$ equal to 0.67.

5.2.2 More Exact Solution

A more exact value has been calculated from Equation (5.3) . Small increments $\Delta\bar{y}$ were considered and for each value of $\Delta\bar{y}$ the value of $\Delta(1/\lambda)$ was calculated for r' in the range ± 6. These values were then summed by numerical integration to give $1/\lambda$. The values of $1/\lambda$ used by M.T.I. and that from the computation are shown in Figure 5.2. It can be seen that for $N\Sigma < 8$ or for $\pi d/D > 0.2$, the error incurred by the use of Equation (5.4) becomes significant.

Due to the similarity of the equations derived from the complex potential theory, the values shown in Figure 5.2 apply for single admission journal, annular thrust and double admission journal bearings.

A point of note is that M.T.I. in their Figure 5.5.17 plot $N\Sigma$ against $d/\Sigma D$ for $1/\lambda$ = 0.67. In Figure 5.2 , $N\Sigma$ is plotted against $\pi d/D$. This has been arranged in order to improve the presentation, as will become evident in subsequent sections.

5.3 Effect of $1/\lambda$ on Performance

Assuming viscous, isothermal flow, as given by Equation (3.7) , but now defining the pressure around the inlet plane as a line pressure P_L, the flow through the bearing clearance is given by:

$$G = \left[\left(\frac{\rho_L}{\rho_o}\right)^2 - \left(\frac{\rho_a}{\rho_o}\right)^2\right] \frac{\pi L^3 \rho_o^2}{6\eta R T \xi} \quad \ldots\ldots (5.5)$$

Substituting for P_d^2 from Equation (5.1) :-

$$G = \left[\left(\frac{\rho_d}{\rho_o}\right)^2 - \left(\frac{\rho_a}{\rho_o}\right)^2\right] \frac{\pi L^3 \rho_o^2}{6\eta R T \xi \lambda}$$

The effect of $1/\lambda$ upon the mass flow rate and P_d/P_o is shown in Figure 5.3 . As $1/\lambda$ decreases, P_d/P_o increases and mass flow rate reduces. Also from Equation (5.5) , P_L/P_o reduces, which in turn leads to a reduced load capacity.

Equating the mass flow rate through the orifices with that through the bearing clearance gives:-

$$1_S \xi\ C_d \left\{\frac{2\gamma}{\gamma-1}\left[\left(\frac{p_t}{\rho_o}\right)^{2/\gamma} - \left(\frac{p_t}{\rho_o}\right)^{\frac{\gamma+1}{\gamma}}\right]\right\}^{\frac{1}{2}} = \left(\frac{\rho_L}{\rho_o}\right)^2 - \left(\frac{\rho_a}{\rho_o}\right)^2$$

$$= \frac{1}{\lambda}\left[\left(\frac{\rho_d}{\rho_o}\right)^2 - \left(\frac{\rho_a}{\rho_o}\right)^2\right] \quad \ldots\ldots (5.6)$$

where $$\frac{p_t}{\rho_o} = \left[\frac{2}{\gamma+1}\right]^{\frac{\gamma}{\gamma-1}}$$ for choked orifices

$$\frac{p_t}{\rho_o} = \frac{\rho_d}{\rho_o}$$ for unchoked orifices

Figure 5.4 shows P_d/P_o and P_L/P_o plotted against $\lambda_s \xi$ for various $1/\lambda$ with $P_o/P_a = 5$. It can be seen that as $\lambda_s \xi$ increases, greater disparity occurs between P_L/P_o and P_d/P_o.

With reference to Figure 5.4 :

$$As \quad \lambda_s \xi \longrightarrow \infty$$

$$\frac{\rho_d}{\rho_o} \longrightarrow 1$$

$$\frac{\rho_L}{\rho_o} \longrightarrow \sqrt{\left(\frac{\rho_a}{\rho_o}\right)^2 \left[1 - \frac{1}{\lambda}\right] + \frac{1}{\lambda}}$$

At low values of $\lambda_s \xi$ (choked orifices);

$$\frac{\rho_d}{\rho_o} = \sqrt{0.685\, C_d^* \lambda\, \lambda_s \xi + \left(\frac{\rho_a}{\rho_o}\right)^2}$$

$$\frac{\rho_L}{\rho_o} = \sqrt{0.685\, C_d^*\, \lambda_s \xi + \left(\frac{\rho_a}{\rho_o}\right)^2}$$

5.3.1 Flow Rate

Non-dimensionalising flow in the following form:

$$\overline{G} = G \, \frac{6 \gamma R T \xi}{\pi \rho_o^2 L_o^3}$$

$$\overline{G} = \left(\frac{\rho_L}{\rho_o}\right)^2 - \left(\frac{\rho_a}{\rho_o}\right)^2 = \frac{1}{\lambda}\left[\left(\frac{\rho_d}{\rho_o}\right)^2 - \left(\frac{\rho_a}{\rho_o}\right)^2\right]$$

Figure 5.5 shows results of $\overline{G}$ against $\Lambda_s\xi$ for various $1/\lambda$. It can be seen that as $\Lambda_s\xi$ increases, the effect of $1/\lambda$ on flow rate becomes more significant.

To summarise:-

As $\Lambda_s\xi \longrightarrow \infty$.

$$\bar{G} \longrightarrow \frac{1}{\lambda}\left[1-\left(\frac{\rho_a}{\rho_s}\right)^2\right]$$

At low values of $\Lambda_s\xi$ (choked orifices):

$$\bar{G} \longrightarrow 0.685\ C\alpha^*\ \Lambda_s\xi \quad \text{(i.e. independent of } 1/\lambda\text{)}$$

5.3.2 Load Capacity

The effect of $1/\lambda$ on load capacity can be demonstrated by considering a single acting annular thrust bearing where parallel film conditions exist. The load capacity would follow the trend shown by curves of P_L/P_o in Figure 5.4 . At low values of $\Lambda_s\xi$ little difference exists but as $\Lambda_s\xi$ increases, the effect of $1/\lambda$ becomes more pronounced.

5.3.3 Stiffness

The film stiffness is largely dependent upon dP_L/dh. To demonstrate the effect of $1/\lambda$ upon the bearing stiffness, a small eccentricity analysis has been made to determine the film pressure response dP_L/dh. The results are shown in Figure 5.6 . It can be seen that as $1/\lambda$ decreases, the maximum obtainable dP_L/dh reduces significantly, which would result in lower bearing stiffness accordingly. Also of note is that the effect of reducing the value of $1/\lambda$ (increasing dispersion) is to

reduce the optimum $\Lambda_s \xi$ for maximum dP_I/dh (and stiffness) conditions. The optimum values of $\Lambda_s \xi$ are tabulated below:-

P_o/P_a	Λ				
	1.0	0.8	0.6	0.4	0.2
2	0.825	0.674	0.519	0.358	0.188
3	0.817	0.665	0.512	0.354	0.189
4	0.795	0.645	0.494	0.340	0.182
5	0.778	0.630	0.480	0.329	0.175
8	0.754	0.607	0.459	0.311	0.162
10	0.747	0.600	0.453	0.305	0.155

For typical values of Λ used in practice, the optimum feeding parameter for maximum stiffness would be in the range $0.45 < \Lambda_s \xi < 0.67$ as indicated above.

5.4 Conclusions

The method of obtaining the line feed correction factor Λ from complex potential theory is given. It is shown that if only the first term of the series expansion is used as suggested by Lund (Ref. 4.4), the result is only valid for particular ranges of bearing parameters.

The data presented considers a wide range of Λ values (viz. 0.2→1). This is more generally applicable than the analysis given by M.T.I. (Ref. 2.11) for which one specific value of Λ ($\Lambda = 0.67$) was considered.

It has been shown that the value of $1/\lambda$ significantly affects bearing performance. Flow rate, bearing load capacity, and stiffness have all been shown to be largely dependent upon the parameter $1/\lambda$.

6. THE APPLICATION OF FINITE DIFFERENCE METHODS

6.1 Introduction

Finite difference methods can be used to solve film pressures for either steady state or dynamic simulations of bearing behaviour. A review of various methods has been made by Castelli and Pirvics (Ref. 6.1).

An intermediate relaxation finite difference solution relating to zero speed conditions for journal bearings which employ slot restrictors has been developed by Rowe and Stout (Ref. 6.2). Other methods include the Alternating - Direction - Implicit (A.D.I.) scheme developed by Peaceman and Rachford (Ref. 6.3) which have been used for both steady state and dynamic analyses of journal bearings (Refs. 2.12 and 6.4) and for thrust bearings (Ref. 6.5).

The method developed by Rowe and Stout has been extended in this study to take account of the discrete nature of the orifices and the effect of aerodynamic contributions. A comparison of this method with results from the A.D.I. technique is given in Section 9.7 relating to journal bearings. The method presented in this thesis can be used to calculate film pressures for aerodynamic, aerostatic or hybrid operation. Also, the technique can be applied to any type of bearing geometry which employs orifice restrictors, e.g. journal bearings, collar thrust bearings and rectangular thrust bearings.

The equations used in the finite difference analysis to describe the flow through the bearing film in this work are based on the following assumptions:

(a) The flow throughout the entire bearing film is assumed to be purely viscous, ignoring slip at the boundaries. This means that gas inertia is neglected, a valid assumption for low Reynolds' Numbers.

(b) The gas flows through the bearing film at constant temperature (i.e. isothermal conditions). This implies that the heat generated by the

viscous shearing is efficiently dissipated - a valid assumption for small clearances and where bearing materials having high values of specific heat are employed. As typical bearings used in practice employ both small clearances and metal for the bearing faces, this assumption would be valid.

(c) Pressure is constant across the bearing film. For the small clearances used in practice, the pressure would vary only marginally across the film.

6.2 Downstream Grid Points

Figure 6.1 shows an elemental area within the bearing film downstream of the restrictor. The flow to the grid point can be expressed as a combination of pressure induced and velocity induced flows across the boundaries from the surrounding grid points. This implies one-dimensional flows with pressure constant normal to the flow directions. This is a valid assumption if the elemental area is small compared to the pressure gradient across it.

The pressure induced flow is given by:-

$$\dot{m} = \frac{L^3}{12\eta RT} \cdot \rho\Delta P \cdot \frac{\text{flow width}}{\text{flow length}}$$

The derivation of the above equation is given in Section 3.2

Substituting:

$$\rho\Delta P = \frac{\Delta(P^2)}{2}$$

gives : $$\dot{m} = \frac{L^3}{24\eta RT}\,\Delta(P^2)\,\frac{\text{flow width}}{\text{flow length}} \quad \ldots\ldots (6.1)$$

The velocity induced flow is given by:-

$$\dot{m} = A \rho V$$

$$= \Delta x \; h \; \frac{P_{mean}}{RT} \; \frac{u}{2} \quad \ldots\ldots (6.2)$$

The net flow to any point must be zero for mass flow rate continuity.

With reference to Figure 6.1 , summing flows to the point (i,j) and equating to zero gives:-

$$\dot{m}\left[(i,j+1) \rightarrow (i,j)\right] + \dot{m}\left[(i,j-1) \rightarrow (i,j)\right]$$

$$+ \dot{m}\left[(i+1,j) \rightarrow (i,j)\right] + \dot{m}\left[(i-1,j) \rightarrow (i,j)\right] = 0$$

The mass flow rates given by Equations (6.1) and (6.2) can be expressed with reference to the grid dimensions as:-

(a) Pressure induced flow

$$\dot{m}\left[(i,j+1) \rightarrow (i,j)\right]_{PI}$$

$$= \frac{h^3(i)}{24 \eta RT} \left\{ P^2(i,j+1) - P^2(i,j) \right\} \frac{1}{GA}$$

$$\dot{m}\left[(i,j-1) \rightarrow (i,j)\right]_{PI}$$

$$= \frac{h^3(i)}{24 \eta RT} \left\{ P^2(i,j-1) - P^2(i,j) \right\} \frac{1}{GA}$$

$$\dot{m}\left[(i+1,j)\rightarrow(i,j)\right]_{PI} = \frac{GA}{24\eta RT}\left\{p^2(i+1,j)-p^2(i,j)\right\}\left\{\frac{h^3(i+1)+h^3(i)}{2}\right\}$$

$$\dot{m}\left[(i-1,j)\rightarrow(i,j)\right]_{PI} = \frac{GA}{24\eta RT}\left\{p^2(i-1,j)-p^2(i,j)\right\}\left\{\frac{h^3(i-1)+h^3(i)}{2}\right\}$$

(b) Velocity induced flow

$$\dot{m}\left[(i+1,j)\rightarrow(i,j)\right]_{VI} = \Delta x\left\{\frac{h(i+1)+h(i)}{2}\right\}\left\{\frac{p(i+1,j)+p(i,j)}{2}\right\}\frac{u}{2RT}$$

$$\dot{m}\left[(i-1,j)\rightarrow(i,j)\right]_{VI} = -\Delta x\left\{\frac{h(i-1)+h(i)}{2}\right\}\left\{\frac{p(i-1,j)+p(i,j)}{2}\right\}\frac{u}{2RT}$$

The solution of any given bearing geometry involves summation of the pressure induced flows in addition to velocity induced flows, where applicable. This analysis is only valid for the network shown in Figure 6.1. Typical examples for which this is applicable are:-

(a) aerodynamic journal bearings

(b) slot entry bearings where the discreteness of feeding is

neglected and the slots are assumed to provide a continuous line feeding.

(c) orifice restrictor bearings for the film clearance downstream from the restrictor.

6.3 Grid Points Surrounding Restrictor

The analysis presented in the previous Section is inadequate to account for the feeding region in the immediate vicinity of orifice restrictors as shown in Figure 6.2 . Special attention has to be paid to the modelling of this area in order to account for the discreteness of feeding.

The modelling technique used presumes that radial flow dominates to the surrounding grid points,and that downstream from these points the flow is represented as two dimensional flow as given in Section 6.2 .

The total pressure induced flow from the restrictor to the surrounding grid points is given by the eight radial flow elements thus:

$$\dot{m}\rho_I = \dot{m}[(i,j)\Rightarrow(i,j\pm1)] + \dot{m}[(i,j)\rightarrow(i\pm1,j)]$$
$$+ \dot{m}[(i,j)\rightarrow(i\pm1,j-1)]$$
$$+ \dot{m}[(i,j)\rightarrow(i\pm1,j+1)]$$

With reference to Section 3.2 , each radial flow element is defined by $\dot{m}$ where:-

$$pd^2 - p^2 = \frac{12\eta RT\,\dot{m}}{\pi h^3}\int_{d/2}^{R}\frac{2\pi}{\theta r}\,dr$$

where p = downstream grid pressure

r = radius

R = grid point radius (w.r.t. to centre of source)

Θ = angle subtended by radial flow element

d = source diameter

The integral

$$\int_{d/2}^{R} \frac{2\pi}{\Theta r}\, dr = \frac{2\pi}{\Theta} \log_e \left[\frac{R}{d/2}\right]$$

Therefore the mass flow element is given by:-

$$\dot{m} = \frac{L^3}{24\eta RT} \left\{P_d^2 - P^2\right\} \frac{\Theta}{\log_e \left[\frac{R}{d/2}\right]}$$

In the case of a rectangular grid network shown in Figure 6.2 :

Axial Direction

$$\Theta = 2 \tan^{-1}\left[\frac{1}{2GA}\right]$$

$$R = \Delta x$$

$$\therefore \quad \dot{m}\left[(i,j) \rightarrow (i, j \pm 1)\right]$$

$$= \frac{L^3}{24\eta RT} \left\{P_d^2 - P^2(i, j\pm1)\right\} 2\, GARJ$$

where $GARJ = \dfrac{\tan^{-1}\left[\frac{1}{2GA}\right]}{\log_e\left[\frac{2\Delta X}{d}\right]}$

Circumferential Direction

$$\theta = 2 \tan^{-1}\left[\frac{GA}{2}\right]$$

$$R = \Delta Y$$

$$\therefore \quad \dot{m}\left[(i,j) \rightarrow (i\pm1, j)\right] = \frac{L^3}{2\pi\eta RT}\left\{P_d^2 - P^2(i\pm1, j)\right\} 2\,GARI$$

where $$GARI = \frac{\tan^{-1}\left[\frac{GA}{2}\right]}{\log_e\left[\frac{2\Delta Y}{d}\right]}$$

Diagonal Direction

$$\theta = \frac{\pi}{2} - \tan^{-1}\left(\frac{1}{2GA}\right) - \tan^{-1}\left(\frac{GA}{2}\right)$$

$$R = \Delta y \sqrt{1 + (GA)^2}$$

$$\dot{m}\left[(i,j) \rightarrow (i\pm1, j\pm1)\right] = \frac{L^3}{2\pi\eta RT}\left\{P_d^2 - P^2(i\pm1, j\pm1)\right\} GARJI$$

where $$GARJI = \frac{\pi - 2\tan^{-1}\left(\frac{1}{2}GA\right) - 2\tan^{-1}\left(\frac{2}{GA}\right)}{\log_e\left[\frac{2\Delta y}{d}\sqrt{1+(GA)^2}\right]}$$

6.4 Evaluating Pressure Profiles

6.4.1 Orifice Bearings

The computation technique used throughout this work is demonstrated for bearings with pocketed orifices in Figure 6.3 . In the case of inherently compensated bearings, the technique used was exactly the same.

The procedure initially involves assigning restrictor downstream pressures. This can be accomplished by the use of empirical data from pressure profiles or from the analysis of a corrected line feed model given in Section 5 . The next step is to assign values to the film pressures to start the iteration process. These are determined from the boundary conditions of the restrictor downstream pressures, as previously discussed, and the atmospheric boundary. These initial values are initially calculated either by assuming a constant pressure gradient throughout or by calculating each grid pressure from complex potential theory.

6.4.2 Solving Grid Pressures

The solution of a grid pressure is achieved by summing the flows to the grid points and equating to zero. The equations are transposed to give the pressure at the respective grid point, as a function of surrounding grid pressures, grid dimensions and bearing surface speed if applicable.

The order of relaxation is from high pressure regions to the atmospheric boundaries, using the intermediate difference approach. After each point has been relaxed to an accurate pressure value relative to the surroundings, all the film pressures are tested in order to determine whether numerical convergence has been achieved. This process is repeated until the calculated film pressures converge to within 1×10^{-4} P_a. When this occurs, the film pressures that have been evaluated are those which give mass flow rate equality throughout the bearing film for the given boundary conditions.

6.4.3 Newton-Raphson Iteration at Restrictors

For each restrictor, the total mass flow rates from the source to the surrounding grid points are calculated, as well as the mass flow rates through each restrictor. For all restrictors, these two mass flow rates are compared. From a Newton-Raphson iteration technique, new downstream orifice pressures are deduced which gives mass flow rate equality, thus:-

Mass flow rate through restrictor = FLI

Mass flow rate from source diameter = FLO = GFJ + GFI + GFJI

where GFJ = mass flow rate from pocket in axial directions

GFI = mass flow rate from pocket in circumferential directions

GFJI = mass flow rate from pocket in diagonal directions

Newton-Raphson iteration for mass flow rate continuity gives:-

$$\left(\frac{p_d}{p_o}\right)_{new} = \frac{p_d}{p_o} - \frac{FLO - FLI}{\frac{d(GFJ)}{d\left(\frac{p_d}{p_o}\right)} + \frac{d(GFI)}{d\left(\frac{p_d}{p_o}\right)} + \frac{d(GFJI)}{d\left(\frac{p_d}{p_o}\right)} - \frac{d(FLI)}{d\left(\frac{p_d}{p_o}\right)}}$$

The new orifice downstream pressures are compared to the old values. If the difference between these values is greater than $1 \times 10^{-4} P_o$, then the boundary conditions are changed to the modified values, and the grid pressures again relaxed.

These iterations are repeated until mass flow rates and pressures equalise throughout the entire bearing.

6.5 Conclusions

The use of the finite difference technique provides a versatile method for the solution of bearing film pressures. As a result of this, much relevant design information can be obtained relating to specific conditions that prevail such as non-parallel film clearances in journal bearings which arises at eccentric conditions,particular design configurations such as non symmetric feeding arrangements and errors in manufacture. Much of the specific information that can be obtained from the finite difference method cannot be obtained from most other methods which are available.

PART C

STATIC PERFORMANCE OF JOURNAL BEARINGS

PART C - STATIC PERFORMANCE OF JOURNAL BEARINGS

7. INTRODUCTION

Aerostatic journal bearings can support rotating radial loads with extremely low friction within the bearings due to the low viscosity of the lubricant. This feature enables very high speeds to be obtained without incurring excessive viscous frictional losses and also provides low static frictional torque at zero speed. Applications which take advantage of this property include high speed spindle assemblies such as dental drills where speeds up to 500,000 r.p.m. have been achieved.

Another feature of this type of bearing is that the averaging action of the surface finish and the geometric deviations enables high orders of rotational accuracy to be achieved. For this reason, aerostatic journal bearings are widely used in roundness measuring machines and precision machine tool spindles.

Figure 7.1 illustrates typical journal bearing designs. Gas is admitted into the bearing clearance through small diameter orifices. These can take the form of either pocketed or inherently compensated orifices as shown. The pocket orifice design illustrated employs a pierced insert, press-fitted into a reamed hole to an appropriate depth below the surface of the bearing bore, and illustrates a typical design used in practice - although many other mounting arrangements can be employed. The inherently compensated or annular orifice is provided by simply drilling the walls of the bearing using an appropriate sized drill.

7.1 Literature Review

The most simple and earliest analytical approach was the one-dimensional model in which the bearing was divided into discrete axial strips and the flow along these strips was assumed to be in the axial direction only. Typical design methods which have adopted this approach include Shires (Ref. 7.1), Tang and Gross (Ref. 3.1) and Holster (Ref. 3.2).

Experimental work conducted in 1958 by Robinson and Sterry (Ref. 7.2) established that an optimum bearing condition could be obtained at which the load capacity was maximised. This optimum condition was achieved by the matching of the various bearing parameters, such as bearing clearance, orifice diameter and number of orifices per row. In order to correct the axial flow model due to circumferential pressure losses, empirical factors were obtained.

Shires (Ref. 7.3) extended this work in 1962 and obtained a modified expression for circumferential flow which increased the accuracy of the predictions.

This early pioneering work, in conjunction with unpublished work conducted at Southampton University in the early 1960's, provided the foundation for the first comprehensive design guide by Shires published in Grassam and Powell's book (Ref. 7.4) in 1964. This design method gave data principally for a high eccentricity ratio of $\varepsilon = 0.9$, although information was provided to correct the design predictions to lower operating eccentricities of $\varepsilon = 0.1$ and $\varepsilon = 0.5$. The effect on load capacity due to changing the number of orifices was presented as a series of correction factors. The larger the number of orifices, the greater the load capacity.

The design information presented by Shires was updated by Powell(Ref. 7.5)

in 1971 who gave design information specifically for the more modest eccentricity ratio of $\varepsilon = 0.5$. At this time the importance of dispersion losses was more fully appreciated.

Greater understanding was provided by Dudgeon and Lowe (Ref. 7.6) who in 1965 reported work undertaken on the effect of the gas flow divergence around feed holes. This effect was aptly named 'dispersion'. Employing the electrical analogue method, expressions (derived empirically) were presented to correct the axial flow model. Although this work had great potential, no further information in the form of design data has been published (Private Correspondence 1974).

In contrast to the design methods formulated in Britain by Shires and Powell, which were based mainly upon experimental studies, other design methods were developed elsewhere from a mainly theoretical standpoint. These further design methods were developed at a somewhat later date which can be attributed to the evolution of more modern analytical treatments and to the availability of high speed computers.

In America, M.T.I. (Ref. 2.11) published a design method in 1967. The theoretical model used was a line feed model corrected to account for dispersion losses as discussed in Section 5. The analytical method was the small eccentricity-perturbation technique originally developed by Ausman (Ref. 7.7) in 1959 for self acting bearings and further extended for externally pressurised bearings by Lund (Ref. 7.8). This design guide is the most comprehensive currently available and gives additional information which was absent in the data presented by Shires and Powell - namely guidance to avoid pneumatic hammer instability and specific guidance on the selection of the line feed parameters.

Constantinescu in Rumania also produced a design method in 1967 (Ref. 7.9) which like M.T.I., gave predictions using purely mathematical techniques. However, unlike the model used by M.T.I., no account is made for the discrete nature of the feeding region. The results presented are therefore applicable to bearings with a sufficiently large number of inlets to approach a line source feeding. The linearisation procedure used also limits the results to low eccentricities.

A comparison of these design methods has been presented by the Author in 1974 (Refs. 7.10 , 7.11), as well as references to other theoretical methods. To conclude this work, the accuracy of the design methods has been deduced by the Author in 1976 (Refs. 2.1 , 2.2). This has been achieved by comparison of the results from an experimental study with that of the design method predictions. It was shown that discrepancies and experimental trends existed which undermines the validity of the design information presented at this time. In particular, the existance of lock-up was experimentally observed for which limited reference was made in the design methods. A design method based upon these experimental studies has been presented by Pink and Stout (Ref. 7.12) in 1978.

In view of the need for an accurate theoretical analysis of these bearings a theoretical study has been presented by Pink and Stout (Ref. 7.13) in 1980 which employs finite difference techniques. It was shown that by using a suitable restrictor loss analysis in conjunction with an appropriate finite difference grid network to account for the discreteness of feeding, good correlation was achieved between theory and experiment up to and including the effects of lock-up.

Work conducted at Liverpool Polytechnic by Markho et.al.(Ref. 2.19) in

1979 has quantified the effects of misalignment and directionality on the performance characteristics of a double plane admission bearing having a length to diameter ratio of unity. The results from a study on the effects of inter-orifice variations has also been published in 1980 by Stowell et.al. (Ref. 7.14).

Finite difference techniques have also been developed using the Alternating-Direction-Implicit (A.D.I.) scheme originally proposed by Peaceman and Rachford (Ref. 6.3). The application of this method to journal bearings was made by Elrod and Glanfield (Ref. 2.12) in 1970 and further improvements on this theoretical method has been reported by Auburn (Ref. 7.15). Other applications of the A.D.I. method to journal bearing analysis include a theoretical analysis developed by Kazimierski (Ref. 6.4).

7.2 Aims and Scope of the Investigation

The bearings considered for this investigation are those with either pocketed or inherently compensated orifices.

The aims of this study are :

1. To present various theoretical models, to discuss their limitations and to indicate the effect of changing various design parameters on the bearing performance.

2. To compare the various theoretical models with experiment in order to deduce their accuracy and validity.

3. To examine theoretically and to quantify the effect of various manufacturing errors on the bearing performance. In order to verify this work, experimental results, for which the limits of manufacturing tolerances are known, are compared with appropriate theoretical values.

The experimental data which has been used for comparison with the theoretical predictions has been obtained by the Author (Ref. 2.2), Markho et. al. (Ref. 2.19) and Grewal (Ref. 7.16).

8. ANALYSES

8.1 Calculation of Radial Load Capacity and Angular Torque

A number of non-dimensional parameters concerning the radial loading and angular torque will be used in later sections dealing with bearing performance. To eliminate repetition, the computation procedure for calculating these parameters is presented below. The procedures are common for all the theoretical models outlined.

The geometry of a bearing subjected to a radial load W and an angular torque T_q is shown in Figures 8.1 and 8.2 .

The local clearance is defined as :

$$h = h_o \left\{ 1 + \left[\varepsilon_c - \varepsilon_T \frac{(JSPAN + 1 - j)}{JSPAN} \right] \cos\left[\frac{2\pi(i-1)}{IDIV} \right] \right\}$$

Load Capacity

$$W = \sum \oint \delta A \cos\Theta$$

Using the grid notation shown in Figure 8.2 :

$$W = \frac{2\pi L D p_a}{(JSPAN)(IDIV)} \sum_{j=JSPAN}^{j=1} \sum_{i=IDIV}^{i=1} \left[\frac{\bar{p}(i,j) + \bar{p}(i,j+1)}{2} \right] \cos\left\{ \frac{2\pi(i-1)}{IDIV} \right\}$$

Non-dimensionalising to the form:

$$\overline{W} = \frac{W}{L D (P_0 - P_a)}$$

gives:

$$\overline{W} = \frac{2\pi}{(P_0/P_a - 1)(JSPAN)(IDIV)} \sum_{JSPAN}^{j=1} \sum_{IDIV}^{i=1} \left[\frac{\bar{p}(i,j) + \bar{p}(i,j+1)}{2} \right] \cos\left\{ \frac{2\pi(i-1)}{IDIV} \right\}$$

Radial Stiffness

The radial stiffness is given by:

$$K = \frac{dW}{de} = \frac{dW}{L_0 \, d\varepsilon}$$

$$\therefore \quad \frac{dW}{d\varepsilon} = K L_0$$

The stiffness is non-dimensionalised to the form :

$$\overline{K} = \frac{d\overline{W}}{d\varepsilon} = \frac{K L_0}{L D (P_0 - P_a)}$$

Angular Torque

Restoring torque is calculated by numerical integration thus :

$$T_Q = \sum \rho \, \delta A \cos\Theta \, x$$

$$= \sum \Delta W x$$

$$= \sum_{JSPAN}^{j=1} \sum_{IDIV}^{i=1} \Delta W \frac{(JSPAN - j + 0.5)}{JSPAN} \frac{L}{2}$$

Non-dimensionalising to the form :

$$\overline{T_Q} = \frac{T_Q}{L D^2 (\rho_o - \rho_a)}$$

gives :

$$\overline{T_Q} = \frac{L}{D} \frac{1}{2\,JSPAN} \sum_{JSPAN}^{j=1} \sum_{IDIV}^{i=1} \Delta \overline{W} (JSPAN - j + 0.5)$$

Angular Stiffness

The angular stiffness is given by:

$$K_A = \frac{d T_Q}{d\alpha} \quad \text{torque/radian} \quad , \quad \text{where} \quad d\alpha = \frac{de_1}{L/2}$$

Non-dimensionalising :

$$\overline{K_A} = \frac{\alpha \overline{T_q}}{2 \alpha \varepsilon_T} = \frac{K_A h_o}{L^2 D^2 (P_o - P_a)}$$

8.2 Line Feed Solutions

Various simplified bearing analyses are presented for which the row of orifices are, for convenience, replaced by a line feed. The different models represent varying degrees of refinement. The mass flow rate through the orifices are represented by the simplified analysis given by Equations (2.8) and (2.13) . These equations assume that C_d is constant, and that effects such as pressure recovery, inertia effects and supersonic flow domains within the bearing film are neglected.

8.2.1 One Dimensional Model

The one-dimensional model provides an idealised case for which circumferential flow and dispersion losses between inlets are ignored. The results from this model provide information on the ultimate performance of an idealised bearing in terms of load capacity and stiffness.

The general analysis for one-dimensional flow has been described in Section 3 , for which the results relating to downstream pressure ratio P_d/P_o and non-dimensional mass flow rate $\overline{G}$ has been presented in Figures 3.3 and 3.4 respectively.

The shape factor ξ , as given in Section 3.2 , is defined as:

$$\xi = \int_0^{y=Y} \frac{2\pi}{x} \, dy$$

In this case, dy = dx and x = π D. For single admission bearings Y = L/2 and for two plane admission bearings Y = a.

Thus:

$$\xi = \int_0^{L/2} \frac{2}{D}\, dx = \frac{L}{D} \quad \text{for single plane admission}$$

$$\xi = \int_0^{a} \frac{2}{D}\, dx = \frac{2a}{D} \quad \text{for double plane admission}$$

The film pressure at a distance x from the inlet plane is given by:

$$\bar{P} = \frac{P}{P_a} = \left\{ \left(\frac{P_d}{P_a}\right)^2 - \left[\left(\frac{P_d}{P_a}\right)^2 - 1 \right] \frac{x}{a} \right\}^{1/2}$$

This analysis is applicable to bearings with short L/D ratios where circumferential flow is absent and also a large number of inlets around the feeding plane.such that zero dispersion occurs.

8.2.2 Line Feed Model

The influence of circumferential flow is dependent upon L/D, eccentricity ratio and bearing tilt.

In order to account for two dimensional flow, a finite difference method applicable for the case of the line feed model has been used to calculate bearing film pressures and hence performance characteristics.

With reference to Section 6 , the shape factors applicable to the finite difference grids shown in Figure 8.2 are as follows:

$$GA = \frac{\text{grid spacing in axial direction}}{\text{grid spacing in circumferential direction}}$$

$$= \frac{L}{2\ JSPAN} \cdot \frac{IDIV}{\pi D}$$

The analysis was used in a computer program to calculate film pressures and bearing performance. The inlet pressures P_d/P_o were initially set assuming only axial flow and grid pressures relaxed until convergence was achieved. The flows through the restrictors were compared to those obtained from the assumed line source to the downstream grid positions in the axial directions. The inlet pressures were adjusted by Newton-Raphson iteration techniques to achieve mass flow rate equality and the grid pressures again relaxed. This process was repeated until equality of mass flow rates and convergence in film pressures was achieved.

8.2.3 Corrected Line Feed Model

To account for dispersion losses, the analysis presented in Section 5 is reviewed with reference to journal bearings.

The line feed correction factor $1/2$ is given by Figure 5.2, where:

n = number of inlets/row

N = total number of inlets in bearing

ξ = L/D for single admission bearings

= 2a/D for double admission bearings

d/D = d_f/D for inherently compensated bearings

= d_R/D for pocketed compensated bearings

D = bearing diameter

For the case of concentric conditions $\xi_c = 0$ and $\xi_T = 0$, the pressure profile has the form:

$$\bar{p} = \frac{p}{p_a} = \left\{ \left(\frac{p_2}{p_a}\right)^2 - \left[\left(\frac{p_2}{p_a}\right)^2 - 1 \right] \frac{x}{a} \right\}^{1/2}$$

The analysis method used for calculation was the finite difference solution which has been previously described in Section 6.

The downstream pressure ratio P_d/P_o and non-dimensional flow rate has been discussed in Section 5, with reference to Figures 5.4 and 5.5.

8.3 Finite Difference Solution

Using finite difference methods previously described in Section 6, an analysis is presented for journal bearings. The analysis takes into account dispersion losses between the inlet restrictors and clearance variations.

For pocketed orifices, the restrictor loss analysis employed is that defined by Equation (2.17). This is the more representative model than

that used in the line feed solutions as recovery within the film is accounted for. Also, the value of C_d used is dependent upon P_p/P_o, defined by Equation (2.11) .

For inherently compensated orifices, the restrictor loss analysis as given by Equation (2.8) is used which neglects pressure recovery, inertia effects and supersonic flow domains within the bearing clearance.

The grid network used in the computation is shown in Figure 8.3 . With reference to Section 6 , the shape factors of the finite difference grid are given below:

$$GA = \frac{L}{D} \frac{IDIV}{2\pi\, JSPAN}$$

$$GARJ = \frac{\tan^{-1}\left[\frac{1}{2\,GA}\right]}{\log_e\left[\frac{L}{JSPAN\;d}\right]}$$

$$GARI = \frac{\tan^{-1}\left[\frac{2}{GA}\right]}{\log_e\left[\frac{2\pi D}{IDIV\;d}\right]}$$

$$GARJI = \frac{\pi - 2\tan^{-1}\left(\frac{1}{2}GA\right) - 2\tan^{-1}\left(\frac{2}{GA}\right)}{\log_e\left[\frac{2\pi D}{IDIV\;d}\sqrt{1+GA^2}\right]}$$

The initial values assigned to the restrictor downstream pressure were calculated from the corrected line feed analysis and the film pressures were calculated using the complex potential theory. It was found that the final calculated bearing performance was insensitive to the initial film pressures. However, by selecting more representative film pressures as initial values in the iteration process, the number of iterations necessary to achieve satisfactory convergence was reduced and, as a consequence computer process time reduced.

9. DISCUSSION OF THEORETICAL RESULTS

9.1 Introduction

In this section, results from the various theoretical models are presented. The corrected line feed model is used to evaluate the effect of the various design parameters on the bearing performance. This enables an indication of the significance of these design parameters to be determined.

A comparison is also given between the results from the corrected line feed model with the finite difference solution and conclusions drawn as to their respective merits.

9.2 Effect of Circumferential Flow and Dispersion

The circumferential and dispersion losses are shown in Figure 9.1 for both single and double plane admission bearings. Non-dimensional load capacity, based on projected bearing area and supply pressure and hence a measure of the bearing efficiency, is plotted against L/D for a given eccentricity ratio. As L/D ratio approaches zero, no circumferential pressure losses occur and in the absence of dispersion losses, the bearing can be modelled from the one dimensional analysis. As expected, the effect of increasing L/D ratio is to increase the circumferential losses and to effectively reduce the bearing efficiency.

The effect of dispersion is accounted for by the line feed correction parameter $1/\lambda$. This design parameter, which is calculated from n,d/D and L/D gives a measure of the dispersion losses. The effect of $1/\lambda$ on load/deflection characteristics is shown in Figure 9.2 . It can be seen that the bearing performance is significantly dependent upon the $1/\lambda$ value. It is interesting to note that the percentage reduction in load

capacity for a given $1/\lambda$ value is almost independent of L/D ratio. This indicates the relevence of $1/\lambda$ as a design parameter as its value can be used to give a measure of the dispersion losses, in terms of a percentage loss, from the line feed model.

9.3 Lock-Up

Load capacity is plotted against ε for various L/D ratios in Figure 9.3 . These results are from the line feed model as dispersion losses are absent $(1/\lambda = 1)$. As L/D increases, the load parameter reduces as discussed previously. The effect of eccentricity is to give a greater percentage reduction from the one dimensional model (viz. $L/D \rightarrow 0$). This implies that greater circumferential losses occur as eccentricity is increased. An important characteristic occurs as a result of this. The one dimensional model ($L/D \rightarrow 0$) gives a continuously increasing load as ε increases. As $\varepsilon \rightarrow 1$, the stiffness, although still positive, is relatively small. If the loss in load capacity due to circumferential flow increases with increasing ε at a higher rate than the increase in load capacity as demonstrated for the one dimensional model ($L/D \rightarrow 0$), then bearing load will reduce as $\varepsilon \rightarrow 1$. This phenomenon is known as lock-up and manifests itself at high eccentricities by a sudden collapse when load is increased and is due to a negative stiffness region. It can be seen from Figure 9.3 as L/D increases, bearings are more prone to lock-up.

These characteristics are further explained with reference to film pressures in Figure 9.4 . A two plane admission bearing is considered and the film pressures in-line with the load and half way between the admission planes are shown in Figure 9.4(a). In the low clearance side of the bearing the one-dimensional model gives a continuously increasing film pressure as ε increases. The effect of circumferential flow is to reduce the film

pressure P_H. At this point within the film the circumferential flow path

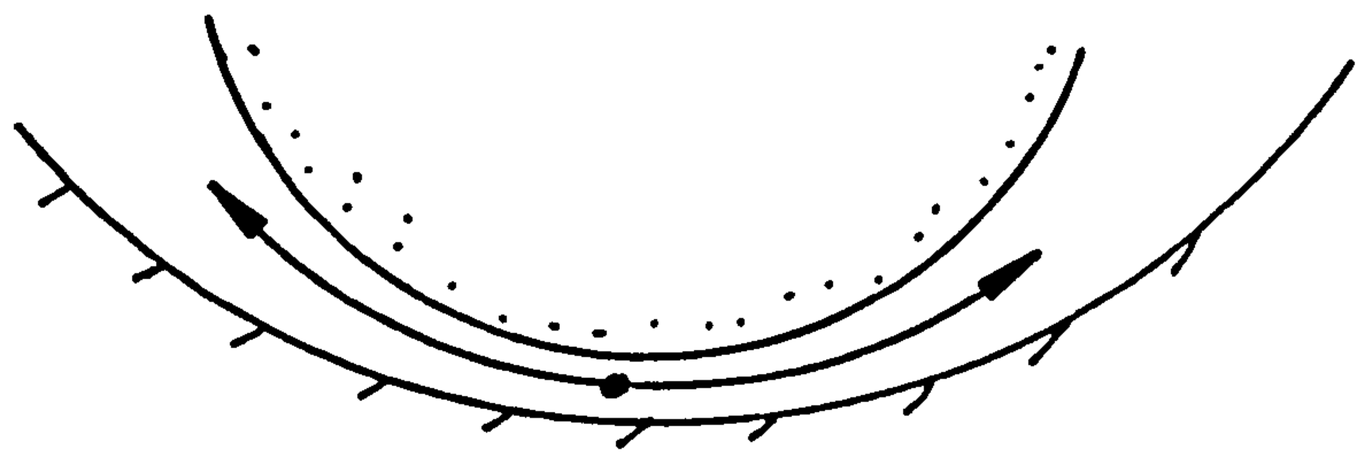

has a converging shape as shown above whilst in the axial direction parallel film conditions exist. As ε increases, the gas film is losing pressure due to circumferential flow at a faster rate, even though the orifice pressure is increasing. This effect becomes more pronounced the further downstream from the orifice and/or as L/D increases.

The pressure differential across the bearing is plotted against ε in Figure 9.4(b). It can be seen that the pressure difference reaches a maximum and subsequently reduces. The eccentricity of this maximum need not coincide with the eccentricity at which lock-up occurs. Lock-up is dependent upon the integrated film pressures whilst Figure 9.4 shows only one sample pressure plane to demonstrate the effect. An important aspect of this work is that it has been shown that lock-up is predicted from a simple line feed model. As dispersion has been neglected, the existence of lock-up is predicted from exclusively circumferential flow considerations. This has also been predicted for the case of slot entry journal bearings by Rowe and Stout (Ref. 6.2) where a similar line feed model has been assumed with the absence of dispersion losses. The influence of dispersion losses around orifices can be expected to reduce the pressure differential and hence the bearing would be even more prone to lock-up.

9.4 Effect of Various Design Parameters on $\overline{W}$

9.4.1 Feeding Parameter $\Lambda_s \xi$

Load capacity against $\Lambda_s \xi$ for various ε and P_o/P_a are shown in Figure 9.5. The characteristic shapes of the curves are common to all journal bearings independent of L/D, a/L, ξ_o and $1/\lambda$. For different values of these parameters, the absolute level of $\overline{W}$ changes but the shapes would remain the same. Therefore conclusions regarding Figure 9.5 are common to all journal bearings and are not specifically applicable for the conditions shown.

At the low eccentricity condition $\varepsilon = 0.25$, the results can be used to deduce bearing stiffness with the assumption that stiffness is constant up to $\varepsilon = 0.25$. For this condition, the results follow closely those given in Section 3.6 dealing with sensitivity of dP_d/dh as shown in Figure 3.5 . It can be seen from Figure 9.5 that the optimum $\Lambda_s \xi$ to achieve maximum stiffness corresponds to those quoted in Section 3.6 .

At higher eccentricities, the optimum value of $\Lambda_s \xi$ to achieve maximum load capacity reduces. This bearing characteristic has also been found experimentally by the Author (Ref. 2.1).

The effect of $\Lambda_s \xi$ on loading eccentricity curves is shown in Figure 9.6 . At low values of $\Lambda_s \xi$ ($\Lambda_s \xi \leq 0.1$) the bearing exhibits increasing stiffness up to $\varepsilon \simeq 0.7$. At higher values of $\Lambda_s \xi$ ($0.5 \geq \Lambda_s \xi \geq 1.0$) the bearing exhibits reducing stiffness as ε increases. At still higher values ($\Lambda_s \xi$ = 10) the trend reverts back to an increasing stiffness with ε characteristic. These trends have been noted from experimental studies by the Author (Ref. 9.1).

9.4.2 Line Feed Correction Factor $1/\lambda$

Load capacity at $\varepsilon = 0.5$, is plotted against $\Lambda_s\xi$ for various $1/\lambda$ in Figure 9.7 . It can be seen that $1/\lambda$ significantly affects load capacity with increasing effect as $\Lambda_s\xi$ increases. As the value of $1/\lambda$ reduces the maximum $\overline{W}$ reduces as well as the corresponding optimum $\Lambda_s\xi$. This has been discussed in Section 5.3.3 where optimum values of $\Lambda_s\xi$ have been presented.

9.4.3 Supply Pressure Ratio P_o/P_a

The variation of $\overline{W}$ for various P_o/P_a values (at a given ε and $\Lambda_s\xi$), as shown in Figure 9.5 is relatively small for a wide range of $\Lambda_s\xi$ values. The maximum variation for $\overline{W}$ for $\Lambda_s\xi > 0.1$ is tabulated below:

	$\varepsilon = 0.25$	$\varepsilon = 0.5$	$\varepsilon = 0.8$
% $\overline{W}$ variation for $P_o/P_a = 2 \rightarrow 8$	15.8%	8.3%	5.6%

The effect of P_o/P_a on $\overline{W}/\varepsilon$ for $\Lambda_s\xi = 0.5$ is shown in Figure 9.8 . This value of $\Lambda_s\xi$ corresponds to approximately optimum conditions for maximum load capacity. It can be seen that for the range of P_o/P_a shown, the effect on $\overline{W}/\varepsilon$ is relatively small and is tabulated below:

	$\varepsilon = 0.25$	$\varepsilon = 0.5$	$\varepsilon = 0.8$
% $\overline{W}$ variation for $P_o/P_a = 2 \rightarrow 8$	6.2%	5.9%	3.2%

9.4.4 Land Width Ratio a/L

The effect of the number of feeding planes on load eccentricity characteristics is shown in Figure 9.9 . The ratios of load capacities are tabulated below:

	ε = 0.25	ε = 0.5	ε = 0.8
$\frac{\overline{W} \text{ for } a/L = 0.5}{\overline{W} \text{ for } a/L = 0.25}$	0.734	0.727	0.719

9.4.5 Type of Compensation

Figure 9.10 shows the effect of the type of orifice compensation on the $\overline{W}/\varepsilon$ characteristics. The ratios of $\overline{W}$ are tabulated below:

	ε = 0.25	ε = 0.5	ε = 0.8
$\frac{\overline{W} \text{ for inherently compensated}}{\overline{W} \text{ for pocketed}}$	0.690	0.742	0.801

As expected, the load ratio at low eccentricity approaches 0.667 which has been derived theoretically in Section 3.6.1 . At higher eccentricities, the load ratio increases. This is attributed to the fact that bearings with inherently compensated orifices have a lower pressure differential and as such exhibit lower circumferential losses in terms of their total load capacity. However it has to be borne in mind that inherently compensated orifice diameters d_f are usually smaller than pocket diameters

d_R. Therefore, for a given n, L/D and D the value of $1/\lambda$ applicable for inherently compensated bearings is usually lower than for the equivalent pocketed bearing. Therefore, the load capacity is proportionally lower for inherently compensated bearings due to their higher dispersion losses.

9.5 Mass Flow Rate Against Eccentricity Ratio

The effect of ε on mass flow rate is shown in Figure 9.11 for a range of $\Lambda_s \xi$ values and differing types of compensation. It can be seen that at low values of $\Lambda_s \xi$, ($\Lambda_s \xi = 0.1$) mass flow rate varies only slightly over the entire ε range. This is due to the fact that all the orifices are choked up to $\varepsilon \leqslant 0.59$ for pocketed orifices and for the entire range of ε for inherently compensated orifices.

At the higher values of $\Lambda_s \xi$ equal to 0.5 and 1.0, the orifices at concentric conditions are unchoked. At a particular eccentric condition choking occurs in the high clearance side. For this condition, the mass flow rate is fixed for pocketed orifices and further increases in ε do not affect the mass flow through the choked orifices (flow area = $\pi d_o/4$). However, for inherently compensated orifices further increases in ε result in increased choked flow rates accordingly (flow area = $\pi d_f h$).

With reference to Figure 9.11 the mass flow rate for inherently compensated orifices is almost constant up to $\varepsilon \leqslant 0.6$. At higher eccentricities, mass flow rate increases slightly. For pocketed bearings mass flow rate reduces as ε increases. The effect of increasing $\Lambda_s \xi$ on the $\bar{G}/\varepsilon$ characteristics is to accentuate these trends.

One implication of these trends is that it may be possible to determine whether a bearing is optimised correctly by examining flow rate/ ε characteristics and thus deducing $\Lambda_s \xi$.

9.6 Effect of Various Design Parameters on $\overline{T}_q$

9.6.1 Feeding Parameter $\Lambda_s\xi$

Non-dimensional torque is plotted against $\Lambda_s\xi$ for various $1/\lambda$ is shown in Figures 9.12(a) and 9.12(b) for single and double plane admission bearings respectively. These two types of bearings differ in the way $\Lambda_s\xi$ influences $\overline{T}_q$.

For single admission bearings, the tilting occurs about the feeding plane where the eccentricity ratio ε_c is specified as zero. The film pressure at this plane varies only slightly with ε_T and can be determined approximately from the value of $\Lambda_s\xi$ and $1/\lambda$ as discussed in Section 5.3 and shown in Figure 5.4 . $\overline{T}_q$ is dependent upon the line feed pressure P_L/P_o in the plane of the orifices and as a result, the curves of $\overline{T}_q$ against $\Lambda_s\xi$ for single plane bearings follow closely that for P_L/P_o curves shown in Figure 5.4 . The values of $\overline{T}_q$ shown in Figure 9.12(a) are independent of the type of compensation and apply for bearings with either pocketed or inherently compensated orifices.

In contrast to this is the double admission bearing characteristics. In this case , tilting affects the restrictor pressures at the feeding planes. Unlike single admission bearings, the value of $\overline{T}_q$ maximises at an optimum $\Lambda_s\xi$. This optimum value of $\Lambda_s\xi$ corresponds approximately to that for maximum load capacity at small radial eccentricity ratios shown by the curves for $\varepsilon = 0.25$ in Figure 9.5 . It can be seen from Figure 9.12 (b) that the value of $1/\lambda$ significantly affects $\overline{T}_q$. The effect of $1/\lambda$ on $\overline{T}_q$ is similar in form to the effect on W.

$\overline{T}_q$ is plotted against ε_T in Figure 9.13 for various $\Lambda_s\xi$ for double admission bearings. At low values of $\Lambda_s\xi$ ($\Lambda_s\xi \leq 0.1$), the angular

stiffness increases with ε_T ; for optimum conditions corresponding to maximum $\overline{T}_q$ shown by $\Lambda s \xi$ = 0.5 and 1.0, the angular stiffness is nearly constant up to ε_T = 1 whilst for higher values($\Lambda s \xi$ = 10) angular stiffness again increases slightly as ε_T increases.

9.6.2 Length to Diameter Ratio L/D

$\overline{T}_q$ is plotted against L/D for a/L = 0.25 and 0.5 in Figure 9.14 for $\Lambda s \xi$ = 0.5. For double admission bearings this value of $\Lambda s \xi$ corresponds approximately to the optimum value for maximum $\overline{T}_q$. However for single admission bearings it is pointed out that this value of $\Lambda s \xi$ is not the optimum value to maximise $\overline{T}_q$ - higher values of $\overline{T}_q$ can be obtained at higher $\Lambda s \xi$ values but with a corresponding loss of radial load capacity.

9.6.3 Supply Pressure Ratio P_o/P_a

The effect of P_o/P_a on $\overline{T}_q/\varepsilon_T$ characteristics are shown in Figure 9.15 . It can be seen that for the range of P_o/P_a considered, the effect on $\overline{T}_q/\varepsilon_T$ is relatively small. This was the case for the $\overline{W}/\varepsilon$ characteristic discussed in Section 9.4.3 . The % variations are tabulated below:

	ε_T = 0.25	ε_T = 0.5	ε_T = 1
% $\overline{T}_q$ variation for $P_o/P_a = 2 \rightarrow 8$	5.3%	4.2%	7.0%

9.6.4 Type of Compensation

Figure 9.16 shows the effect of the type of orifice compensation on the $\overline{T}_q/\varepsilon_T$ characteristics for double admission bearings. For single admission bearings, $\overline{T}_q$ is independent of the type of orifice compensation.

The ratios of $\overline{T}_q$ shown in Figure 9.16 are tabulated below:

	$\varepsilon_T = 0.25$	$\varepsilon_T = 0.5$	$\varepsilon_T = 1$
$\frac{\overline{T}_q \text{ for inherently compensated}}{\overline{T}_q \text{ for pocketed}}$	0.726	0.752	0.785

These results follow closely those previously presented in Section 9.4.5 dealing with the effect on $\overline{W}$.

9.7 Comparison of Results from Finite Difference Solution with A.D.I. Method

The results from the finite difference method used in this study has been compared with specimen results computed at Southampton University using the A.D.I. scheme described in Ref. 7.15 .

An inherently compensated journal bearing with the following parameters was investigated:

$$L/D = 1$$

$$a/L = 0.25$$

$$n = 8$$

$$P_o/P_a = 5.08$$

$$d_f = 0.66$$

$$h_o = 30\mu m$$

$$\delta_o = 5.5$$

$$d_f/D = 0.017$$

$$\lambda_s \xi = 0.359$$

A comparison of the theoretical results for radial stiffness and load capacity is summarised below:

	Finite Difference Method Used	A.D.I. Method	% Variation
K ($\varepsilon \to 0$) N/μm	9.29	9.49	2.1
W (ε = 0.5) N	143.0	148.9	4.1
W (ε = 0.8) N	179.7	185.5	3.2

Predicted film pressures at $\varepsilon = 0.5$ correlate to within 25 kN/m^2 (4 p.s.i) for a supply pressure of 414 kN/m^2 (60 p.s.i.).

It should be mentioned that the restrictor loss analyses used differ, in that the A.D.I. accounts for pressure recovery by the use of loss coefficients as discussed in Section 2.3.4 whilst the analysis used in this study employs a coefficient of discharge due to its simplicity. Despite these differences, and the fact that the two iterative techniques have been developed independently, the results correlate remarkable well.

9.8 Comparison of the Results from the Corrected Line Feed Model with the Finite Difference Solution

The corrected line feed solution provides a convenient method to obtain generalised design information and to determine the effect of changing various design parameters. However, although the effect of dispersion is included in the analysis, there is some doubt as to the validity of this model due to dispersion losses in the immediate vicinity of the discrete sources when the local clearance varies. The finite difference solution, on the other hand, treats the inlet flows as a number of discrete sources and thus

provides a more appropriate theoretical model. The question arises: how do the results of these two theoretical models compare?

To illustrate the differences and to present a comparison, a bearing with double plane admission, L/D = 1 has been analysed. Various combinations of numbers of orifices per row, n and pocket diameter to bearing diameter d_R/D have been investigated.

Figure 9.17 shows the load eccentricity curves for varying n with d_R/D fixed at 0.03. It can be seen that both the corrected line feed model and the finite difference solution give increasing load capacity as n is increased. This is to be expected as increasing n gives reduced dispersion losses. The corrected line feed model gives consistently higher load capacity than the finite difference solution, with reducing n and/or increasing ε leading to greater disparity. It can be seen that for $n \geqslant 6$ and $\varepsilon \leqslant 0.5$ good correlation exists between the two theoretical models - the maximum deviation being of the order of 7%.

Figure 9.18 shows the results from the two theoretical models for varying d_R/D with n = 8. In this case, the maximum deviation of 7% applies for $d_R/D \geqslant 0.01$ and $\varepsilon \leqslant 0.5$.

Figure 9.19 illustrates the combined effect of n and d_R/D on load capacity at $\varepsilon = 0.5$. The two theoretical models agree within 10% of each other for the following parameters:

$$\varepsilon \leqslant 0.5$$

$$n \geqslant 6$$

$$d_R/D \geqslant 0.01$$

Increasing n or d_R/D above these limits gives greater correlation between the two theoretical models.

9.9 Conclusions

It has been shown that by using complex potential theory, a corrected line feed model has been developed to account for dispersion losses. This model has been used to illustrate the effect of changing various design parameters and to obtain generalised design data. Both load capacity and angular torque results have been presented.

From this model, the phenomenon known as lock-up can be predicted. With reference to bearing film pressures, it has been shown that circumferential flow induces lock-up and confirms previously reported experimental observations. Other experimental trends which have been reported have been demonstrated theoretically. These include:

(1) The effect of $\Lambda_s \Sigma$ on load deflection characteristics

(2) The effect of ε on the optimum $\Lambda_s \Sigma$

The data presented considers a wide range of $1/\lambda$ values which is an advancement on the analysis given by M.T.I. — for which the design data is applicable for only one specific value of $1/\lambda$.

The effect of supply pressure ratio on non-dimensional load $\overline{W}$ and angular torque $\overline{T_q}$ has been found to be small. For the range of P_o/P_a between 2 and 8 the effect on $\overline{T_q}$ and $\overline{W}$ has been shown to be less than 6% for bearings designed at optimum conditions and operating at $\varepsilon \leq 0.5$. This implies that $\overline{T_q}$ and $\overline{W}$ are valid design parameters for typical operating conditions. This conclusion validates the design methods given by Powell (Ref. 7.5) and Pink and Stout (Ref. 7.12) where non-dimensional load parameters are

assumed to be independent of supply pressure ratio. When compared with the effect that the line feed parameter $1/\lambda$ has on bearing performance, this would seem a reasonable assumption.

A comparison between the results from the finite difference method used in this study with those employing the A.D.I. method of solution gives good correlation. However, only a limited comparison has been made and a more detailed study involving more comparisons are necessary in order to make generalised conclusions.

A comparison has been given between the results of the corrected line feed model with the finite difference solution. Various combinations of n and d_R/D have been analysed to illustrate the dispersion characteristics. It has been shown that the two theoretical models agree within 10% for $\mathcal{E} \leq 0.5$, $n \geqslant 6$ and $d_R/D \geqslant 0.01$. Outside these ranges the discrepancy increases. This is due to the local clearance variation in the immediate vicinity of the discrete sources. For these conditions, it is expected that the dispersion losses can be more accurately represented by the finite difference model.

10. COMPARISON BETWEEN THEORETICAL RESULTS AND EXPERIMENTAL DATA

10.1 Introduction

To determine the accuracy of the various theoretical models, the results are compared with experimental data. The experimental data used for the comparison have been previously obtained by the Author at Southampton University (Ref. 2.2) and at Leicester Polytechnic (Ref. 10.1) . Other experimental data for the comparison is that obtained at Liverpool Polytechnic by Grewal et. al.(Refs. 2.19, 7.16) .

10.2 Pressure Profiles

10.2.1 Concentric Conditions

Experimental and theoretical pressure profiles relating to concentric conditions are shown in Figure 10.1 . Each diagram relates to specific bearing conditions and pressure profiles are shown for both the axial and circumferential directions. The various bearings considered are tabulated below:

Fig. No.	L/D	a/L	n	d/D	P_o/P_a	Pocketed (PC) or Inherently Compens'd (IC)	Source Ref.
10.1(a)	0.5	0.5	16	0.031	3.04	PC	2.2
10.1(b)	———	———	"	———	5.08	↓	↓
10.1(c)	1.0	0.5	8	0.031	3.04	↓	↓
10.1(d)	———	———	"	———	5.08	↓	↓
10.1(e)	1.0	0.25	8	0.031	1.68	↓	↓
10.1(f)	———	———	"	———	3.04	↓	↓
10.1(g)	———	———	"	———	5.08	↓	↓
10.1(h)	———	———	"	———	7.80	↓	↓
10.1(i)	1.0	0.25	8	0.017	5.08	IC	↓
10.1(j)	1.0	0.25	8	0.050	3.67	PC	7.16

The parameters varied include L/D, a/L, n, d/D, P_o/Pa, types of compensation in addition to δ_o and $\Lambda_s \xi$. As many design parameters have been varied generalised conclusions can be made regarding the correlations between theory and experiment.

For Figures 10.1(a) - (i) , the experimental data relates to that obtained by the Author (Ref. 2.2) . The bearing film pressure was monitored by a pressure trarsducer located in test shafts behind a small diameter (0.06mm) pressure tapping. The test shaft was motorised to give a slow scanning speed either axially or circumferentially. Both axial and circumferential positions were monitored by plastic coated potentiometers and, together with the output of the pressure transducer, were connected to an X-Y plotter to give a complete pressure profile in either direction. The experimental data shown in Figures 10.1(a) - (i) are therefore of the form of continuous curves. The results from the two theoretical models are shown - the complex potential theory as presented in Section 4 , and the finite difference solution.

In the axial direction, two planes are considered - one under an orifice and the other midway between orifices. In Figures 10.1(a) - (i) , the experimental axial pressure profiles are shown for a number of circumferential positions. The pressure profile giving the highest pressure level corresponds to the plane in-line with an orifice; the lowest pressure level to a position midway between orifices. The experimental profiles have not been traced or modified and are presented in their original form to preserve their authenticity. Close to the orifice, predicted pressures are generally greater than those obtained experimentally. This can be attributed to inertia effects local to the restrictor, which are particularly evident for the inherently compensated bearing shown in Figure 10.1(i) .

The correlation between the results obtained from the complex potential theory and the finite difference theory is extremely good in both directions. As the complex potential theory is an exact solution, a conclusion is that the finite difference grid network around the discrete sources is a valid model to account for local pressure drops. The validity of various modelling techniques around sources has never been established and therefore the conclusions reached concerning this area are an important aspect of this work.

It is pointed out that the restrictor pressure P_d is calculated as part of the overall solution for each theoretical model. For both P_d and bearing film pressures, theoretical results compare well with experiment.

The experimental data shown in Figure 10.1(j) was obtained by Grewal (Ref. 7.16) . The radial clearance for this bearing was determined by two methods. The first from measurements of the bearing housing and test shaft. From this method, a radial clearance of 35.5 μm was deduced. However, the available movement between shaft and bearing was measured as 63.0 μm, indicating a radial clearance of 31.5 μm, 4 μm lower. In the case of the Author's experimental investigation reported in Ref. 2.2 , it was found that the indicated free movement of the test shaft within the bearing was largely dependent upon the cleanliness of the bore and shaft. Typical discrepancies between the two methods were typically in the range of 1-6 μm on diametrical clearance, a similar order was found by Grewal.

The experimental data obtained by Grewal is compared with theoretical results (from the finite difference solution) applicable for the two clearances deduced i.e. h_o = 31.5 μm and 35.5 μm.

From Figure 10.1(j) it can be seen that the clearance of h_o = 35.5 μm gives the better correlation.

10.2.2 Eccentric Conditions

Figure 10.2 compares theoretical and experimental pressure profiles for eccentric conditions.

Figure 10.2(a)- (e) show circumferential pressure profiles relating to experimental data obtained by the Author (Ref. 2.2) for L/D = 1 with double plane admission. Bearings with pocketed orifices are shown in Figures 10.2(a) - (d) for various supply pressures; inherently compensated orifices are shown in Figure 10.2(e). Two theoretical models are shown, the corrected line feed model and the finite difference solution. As illustrated in these figures, the corrected line feed model neglects the discrete nature of feeding although it includes allowance for dispersion. For this reason, this method is sometimes referred to as a 'smeared profile'. The theoretical results from the finite difference solution compare well with those obtained experimentally for pressure profiles, load capacity and mass flow rate. The results from the corrected line feed model tend to over-estimate load capacity and under-estimate flow rate. The discrepancy is within 15% and although this method can give large errors in the prediction of film pressures, the calculated load capacity and flow rate are within reasonable tolerances if this method is used to give approximate design information.

Figure 10.2(f) - (g) compares experimental data obtained by Grewal with theoretical results from the finite difference solution for the limits of the radial clearance. Figure 10.2(f) relates to the plane of the orifices; Figure 10.2(g) to the bearing centreline. As shown in Figure 10.1(j), for concentric conditions, an assumed clearance of h_o = 35.5 μm gives the better correlation between theoretical predictions and Grewal's experiments.

10.3 Load / Deflection

Figure 10.3 compares experimental load deflection characteristics (Ref. 2.2) with the theoretical results from two models - the finite difference solution and the corrected line feed model. Figure 10.3(a) refers to bearings with pocketed orifices; Figure 10.3(b) to inherently compensated. It can be seen that the corrected line feed model over-estimates load capacity - with increasing ε giving greater error. Up to $\varepsilon = 0.5$, the corrected line feed model gives load capacity to within 10% of that determined experimentally. The finite difference solution gives better correlation with experiment - typically within 4%.

Figure 10.4 plots load capacity for various ε against $\Lambda s \xi$. Both experimental and theoretical results (applicable to the finite difference solution) are shown. The results for pocketed orifices are shown in Figure 10.4(a) and for inherently compensated orifices in Figure 10.4(b). The experimental data is taken from Ref. 2.2 and numerical values together with the theoretical predictions and the percentage error is tabulated in Table 10.1 and Table 10.2 respectively. It can be seen that experimental and theoretical values correlate well for a wide range of supply pressures and $\Lambda s \xi$.

Within the range of $0.2 < \Lambda s \xi < 0.9$, the % variation between theory and experiment for $P_o/P_a \geq 3.04$ is given below:

	pocketed	inherently compensated
K ($\varepsilon \to 0$)	+ 7.3 % - 11.5 %	+ 7.4 % - 15.7 %
W ($\varepsilon = 0.5$)	+ 6.9 % - 7.3 %	+ 7.1 % - 3.6 %
W ($\varepsilon = 0.8$)	- 5.1 % - 1.4 %	+ 11.3 % + 1.1 %

Theoretical load deflection characteristics are compared with Grewal's experimental results in Figure 10.5 . Similar to the comparisons made for pressure profiles, it would appear that the theoretical model assuming $h_o = 35.5\,\mu m$ gives the better correlation with experiment.

10.4 Mass Flow Rate

The experimental mass flow rate at $\varepsilon = 0$ obtained in Ref. 2.2 is tabulated in Table 10.3 and 10.4 with the finite difference results and the percentage error. Table 10.3 refers to pocketed orifices; Table 10.4 to inherently compensated orifices.

Within the range of $0.2 < \lambda s < 0.9$, the % variation between theory and experiment for $P_o/P_a \geq 3.04$ is given below:

	pocketed	inherently compensated
G ($\varepsilon = 0$)	+ 10.0 % - 4.5 %	+ 6.0 % - 24.2 %

Experimental mass flow rate against eccentricity by Grewal are compared with the finite difference values in Figure 10.6 . The theoretical results for $h_o = 35.5\,\mu m$ give the better correlation with experiment.

10.5 Stiffness / Deflection

The variation of experimental stiffness/deflection data obtained by Grewal are compared with the finite difference predictions in Figure 10.7 . Again, the better correlation applies to the case for the theoretical values applicable to the higher clearance of $h_o = 35.5\,\mu m$.

10.6 Torque / Tilt Characteristics

Figure 10.8 compares experimental torque/tilt characteristics (Ref. 2.2) with theoretical results.

For the double admission bearing shown in Figure 10.8(a), the results from two theoretical models are shown - the finite difference solution and the corrected line feed model. It can be seen that the two theoretical models give good correlation with experiment, with the finite difference solution giving the more accurate predictions.

For single admission bearings shown in Figure 10.8(b), experimental torque stiffness is compared with the results from the corrected line feed model and the predictions from M.T.I. design charts. It can be seen that the M.T.I. predictions significantly over-estimate torque stiffness. This point has been previously noted by the Author in Ref. 7.12 . The results from the corrected line feed model are shown to give more accurate predictions.

Figure 10.9 compares theoretical torque/tilt characteristics with experimental results obtained for double admission bearings by Grewal. It can be seen that the theoretical results for h_o = 35.5 μm give better correlation with experiment.

10.7 Bearing Film Pressure

Figure 10.10 compares experimental film pressure/deflection characteristics for slot bearings obtained by the Author (Ref. 10.1) with the theoretical results from a line feed model (Ref. 6.2) . An important characteristic is that as eccentricity increases the film pressure in the low clearance side of the bearing P_H reaches a maximum value. A further increase in

eccentricity results in a reduction of film pressure - which is both theoretically predicted as well as experimentally observed. The pressure differential across the bearing is plotted against eccentricity in Figure 10.10(b). It can be seen that the pressure differential reaches a maximum and subsequent increases in eccentricity gives a reducing pressure differential which leads to lock-up. As slot bearings do not suffer significantly from dispersion losses, the reduction in film pressure that occurs in the low clearance side is due to exclusively circumferential pressure losses. The implication of this is that even if an orifice bearing were manufactured to give a line source feeding (for example with a circumferential groove connecting the orifices), the bearing would still exhibit lock-up if L/D was sufficiently large (e.g. $L/D \geqslant 0.5$).

Figure 10.11 compares experimental film pressure/deflection characteristics for orifice bearings (Ref. 2.1) with the theoretical results from two models - the finite difference solution and the corrected line feed model. The trends shown are similar to those discussed for slot bearings, except that the collapse of the film pressures occurs more severely, due to the influence of dispersion losses. The corrected line feed model gives an over-estimate of the pressure changes with eccentricity, whilst the finite difference solution gives a better representation.

Experimental results for film pressure differential against load capacity obtained by Grewal are compared with finite difference predictions in Figure 10.12 . The theoretical data shown indicates that clearance changes do not significantly influence the resultant film pressure differential/loading characteristic. The predicted fall of the film pressure differential at high loadings was not observed although this characteristic has been experimentally noted by the Author (Ref. 2.1) .

10.7 Conclusions

It has been shown that the finite difference solution gives accurate predictions for bearing film pressures including the area local to the sources. The results compare well with both experiment and the predictions from the complex potential theory. This indicates that the modelling technique used in the finite difference grid network around the sources is a valid theoretical method to account for the localised dispersion.

The predictions from the finite difference solution compare well with those obtained experimentally for load capacity, flow rate, radial stiffness and restoring torque. Both experimental data obtained by the Author and that obtained independently at Liverpool Polytechnic have been used for comparison.

The predictions from the corrected line feed model have been shown to give reasonably accurate results for bearing characteristics at $\varepsilon \leqslant 0.5$, with discrepancies between theory and experiment being less than 15%. This model is more convenient to use than the finite difference analysis as generalised design data can be obtained. For the case of single plane admission bearings, the predictions for torque stiffness are shown to give greater correlation with experiment than the data presented by M.T.I.

In contrast, the finite difference solution gives a unique solution for a particular set of bearing variables. This method is more applicable to cases where greater accuracy is required in the prediction of bearing performance, and is particularly useful for the analysis of manufacturing errors.

11. ANALYSIS OF MANUFACTURING ERRORS

11.1 Introduction

In the previous section, it was shown that the finite difference solution gives an accurate theoretical model. Having established a theoretical technique which provides close correlation with experiment, it is now possible to investigate analytically the extent to which errors in manufacture affect bearing performance.

Inevitably even bearings which are manufactured to very high standards will contain small deviations from the design condition. These variations, although small in size terms, are likely to to be large when considered in relation to the designed bearing clearance. It is the relationship between the flow characteristics of the control device, in this case orifices, and the flow through the bearing clearance which substantially affects the load and stiffness characteristics of the bearing.

Errors in bearing clearance due to the application of manufacturing tolerances to journal and sleeve diameters in addition to errors in form, such as taper and out-of-roundness, affect the bearing performance. Other errors can include errors in orifice diameter, mismatched orifices, bearing misalignment and local rising around the pocket when inserts are press-fitted.

The aim of this section is to present in useful graphical form the quantitive effects of such errors on bearing load capacity. The study is confined to journal bearings having pocketed orifices.

11.2 Variation of Load Capacity with Orifice Diameter and Bearing Clearance

It has previously been shown that non-dimensional load capacity $\overline{W}$ varies with feeding parameter $\Lambda_s \xi$. Figure 10.4 discussed in Section 10 , illustrates that good correlation exists between theory and experiment for a wide range of feeding parameters and for eccentricity ratios up to $\varepsilon = 0.8$.

An important characteristic of Figure 10.4 is the existence of maximum load capacities which occur in the range of $0.34 < \Lambda_s \xi < 0.5$. The optimum value of $\Lambda_s \xi$ is achieved by the correct selection of orifice diameters d_o and bearing radial clearance h_o thus:-

$$\Lambda_s \xi = Z \frac{d_o^2}{h_o^3}$$

$$Z = \frac{6 \pi \sqrt{RT}\, n}{4 p_o \sqrt{1+\delta_o^2}} \cdot \frac{L}{D}$$

(for good design : $\delta_o \leq 0.5$)

To achieve both high stiffness at small eccentricities and good load capacity at high eccentricity, the design value for the feeding parameter has been suggested previously at $\Lambda_s \xi = 0.42$ (Ref. 7.12) .

11.2.1 Variations in Bearing Clearance

Figure 11.1 demonstrates how load parameter $\overline{W}$ is affected by variations in clearance from the design condition (i.e. $\Lambda_s \xi = 0.42$). The horizontal axis shown is the ratio of the bearing deflection e to the optimum clearance h_o (opt). Hence for the variations of h_o of -20% and +20%, the ratio e/h_o (opt).has a maximum value of between 0.8 and 1.2 respectively corresponding to touch-down conditions.

It can be seen that two effects come into play - available bearing movement and load capacity. As h_o is decreased, less available movement is possible from the concentric position. In addition lower load capacity is achieved for a given eccentricity ratio; but this is off-set by the reduction in the clearance, resulting in slightly higher stiffness at low eccentricities, and has been discussed previously (Ref. 7.12).. Maximum concentric stiffness is achieved at approximately h/h_o (opt) = 0.85.

As clearance is increased from h_o (opt) the maximum load capacity is marginally increased although concentric stiffness is much reduced. In general it is preferred to have manufacturing variations leading to slightly smaller clearances if stiffness is a major consideration. If maximum load is the major consideration then manufacturing tolerances leading to small increases in bearing clearance are to be preferred.

11.2.2 Variations in Orifice Diameter

Figure 11.2 illustrates how variations in d_o affects load capacity. Although small reductions in orifice diameter slightly improve load capacity at high eccentricities, stiffness at low eccentricities is marginally reduced. Increasing orifice diameter causes a reduction in both load capacity and stiffness. It should be noted that the variation in load capacity at an eccentricity ratio $\varepsilon = 0.5$ is very small for the values of d_o shown in Figure 11.2 . For d_o/d_o (opt) between 0.8→1.2, the load capacity is within 5% of that achieved for the optimum conditions. It can be seen from Figure 11.2 that, in general, it is better that errors tend to give under-sized orifices because of the increased protection against overload conditions.

11.3 Mismatched Orifices

The effect of mismatched orifices is an important aspect to consider as variations can occur in the diameter of orifices. In the case where 'bought-in' jewels are employed, variations in size can exist within the same batch.

When orifices vary in size and these variations are not equal and opposite, the journal takes up a null position which does not coincide with the geometric centre of the bearing sleeve. Numerous combinations of errors are possible and the magnitude of their individual effect are varied. Figure 11.3(a) illustrates the extreme effects of selected combinations of mismatch on the load deflection characteristics from the null position.

It can be seen that up to deflections of 0.5 h_o, mismatched orifices have minimal effect on loading characteristics, but at greater deflections large differences occur. This has also been found experimentally by Stowell et. al. (Ref. 7.14). The available deflection and the maximum load capacity are dependent upon both the degree of mismatch and the relationship of the mismatched orifices to the loading direction.

Figure 11.3(b) summarizes the effect of mismatch on eccentricity at zero load. Mismatch in orifices normal to the direction of loading will cause a displacement in that plane, but such effects will have minimal effect on the displacement in the direction of loading.

Figure 11.3(a) when used in conjunction with Figure 11.3(b) allows a full assessment of the effect of orifice variations to be evaluated for the extreme cases.

As a final comment it may be possible to purposely mismatch orifices to achieve effectively a pre-loaded bearing, thus enhancing load capacity in one direction.

11.4 Form Errors

During the manufacture of the journal and sleeve diameters, errors in cylindricity occur. The most significant of these errors include parallelism (which can take the form of taper, bellmouthing or barrelling) and roundness. Although small in absolute size terms, these errors can be large when considered in relation to the design bearing clearance.

11.4.1 Non-Parallelism

The equations which describe the bearing clearance for the conditions of taper, bellmouthing and barrelling are given in Appendix E . The effects of these various geometries on load capacity are shown in Figure 11.4 and compared to an idealised bearing without errors. h_o is defined at the datum shown and refers to the average radial bearing clearance. The degree of non-parallelism specified refers to the maximum deviation of the clearance along the bearing expressed as a percentage of the average clearance.

For example, a bellmouthing of 20% h_o gives radial clearance of 1.1 h_o and 0.9 h_o at the ends and at the centreplane of the bearing respectively. Similarly, a taper of 40% gives radial clearance of 0.8 h_o and 1.2 ho at either end of the bearing.

It can be seen that taper has the least effect on load parameter. In comparison, bellmouthing causes a large drop in load capacity - a 40% h_o bellmouthing reduces load capacity by approximately 12% at high eccentricity ratios. An interesting effect is that of barrelling where the geometric effect causes an improvement in load capacity. This trend may be explained by consideration of the pressure profile within the bearing. If barrelling exists, the axial pressure profile assumes a more convex shape due to the clearance profile which enhances load capacity, whilst for bellmouthing the

opposite occurs. If excessive barrelling is present, it can be expected that an increase in the circumferential flow off-sets the enhancement in axial pressure profile to give a reduced load capacity. Computer results suggest that an optimum degree of barrelling exists at approximately 50% which gives a maximum load capacity condition.

11.4.2 Out - Of - Roundness

A further significant geometric error is out-of-roundness as shown in Figure 11.5 . The extreme case of ovality is shown (two lobed case). Higher order lobing has a reduced effect on operational performance. Out-of-roundness is defined as MZC relative to the average radial clearance h_o. It can be seen that dependent upon the directionality of the ovality with respect to the loading plane, the effect of out-of-roundness can either enhance or reduce load capacity. The equations which describe bearing clearance with ovality is given in Appendix E .

11.4.3 Bearing Tilt

The effect of tilt on load capacity is shown in Figure 11.6 and is an effect caused by the misalignment of the housings during assembly or by the application of off-set loadings. Tilt eccentricity ratio e_t/h_o is defined as the displacement of the journal centreline at the extreme edges of the bearing from its centre plane position and is expressed as a ratio of the bearing radial clearance h_o. As shown, the major effect on operation is the reduction in the available bearing movement. This has been demonstrated experimentally in Refs. 2.2, 9.1, 11.1, 2.19 .

11.5 Local Burring at Edge of Pocket

In the manufacture of bearings with pocketed orifices, it is common practice to press-fit either watch-makers jewels or brass bushes into supply holes in

the bearing bore. This operation produces local rising around the pocket and it has been reported that this effect can be in the order of 5 μm (Ref. 2.17) . If the final sizing of the bearing bore is carried out before insertion of the jewels it can be very difficult to totally eliminate the local rising around the pockets without recourse to re-machining.

This phenomenon can have a large influence on bearing load capacity, because it affects local conditions at the entrance to the film. Fig. (a) below shows the clearance profile of a bearing with burring, designated by b_R. This is assumed constant for all pockets. It is also assumed that the burr extends to and terminates at the grid positions surrounding the pocket. The reduction in load capacity due to local burring is illustrated in Figure 11.7 .

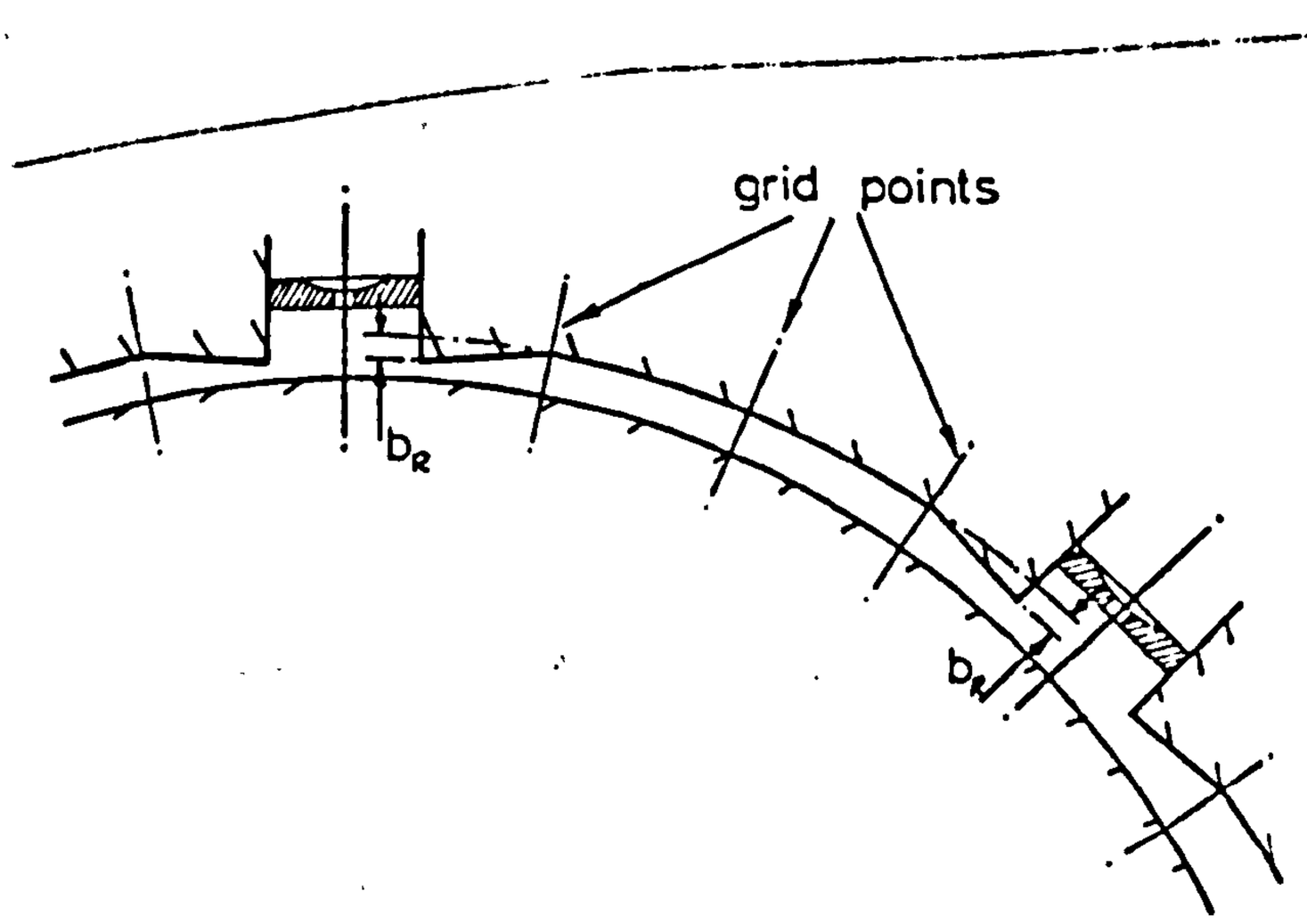

Fig. (a) Representation of burring at edge of pockets

11.6 Analysis of Errors in Experimental Bearings

The effect of manufacturing errors on load capacity is shown in Figure 11.8. Bearings having either pocketed orifices Figure 11.8(a) or inherently compensated orifices Figure 11.8(b) has been considered. The experimental curves shown have been obtained by the Author (Ref. 2.2) .

For these bearings, the radial clearances have been established by air gauge equipment supplied by Thomas Mercer Ltd. The error in these readings was dependent upon the accuracy of the setting masters as quoted by calibration certificates supplied by the manufacturers.

Each orifice was examined under a tool-makers microscope and their diameter was determined. From these results, tolerances were established for the assumed orifice diameter.

The bearing bush and test shaft were hand lapped in order to achieve a good geometric form. The components were rigorously measured on a form measuring machine (Cynform) and using air gauges. The results are shown below:

	Bearing Bush	Shaft
out-of-roundness MZC μm	0.2 → 0.3	0.4
taper in diameter :		
air gauge μm	0.8	<0.6
Cynform μm	0.7	<1.0
straightness μm	0.15	<0.4

The effect of ovality and straightness can either enhance or reduce load capacity dependent upon their directionality with respect to loading.

For the bearing with pocketed orifices shown in Figure 11.8(a) , two theoretical models have been presented - one that includes burring at the entrance to the film, the other neglecting its effect. It can be seen that if only errors in form and orifice diameters are taken into account (without burring), the experimental results fall outside the error band. However, if burring is included, theory and experiment are in agreement. The greatest impact on load capacity is due to burring because it affects local conditions at the entrance to the film whereas form errors prevail throughout the entire bearing area.

The bearing with inherently compensated orifices is shown in Figure 11.8(b) . Two theoretical models are shown , one which includes pressure recovery, the other neglects pressure recovery. It can be seen that the error band applicable for the case of neglecting pressure recovery gives the better correlation with experiment.

11.7 Conclusions

The major errors of dimension and form have been described in this section and the magnitude of the effects presented. It becomes evident therefore that if variations exist and are not detected, large discrepancies are likely to exist between theory and practice.

The finite difference analysis used is able to take into account these variations of manufacture. By accounting for tolerances on measurement and errors of form, experimental bearings have been analysed and their maximum and minimum load conditions established. It is shown that experimental results fall within the tolerance band for both pocketed and inherently compensated bearings.

It is likely that small discrepancies between experiment and theory noted previously can be accounted for by the effects of manufacturing errors.

12. GENERAL CONCLUSIONS

The results from the corrected line feed model have been presented. This model gives an approximate design method. The data presented are an advancement of that previously given by M.T.I. as a wide range of l/λ values have been considered. The analysis neglects dispersion losses local to the orifice due to clearance variations. For this reason, the analysis over-estimates load capacity, which increases as ε increases and n decreases. For $\varepsilon \leq 0.5$, $n \geq 6$ and $d/D \geq 0.01$, the corrected line feed model gives results to an accuracy within 15% when compared with experiment.

Greater accuracy can be obtained from the finite difference analysis, as dispersion effects local to each source are accounted for. By comparing the results from the finite difference solution with those from the complex potential theory and experimental data, it has been established that bearing film pressures including those local to the source are accurately predicted. This validates the modelling technique used around the sources. The finite difference method gave predictions which correlated with experiment to within typically 10% for load capacity, flow rate, stiffness and restoring torque. However, this method gives a unique solution for a particular set of data and would seem more applicable for design studies where greater accuracy is required.

The finite difference method has been used to examine the effects of manufacturing errors on bearing performance. Each of these errors has been considered independently and their effects presented. Also, by accounting for the tolerances in measurement and form, experimental bearings have been analysed and a theoretical error band established. It has been shown that experimental results fall within this band. This indicates that differences between theory and experiment can be largely attributed to the effects of manufacturing errors.

PART D

HYBRID PERFORMANCE OF JOURNAL BEARINGS

PART D - HYBRID PERFORMANCE OF JOURNAL BEARINGS

13. INTRODUCTION

In Part C, the aerostatic performance of externally pressurised journal bearings was examined, where the load carrying capacity was derived exclusively from external pressurisation which is applicable for conditions of zero or low rotational speeds. In this part, the effect of rotational speed is considered where velocity induced flows, generated by aerodynamic effects, are superimposed on the aerostatic conditions. Operating under these conditions, with combined aerostatic and aerodynamic components, these bearings are termed 'hybrid' and exhibit the characteristic where load capacity increases with speed.

Figure 13.1 illustrates a typical bearing geometry. The restrictors are in the form of small diameter orifices that are equally spaced around one or more axial planes. The effect of rotation is to produce an attitude angle ϕ between the load vector and the line of minimum/maximum film clearance.

The bearing can be operated in one of three modes:

1. Purely aerostatically - pressurised without rotation

2. Purely aerodynamically - not pressurised but rotating

3. Hybrid mode - both pressurised and rotating

For a complete understanding of these bearings, all three modes of operation need to be considered. The aerostatic performance has already been dealt with in the previous chapter. The aerodynamic and hybrid performance will be considered separately in this study.

13.1 Literature Review

13.1.1 Aerodynamic Performance*

One of the earliest theoretical treatments was presented by Ausman in 1957 (Ref. 13.1). This used a first-order perturbation technique which was applicable only for low eccentricity ratios. This was improved upon for higher eccentricity ratios by Ausman in 1961 (Ref.13.2) by using a 'linearised ph' solution.

Another method to solve the non-linear partial differential equations is an iterative solution using finite difference approximations. These have been proposed by Gross in 1959 (Ref. 13.3), Raimondi (Ref. 13.4) in 1961 and Elrod and Malanoski (Ref. 13.5) in 1965.

13.1.2 Hybrid Performance

Experimental work presented by Powell (Ref. 13.6) on hybrid bearings in 1962 showed that the increase in load capacity over and above aerostatic load capacity was approximately proportional to compressibility number based on supply pressure conditions. This idea was followed up by a superposition method proposed by Powell (Ref. 13.7) in 1964. This involved vector addition of the aerostatic and aerodynamic loads, the latter dependent upon supply conditions. Subsequent publications in the form of design methods in 1964 (Ref. 7.4) and 1971 (Ref. 7.5) have proposed empirical factors of 0.74 and 0.7 respectively to correct the aerodynamic loads to give improved correlation with results obtained experimentally. Although the empirical factors must be used with caution as they have been derived for a specific bearing geometry, the design method does provide a rapid solution and can be used to give an approximate estimation of hybrid load capacity.

* The aerodynamic performance refers to a plain cylindrical journal bearing (without feeding holes).

Other analyses have been developed from a purely theoretical standpoint. One such analysis which assumes a line feed model and employs a first-order perturbation method has been presented using the linearised pressure solution by Lund in 1964 (Ref. 7.8) and subsequently in 1967 using the linearised ph solution (Ref. 4.4) similar to that used by Ausman (Ref. 13.2). An experimental programme conducted by Cunningham, et.al. (Ref. 13.8) in 1969 showed that the small eccentricity pressure perturbation theory gave better agreement than the linearised ph solution when compared with experiment.

M.T.I. (Ref. 2.11) published design data in 1967 for hybrid bearings based upon the analysis by Lund (Ref. 4.4). The data presented only applies to centrally fed orifice bearings with supply pressures of 5 and 10 atmospheres, which limits its applicability. However, the design data presented for these bearings gives guidance to avoid pneumatic hammer instability as well as recommendations for the selection of the line feed parameters. Confidence in the predictions is somewhat limited as no experimental verification is given and a safety factor of 1.5 is recommended.

More recently, attempts have been made to improve the modelling of the feedin planes. The refinement involves considering individual orifices and computin their flows rather than, as Lund assumed in Ref. 4.4, a line feed model. Analyses which employ this approach include those by Elrod and Glanfield (Ref. 2.12),Majumdar (Ref. 13.9) and Kazimierski (Ref. 6.4). To date however, these analyses have not been exploited to give generalised data in the form of a design method.

The results from an experimental study on hybrid bearing characteristics has been presented by McFarlane and Reason (Ref. 13.10). In addition to giving load/deflection data, experimental pressure profile measurements have also been obtained.

13.2 Aim and Scope of the Investigation

The present study concerns steady state performance. The aims of this study are:

1. To present a theoretical analysis based upon finite difference techniques for the aerodynamic performance of plain cylindrical bearings, and to compare results with the existing analytical methods.

2. To examine the simplified theoretical approach of linear superposition.

3. To present a theoretical analysis based upon finite difference techniques for the hybrid bearings and to indicate the effect of changing various design parameters on bearing performance.

4. To compare the theoretical results from the finite difference solution with results produced by superposition methods and M.T.I. predictions.

5. To compare the theoretical results with experimental data in order to deduce their accuracy and validity.

14. THEORETICAL STUDY

14.1 Aerodynamic Performance

14.1.1 Plain Cylindrical Bearings

An important aspect of this work is to predict accurately the aerodynamic component of hybrid bearings. For this reason, a theoretical analysis is presented for plain cylindrical bearings (in which the surface is continuous and uninterrupted). The results of the analysis will be compared with those from other published results. This ensures that the velocity induced flow component is accurately taken into account, and increases confidence when these techniques are incorporated into the hybrid analyses.

In order to account for two dimensional flow, a finite difference method has been used to account for velocity induced and pressure induced flow. The latter refers to the viscous flow from a high pressure area to a low pressure area, the pressure difference being generated by velocity induced flow. The pressure induced flow does not refer to an external pressure source, but to an internally generated pressure.

The finite difference method used has been presented in a general form in Section 6. The shape factors applicable to the finite difference grids in Figure 8.2 are as follows:

pressure induced flow:

$$GA = \frac{L}{2(JSPAN)} \cdot \frac{(IDIV)}{\pi D}$$

velocity induced flow:

$$\Delta X = \frac{L}{2(JSPAN)}$$

Summing mass flow rates at a point and equating to zero with cancellation gives:

$$0 = \bar{H}(i)\left\{\bar{P}(i,j+1) - \bar{P}(i,j)\right\}\frac{1}{GA}$$

$$+ \bar{H}(i)\left\{\bar{P}(i,j-1) - \bar{P}(i,j)\right\}\frac{1}{GA}$$

$$+ GA\left\{\bar{P}(i+1,j) - \bar{P}(i,j)\right\}\left\{\frac{\bar{H}(i+1)+\bar{H}(i)}{2}\right\}$$

$$+ GA\left\{\bar{P}(i-1,j) - \bar{P}(i,j)\right\}\left\{\frac{\bar{H}(i-1)+\bar{H}(i)}{2}\right\}$$

$$+ \frac{2C_N}{J_{DIV}}\cdot\frac{L}{D}\left\{\frac{\bar{h}(i+1)+\bar{h}(i)}{2}\right\}\left\{\frac{\bar{P}(i+1,j)+\bar{P}(i,j)}{2}\right\}$$

$$- \frac{2C_N}{J_{DIV}}\cdot\frac{L}{D}\left\{\frac{\bar{h}(i-1)+\bar{h}(i)}{2}\right\}\left\{\frac{\bar{P}(i-1,j)+\bar{P}(i,j)}{2}\right\}$$

where $C_N = \dfrac{6\eta\omega r^2}{p_a h_o^2}$; $\bar{p} = \dfrac{p}{p_a}$, $\bar{P} = \bar{p}^2$; $\bar{h} = \dfrac{h}{h_o}$, $\bar{H} = \bar{h}^3$

..... (14.1)

The term C_n is referred to as 'compressibility number'.

The analysis was used in a computer program to calculate film pressures and bearing performance. The boundary at j = 1 was fixed at ambient pressure $\bar{P} = 1$, and a half-bearing solution was obtained. The input variables were L/D, compressibility number C_n, and grid spacings as defined by JDIV and IDIV and shown in Figure 8.2.

The grid pressures were continuously relaxed until convergence was achieved. It was found that by using initial grid pressures given by Ausman (Ref.13.2), in preference to ambient conditions, the computer process time was reduced and instability problems overcome.

Load capacity is calculated by numerical integration as given in Section 8.

The effect of C_n on the load carrying capacity and attitude angle ϕ is shown in Figure 14.1. At low values of C_n, load capacity increases linearly with C_n - a characteristic predicted for incompressible fluids as given by Sommerfeld. However, at high values of C_n, the load capacity for a compressible fluid approaches a constant asymptotic value.

From Figure 14.1(b), it can be seen that as $C_n \rightarrow 0$, the value of $\phi \rightarrow 90°$ and as $C_n \rightarrow \infty$, $\phi \rightarrow 0°$. This means that at low values of C_n, deflections are almost at right angles to the load vector, whereas at high values of C_n, deflections are almost in line with the load vector.

Load capacity is plotted against ε for various C_n in Figures 14.2 and 14.3 for L/D = 1 and 2 respectively. The theoretical results from the finite difference solution are compared also with other theoretical models. It can be seen that all the theoretical solutions predict that at low eccentricities, ($\varepsilon \leqslant 0.2$) film stiffness is approximately constant, but as eccentricity increases further, greater film stiffness is predicted. Another feature shown is that increasing C_n and/or L/D, gives greater load capacity for the range of parameters shown.

The finite difference results obtained from this study compare very well (within 1%) with those from other iterative techniques given by Raimondi (Ref. 13.4) and Elrod and Malanoski (Ref. 13.5) for the load deflection characteristics up to $\varepsilon \leqslant 0.8$. The results from Ausman (Ref. 13.2) correlate exactly with the finite difference solution for low eccentricities; but at higher eccentricities increasing disparity occurs. This is to be expected as the analysis used by Ausman is more applicable to low eccentricities, as discussed in Section 13.

14.1.2 Orifice Compensated Bearings

The published literature contains little information relating to the effect of the orifice supply holes on the aerodynamic performance. The only information available is that which has been obtained experimentally; no analytical treatment has been proposed to account for the effect of the supply holes.

The presence of the holes in the bearing wall under aerodynamic conditions can be expected to derate load carrying capacity. This can be explained by considering a plain bearing (without holes) and examining a typical pressure profile shown below:

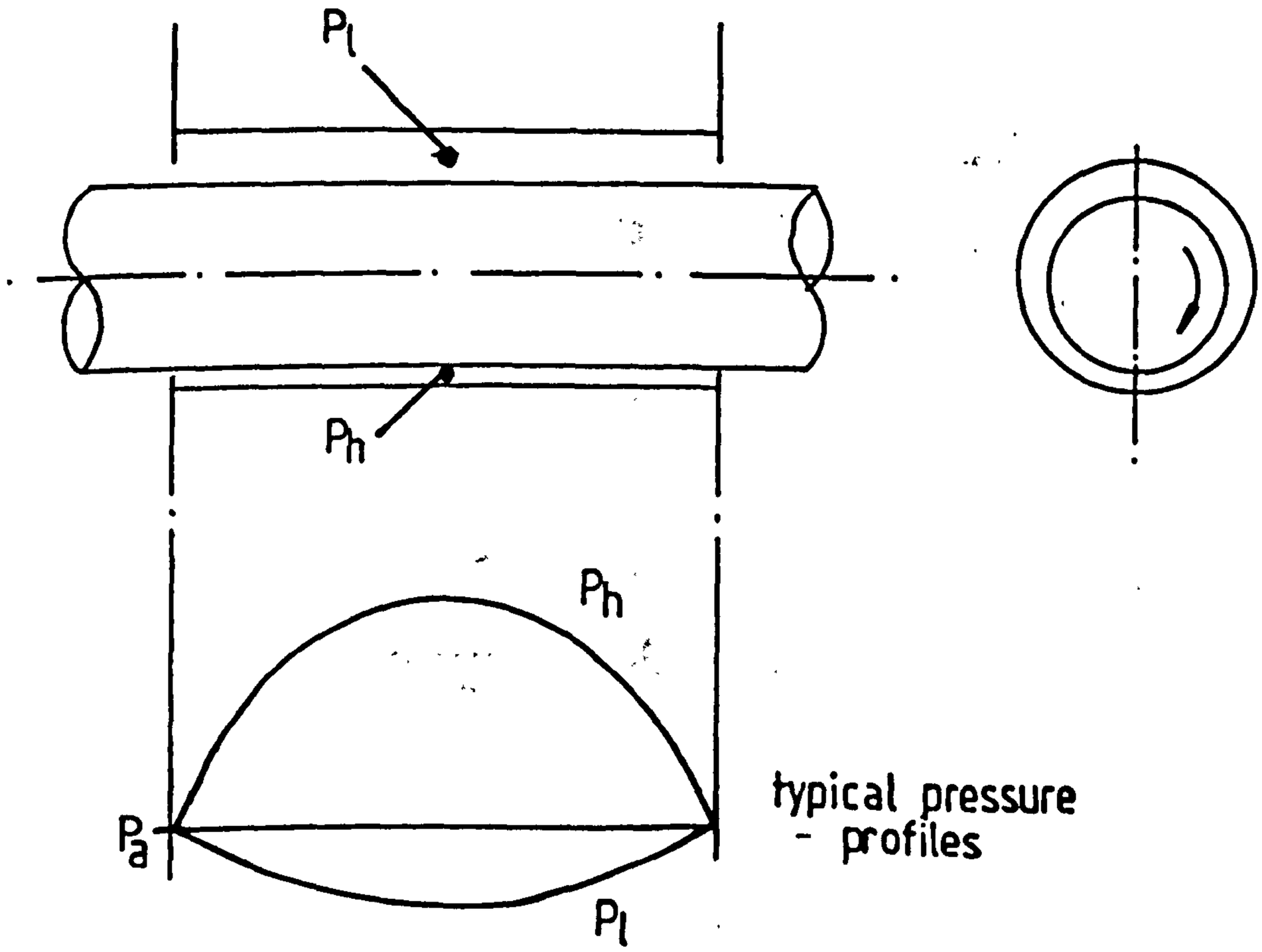

typical pressure - profiles

To assist with the understanding, the orifices are replaced for convenience with a continuous slot in the plane of feeding. In the high pressure side p_h, the slot provides a pressure sink and in the low pressure side (sub-ambient) the slot provides a pressure source. If no restriction exists then the slot would correspond to atmospheric pressure.

The double admission bearing would approximate to the operation of three single units - comprising of a central section plus two outboard sections, as shown below:-

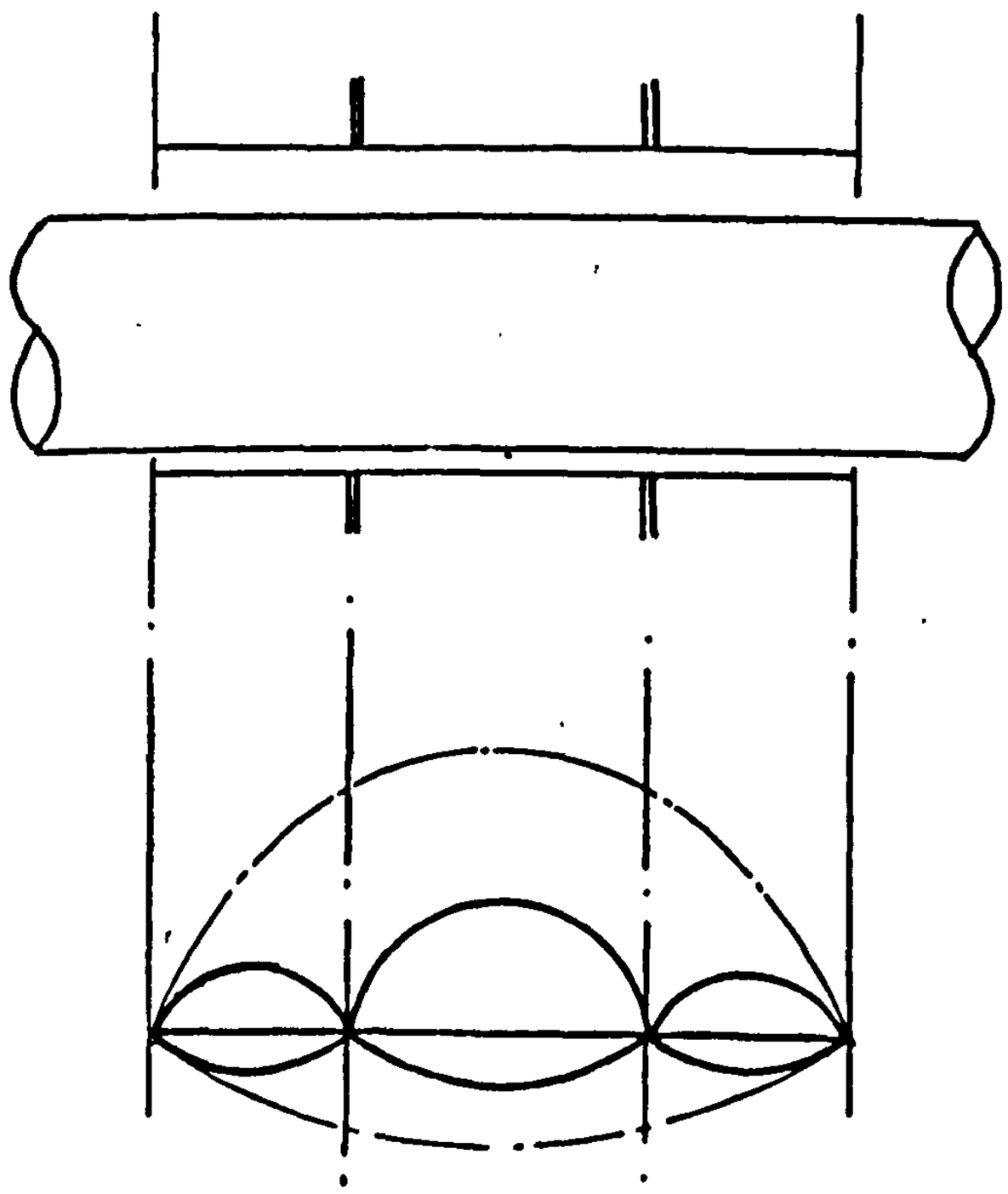

The presence of the discrete holes rather than a slot in conjuction with the restriction afforded by these orifices have the effect of modifying the pressures as shown below:

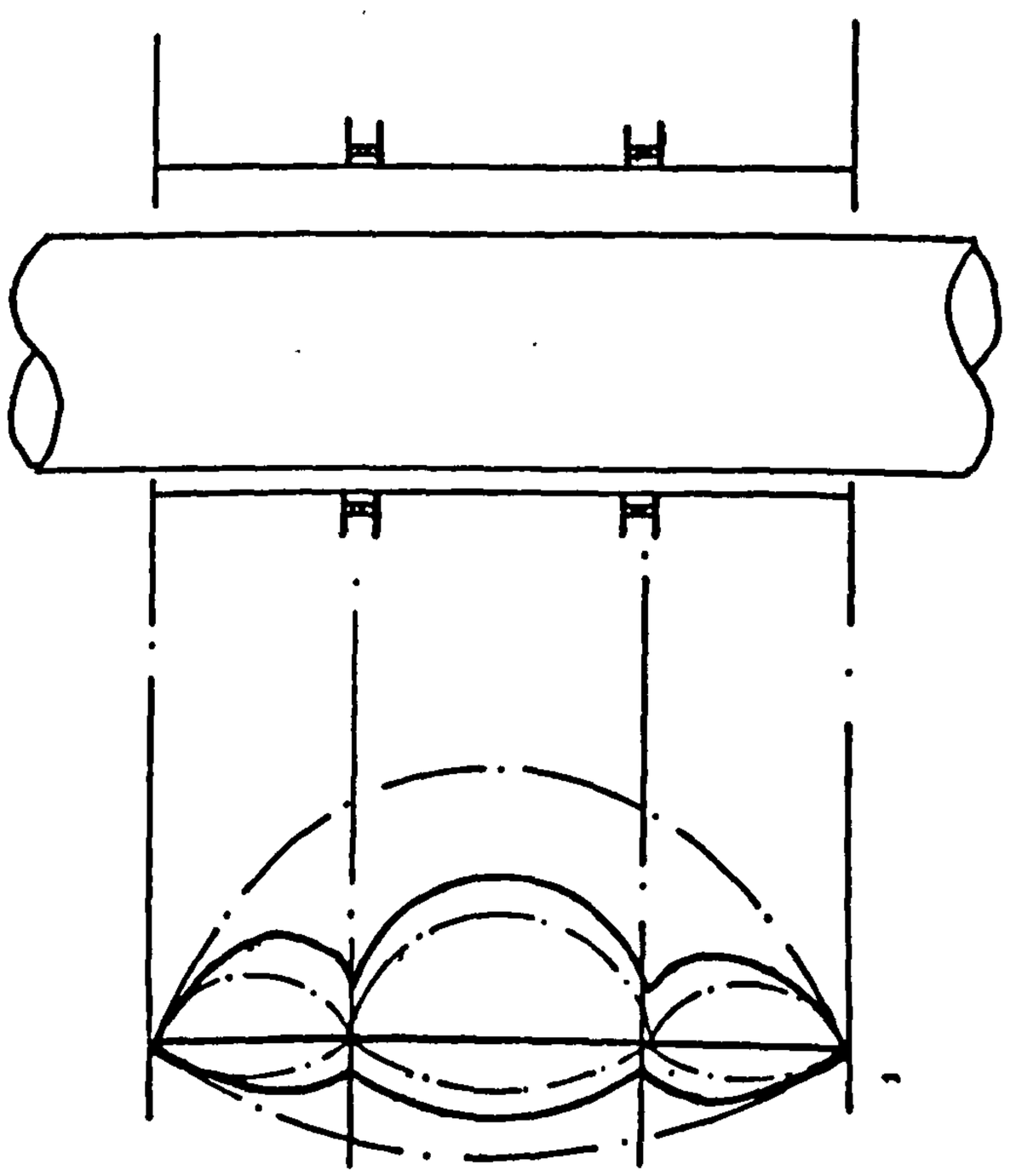

In this study it is assumed that the orifice planes are at atmospheric pressure conditions. Although this approach would tend to under-estimate bearing load capacity, the results can be expected to give a more realistic value than if the effect of the inlet planes were ignored.

14.2 Hybrid Performance

14.2.1 Powell's Method of Superposition

The method of linear superposition has been proposed by Powell (Ref. 13.6). This involves vector addition of the aerostatic and aerodynamic loads, as shown in Figure 14.4. The resultant load W_{res} is composed of the radial load and tangential load as shown. This method has been used as a design

method by Powell in Refs. 7.4 and 7.5. It was recognised that the compressibility number, which is dependent upon ambient pressure conditions for aerodynamic bearings, is modified due to external pressurisation. Difficulty arises in the choice of the mean bearing pressure. This pressure is dependent upon the following factors:

1. Pressure immediately downstream of orifice
2. Shape of the pressure distribution
3. Effect of eccentricity on local film pressures

It has been suggested by Gross (Ref. 14.1) that the mean pressure P_m is given as:

$$p_m = \frac{1}{2}(p_o - p_a)$$

The effective compressibility number is given as:-

$$(C_N)_m = \frac{6\eta\omega r^2}{p_m h_o^2} = \frac{C_N}{p_m/p_a}$$

The load capacity is modified thus:-

$$(W_A)_m = W_A \cdot \frac{p_m}{p_a}$$

It has been proposed by Powell that the effect of errors in specifying P_m on the resultant load capacity is small. This is because typical hybrid bearings have low values of $(C_n)m$, usually less than unity, and therefore

these bearings will be operating in the near incompressible region, where load capacity is proportional to compressibility number. The aerodynamic load capacity calculated by this method is modified thus:-

$$W_A' = k' . W_A$$

where k′is a correction factor

Experimental results obtained by Powell indicated that for single admission bearings with L/D = 2, $k' = 0.7$. (Ref. 7.5). It was pointed out in this reference that this factor must be applied with caution for other L/D ratios.

14.2.2 Modified Superposition Method

As discussed previously for orifice bearings operating aerodynamically, the full aerodynamic component is not realised due to the influence of the supply holes. It is speculated that because of their influence, the aerodynamic load has to be derated in Powell's design method, using an empirical factor, in order to correlate theory and experiment.

It is therefore proposed that a modified superposition method be considered which differs from Powell's method in the manner in which the aerodynamic component is calculated.

(a) Double Plane Admission

The aerodynamic component is calculated on the assumption that a bearing with two plane admission is divided into three separate bearings, and that each of these bearings operates aerodynamically in an ambient pressure which is equal to their respective mean bearing pressures.

where $\frac{p_m}{p_a} \simeq \frac{p_d}{p_a}$ for the central section

and $\frac{p_m}{p_a} \simeq \frac{p_d/p_a + 1}{2}$ for the outboard sections

Both the compressibility number and load capacity are modified thus:

$$(C_N)_m = \frac{C_N}{p_m/p_a}$$

$$(W_A)_m = W_A \cdot \frac{p_m}{p_a}$$

(b) Single Plane Admission

The approach described above can also be applied to central admission bearings. In this case, the aerodynamic load is calculated by dividing the bearing into two separate bearings and assuming that its ambient pressure is equal to:

$$\frac{p_m}{p_a} \simeq \frac{p_d/p_a + 1}{2}$$

14.2.3 Finite Difference Solution

The accuracy of predicting hybrid performance is dependent upon the accuracy of predicting the aerostatic and aerodynamic performance. It has been shown in Part C that the results of the finite difference solution for aerostatic bearings correlate well with experiment. This was achieved by accounting for the discrete nature of feeding and by employing a suitable restrictor loss analysis. The same analysis was used for hybrid bearings, but in this case, the velocity induced flow component was included.

The finite difference method used has been presented in a general form in Section 6. For pocketed orifices, the restrictor loss analysis employed is that defined by Equations 2.13 and 2.18, which neglects pressure recovery in the bearing film but includes allowance for a varying C_d.

For inherently compensated orifices, the restrictor loss analysis as given by Equation 2.8 is used. This neglects pressure recovery, inertia effects and supersonic flow domains within the bearing clearance.

The grid network used in the computation is shown in Figure 8.3. With reference to Section 6, the shape factors for the finite difference grid are given below:-

pressure induced flow:

$$GA = \frac{L}{2(JSPAN)} \cdot \frac{(IDIV)}{\pi D}$$

velocity induced flow:

$$\Delta X = \frac{L}{2\,(JSPAN)}$$

(a) Grid Points Surrounding the Restrictor

(i) Axial Direction

The flow to grid points $(i, j \pm 1)$ in the axial directions downstream of the restrictor was considered from four directions; radial flow from the restrictor at position (i,j) and parallel slot flow from the other surrounding points $(i, j \pm 2)$, $(i+1, j \pm 1)$ and $(i-1, j \pm 1)$.

Summing flows, cancelling and rearranging gives:

$$\bar{P}(i, j \pm 1) =$$

$$\Big[\Big\{ \bar{P}(i,j)\, 2\bar{H}(i)\, GARJ \Big\} + \Big\{ \bar{P}(i, j \pm 2)\, \frac{\bar{H}(i)}{GA} \Big\}$$

$$+ \Big\{ \bar{P}(i+1, j \pm 1) \Big[\bar{H}(i) + \bar{H}(i+1) \Big] \frac{GA}{2} \Big\} + \Big\{ \bar{P}(i-1, j \pm 1) \Big[\bar{H}(i) + \bar{H}(i-1) \Big] \frac{GA}{2} \Big\}$$

$$+ \frac{C_N}{2\, JSPAN} \frac{L}{D} \Big\{ \bar{P}(i-1, j \pm 1) + \bar{P}(i, j \pm 1) \Big\} \Big\{ \bar{L}(i-1) + \bar{L}(i) \Big\}$$

$$- \frac{C_N}{2\, JSPAN} \frac{L}{D} \Big\{ \bar{P}(i+1, j \pm 1) + \bar{P}(i, j \pm 1) \Big\} \Big\{ \bar{L}(i+1) + \bar{L}(i) \Big\} \Big] \Big/$$

$$\Big[2\, \bar{H}(i)\, GARJ + \frac{\bar{H}(i)}{GA} + \Big\{ \bar{H}(i) + \bar{H}(i+1) \Big\} \frac{GA}{2} + \Big\{ \bar{H}(i) + \bar{H}(i-1) \Big\} \frac{GA}{2} \Big]$$

where $$GARJ = \frac{\tan^{-1}\left(\frac{1}{2\, GA}\right)}{\log_e \left[\frac{2a}{Jo\, div\, df} \right]}$$

(ii) Circumferential Directions

The flow to grid points $(i \pm 1, j)$ in the circumferential directions downstream of the restrictor was considered in four directions; radial flow from the restrictor at position (i,j) and parallel slot flow from the other surrounding points.

$$\bar{P}(i\pm1,j) =$$

$$\left[\left\{\bar{P}(i,j)\left[\bar{H}(i)+\bar{H}(i\pm1)\right]GARI\right\}+\left\{\frac{\bar{P}(i\pm1,j\pm1)\ \bar{H}(i)}{GA}\right\}\right.$$

$$-+\left\{\bar{P}(i\pm1,j-1)\frac{\bar{H}(i)}{GA}\right\}+\left\{\bar{P}(i\pm2,j)\left[\bar{H}(i\pm1)+\bar{H}(i\pm2)\right]\frac{GA}{2}\right\}$$

$$\mp\ \frac{C_N}{2\ JSPAN}\ \frac{L}{D}\left\{\bar{P}(i\pm1,j)+\bar{P}(i,j)\right\}\left\{\bar{L}(i\pm1)+\bar{L}(i)\right\}$$

$$\left.\pm\ \frac{C_N}{2\ JSPAN}\ \frac{L}{D}\left\{\bar{P}(i\pm2,j)+\bar{P}(i\pm1,j)\right\}\left\{\bar{L}(i\pm2)+\bar{L}(i\pm1)\right\}\right]\Big/$$

$$\left[\left\{\bar{H}(i)+\bar{H}(i\pm1)\right\}GARI+\frac{2\bar{H}(i)}{GA}+\left\{\bar{H}(i\pm1)+\bar{H}(i\pm2)\right\}\frac{GA}{2}\right]$$

where $$GARI = \frac{\tan^{-1}\left(GA/2\right)}{\log_e\left[\frac{2\pi D}{(IDIV)\,df}\right]}$$

(iii) Diagonal Flow Directions

The flow to grid points in the combined axial and circumferential directions was considered from five directions; radial flow from the restrictor position (i,j) and parallel slot flow from the surrounding grid points.

$$\bar{F}(i\pm1, j\pm1) =$$

$$\left[\left\{\bar{P}(i,j)\left[\bar{H}(i)+\bar{H}(i\pm1)\right]\frac{GARJI}{2}\right\}+\left\{\bar{P}(i\pm1,j)+\frac{\bar{H}(i\pm1)}{GA}\right\}\right.$$

$$+\left\{\bar{P}(i\pm1,j\pm2)\,\frac{\bar{H}(i\pm1)}{GA}\right\}+\left\{\bar{P}(i\pm2,j\pm1)\left[\bar{H}(i\pm2)+\bar{H}(i\pm1)\frac{GA}{2}\right\}\right.$$

$$\pm\frac{C_N}{2\,JSPAN}\frac{L}{D}\left\{\bar{P}(i\pm2,j\pm1)+\bar{P}(i\pm1,j\pm1)\right\}\left\{\bar{L}(i\pm2)+\bar{L}(i\pm1)\right\}$$

$$\mp\frac{C_N}{2\,JSPAN}\frac{L}{D}\left\{\bar{P}(i\pm1,j\pm1)+\bar{P}(i,j\pm1)\right\}\left\{\bar{L}(i\pm1)+\bar{L}(i)\right\}$$

$$\left.+\left\{\bar{P}(i,j\pm1)\left[\bar{H}(i)+\bar{H}(i\pm1)\right]\frac{GA}{2}\right\}\right]\Bigg/$$

$$\left[\frac{2\,\bar{H}(i\pm1)}{GA}+\left\{\bar{H}(i)+\bar{H}(i\pm1)\right\}\frac{GARJI}{2}\right.$$

$$\left.+\left\{\bar{H}(i\pm2)+\bar{H}(i\pm1)\right\}\frac{GA}{2}+\left\{\bar{H}(i)+\bar{H}(i\pm1)\right\}\frac{GA}{2}\right]$$

where $$GARJI=\frac{\pi-2\tan^{-1}\left(\frac{GA}{2}\right)-2\tan^{-1}\left(\frac{1}{2GA}\right)}{\log_e\left[\frac{2\pi D}{(IDIV)\,xf}\sqrt{1+(GA)^2}\right]}$$

(b) Downstream Grid Points

The equations are identical to those given for aerodynamic bearings in Section 14.1.1 by Equation 14.1.

(c) Computation

The initial values assigned to the restrictor downstream pressures were calculated from the corrected line feed analysis applicable to aerostatic performance and the initial film pressures were calculated using complex potential theory.

(d) Convergence and Stability

It was found that by using relaxation techniques developed originally for the aerostatic analysis, in the hybrid computer programs numerical instabilities were experienced. The relaxation factor, used for numerical damping in the iterative technique affected the speed of convergence and numerical instability. The relaxation factor (R') is used in the computation thus:-

$$\beta_{(new)} = \{\beta_{(new)} - \beta_{(old)}\} * R' - \beta_{(old)}$$

The effect of R' on numerical instability and speed of convergence is shown diagrammatically overleaf:

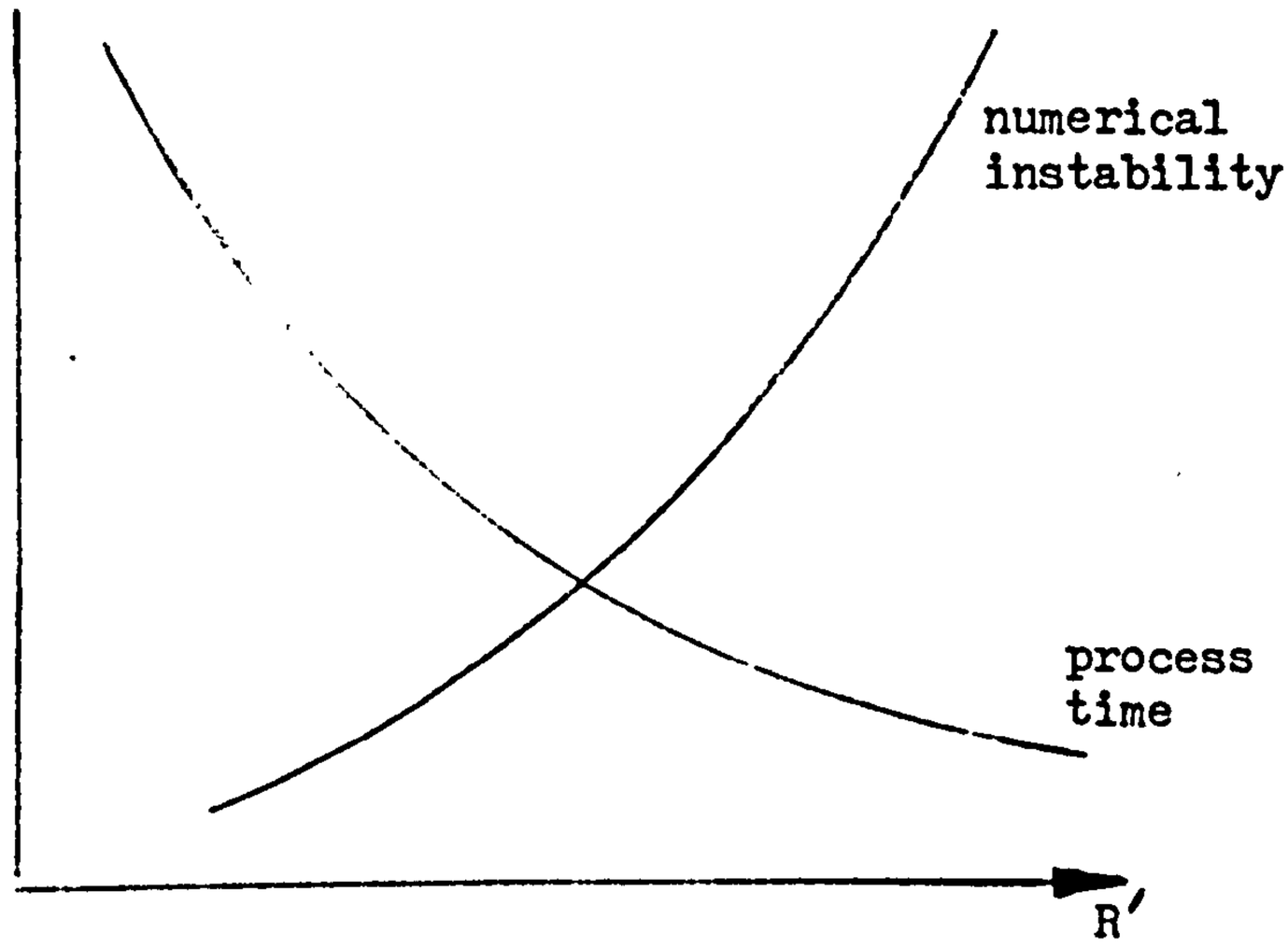

Stout (Ref. 14.2) has suggested that an over relaxation factor of R′equal to 1.1 accelerates the convergence of the film pressures. It was found that for hybrid simulations, under relaxation was necessary to prevent instabilities. The value used in the computation was R′= 0.9. Although this is not an optimum value to minimise computing time, instabilities were avoided for $\mathcal{E} \leqslant 0.8$. A more detailed analysis on the effect of relaxation techniques has been recently accomplished by Tawfik (Ref. 14.3).

(e) Reverse Flow

At high eccentricities it has been observed that the film pressure immediately below the orifice can exceed the bearing supply pressure in the low clearance side due to very high aerodynamic contributions. This implies reverse flow through the orifice from the bearing film. When this occurs it is assumed in the analysis that the inlet film pressures at these orifices are fixed at supply pressure conditions. This has the effect of predicting slightly lower load capacities than would be the case if reverse flow was

taken into account. This effect occurs only at high eccentricities (e.g. $\mathcal{E} > 0.7$ for $C_n = 2$, $L/D = 2$, $P_o/P_a = 5$) and is therefore out of range of the more typical operating conditions of $\mathcal{E} \leq 0.5$.

15. DISCUSSION OF THEORETICAL RESULTS

15.1 Introduction

In this section, the finite difference method is used to evaluate the effect of various design parameters on the hybrid bearing performance and these results are discussed.

A comparison is presented of the results from the finite difference method with those from the methods of superposition and the results presented by M.T.I.

A standard bearing is used as a reference, having the following parameters:

$$L/D = 2$$

$$a/L = 0.25$$

$$P_o/P_a = 5$$

$$\text{As } \xi = 0.7$$

$$n = 8$$

$$d/D = 0.03$$

pocketed compensation

The results presented are based on shaft displacements in-line with an orifice. For the hybrid performance, the load vector does not coincide with this orifice position. However, this basis of description has been chosen to simplify computation. The effect the orifice positions relative to the displacement has been investigated and is presented in this section.

15.2 Effect of Various Design Parameters

15.2.1 Compressibility Number C_n

Figure 15.1 illustrates the effect of C_n on load/deflection chacteristics. It can be seen that at modest values of C_n, lock-up is prevented, and that at higher values of C_n, substantial increases in load capacity are predicted. As mentioned previously, reverse flow can exist through the orifice at high eccentricities. For this condition, the orifice pressures are assumed to be at supply conditions. This is shown in Figure 15.1 by the chained lines and these results have to be viewed with some caution. However, it is noted that the eccentricity ratios where reverse flow is predicted are high compared with more typical operating eccentricities.

The aerodynamic results shown have been calculated on the assumption that the orifice planes are atmospheric boundaries.

The journal locus is shown in Figure 15.1 (b) for various C_n. It can be seen that the effect of C_n on attitude angle is entirely different for hybrid and aerodynamic modes of operation. For the hybrid mode, the effect of C_n is to generally increase attitude angle, although there is some slight overlap at high eccentricities. For the aerodynamic mode, the reverse is true - as C_n increases, attitude angle reduces.

To summarise:

for hybrid $C_n \rightarrow 0$, $\phi \rightarrow 0°$

for aerodynamic $C_n \rightarrow 0$, $\phi \rightarrow 90°$

15.2.2 Length to Diameter Ratio L/D

Figure 15.2 illustrates the effect of varying L/D with C_n fixed. As L/D reduces, the effect on load capacity for a given ε reduces. For L/D = 1, very high values of C_n are required to generate a significant hybrid effect at the supply pressure shown. In the case of L/D = 0.5, hybrid effects are virtually non-existent for eccentricity ratio $\varepsilon < 0.8$, $C_n < 6$.

15.2.3 Supply Pressure Ratio P_o/P_a

Figure 15.3 illustrates the effects of varying P_o/P_a. At low supply pressures, although the aerostatic load is reduced, the effect of speed on load carrying capacity becomes more pronounced. At high supply pressures, the reverse applies.

15.2.4 Land Width Ratio a/L

The effect of the number of feeding planes on load capacity is shown in Figure 15.4. For aerostatic conditions, the load capacity for the single plane admission bearing is approximately 0.7 that of the double plane admission bearing. The aerodynamic contribution however for the single plane bearing is greater than that for the double plane bearing. This characteristic is also predicted by the method proposed for calculating the aerodynamic loads in the modified superposition method. As C_n increases, the load capacities approach a similar value. The lower aerostatic load of the single plane bearing is offset almost entirely by the extra aerodynamic contribution.

15.2.5 Feeding Parameter $\Lambda_s \xi$

The effect of $\Lambda_s \xi$ on hybrid performance is shown in Figure 15.5. For aerostatic conditions, the load capacities are very dissimilar for a wide range of $\Lambda_s \xi$ values. As C_n and ε increases, the load capacities approach the highest load capacity curve given by $\Lambda_s \xi = 0.7$.

15.2.6 Type of Compensation

Figure 15.6 compares the load capacities of bearings having pocketed orifices with those having inherently compensated orifices. At hybrid conditions, the aerodynamic component of the inherently compensated bearing is greater than that for the pocketed bearing. This offsets to some extent the lower aerostatic load capacity which inherently compensated bearings exhibit. The combined effects tend to minimise the difference in performance when operating at speed.

A comparison between orifice compensated and slot fed bearings are shown in Figure 15.7. The computer program for the slot bearing has been developed independently at Leicester Polytechnic by Tawfik (Ref. 14.3). It can be seen that the two bearings give similar load capacities for both aerostatic and hybrid performance (to within 8%).

15.2.7 Orifice Position and Displacement

As mentioned in the Introduction to this section, the results shown are based on shaft displacements in-line with an orifice. This approach has been adopted in order to facilitate computation. It is realised however, that this is a somewhat theoretical condition as in practice bearing orientation and applied loads (i.e. neglecting out-of-balance loads) are fixed relative to one another. This implies that as speed increases, the attitude angle

varies as shown below:

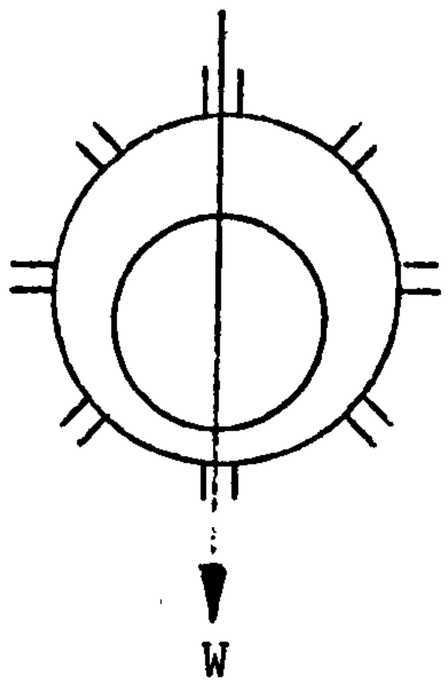

zero speed

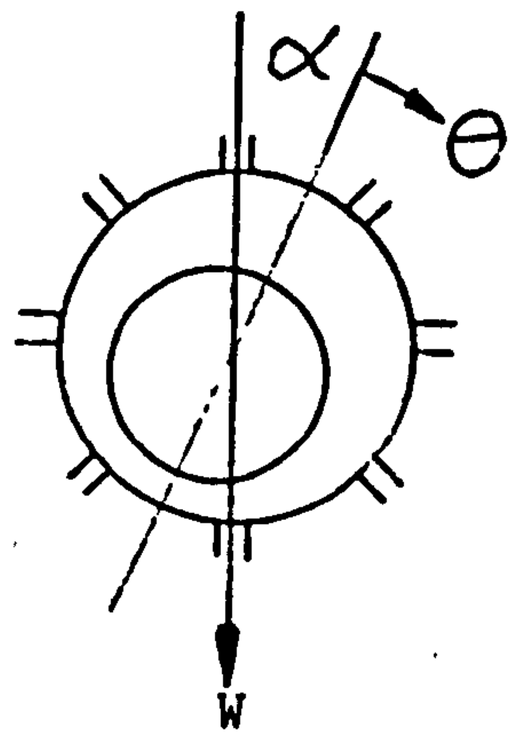

at speed

The effect of the orifice positions relative to the displacement has been computed. The only change necessary is to modify the local clearances thus:

$$h = h_0 \{ 1 + \varepsilon [\cos(\theta + \alpha)] \}$$

where α is the angle between the line of minimum/maximum clearance and the position of the centreline of an orifice

The results are shown in Figure 15.8 for aerostatic and hybrid performance For the aerostatic performance, the results correlate to within 6% for $\varepsilon \leq 0.8$. This compares favourably to experimental data obtained by Grewal (Ref. 7.16), who found the reduction to be of the order of 4%, and with data obtained by the Author (Ref. 2.2) of 7%.

The hybrid performance is also only marginally affected by orifice orientation.

15.3 Typical Pressure Profiles

Figure 15.9 shows typical pressure profiles from the finite difference solution. In this case, the computer program was run with initially $\alpha = 0$ and the attitude angle calculated. The computer program was then re-run, but this time with $\alpha = \emptyset$. In doing so, the resultant load line corresponded to the position of an orifice centreline. It can be seen that the aerodynamic effect on the aerostatic pressure profile is to reduce film pressures in the high clearance side and to increase them in the low clearance side. The pressures at the centre plane in the low clearance side are shown to be greater than supply conditions, although reverse flow through the orifice is not predicted for this case.

Figure 15.9(b) shows the circumferential pressure profiles in the plane of the orifices. A feature which is of note is the shape of pressure gradients around the orifice under the applied load. In the direction of rotation towards the line of minimum/maximum film clearance the pressure gradient is positive. This implies that flow does not occur in that direction due to the wedge effect in the converging clearance.

15.4 Comparison Between Finite Difference Solution and Other Analyses

15.4.1 Powell's Method of Superposition

A comparison of the results from the finite difference solution with the results from the method of superposition proposed by Powell (Refs. 7.4 and 7.5) as outlined in Section 14.2.1 is presented in Figures 15.10(a)→15.10(g). To evaluate the superposition method, the finite difference technique has been applied to calculate both the aerostatic and aerodynamic load components.

These components are used in Powell's superposition method to deduce the hybrid load capacity thus:

$$\overrightarrow{W} = \overrightarrow{W_S + k' W_A}$$

The value of k′ which gives the same load capacity as that given by the hybrid finite difference solution is tabulated below. Throughout d /D = 0.03 and n = 8 and unless otherwise stated in the table:

$C_n = 2$

$L/D = 2$

$a/L = 0.25$

$P_o/P_a = 5$

pocketed compensated orifices

The table has been compiled in this way to highlight those parameters which change.

Figure No.	C_n	L/D	a/L	P_o/P_a	compens'n	k′	
						ε=0.5	ε=0.7
15.10(a)						0.40	0.48
15.10(b)	6					0.44	0.53
15.10(c)		1				0.20	0.24
15.10(d)			0.5			0.74	0.80
15.10(e)				2		0.50	0.60
15.10(f)				8		0.25	0.45
15.10(g)					IC	0.49	0.59

IC - inherently compensated orifices

It can be seen that the value of k' increases with the following variations:

ε	increasing
C_n	increasing
L/D	increasing
a/L	increasing
P_o/P_a	decreasing

This is to be expected as all these changes increase the aerodynamic effects. The most significant parameters which affect k' are L/D, a/L and P_o/P_a.

The values of k' obtained for the case of L/D = 2, a/L = 0.5 [Figure 15.10(d)] compares well to that obtained by Powell from experimental results. In Reference 7.4 Powell suggests $k' = 0.74$ and in Reference 7.5 suggests $k' = 0.70$. This compares with $k' = 0.74$ and 0.80 tabulated for $\varepsilon = 0.5$ and $\varepsilon = 0.8$ respectively.

For L/D = 1 or a/L = 0.25, the value of k' indicated in the table for $\varepsilon = 0.5$ reduces to 0.20 and 0.40 respectively.

15.4.2 M.T.I.

M.T.I. (Ref. 2.11) give design data applicable only to single entry bearings, a/L = 0.5. A comparison of the results from the finite difference solution with those from the M.T.I. design charts is shown in Figure 15.11. The ratio of the load capacities from the M.T.I. design charts to that obtained by the finite difference solution is shown below for $\varepsilon = 0.5$:

aerostatic	: 1.07
hybrid ($C_n = 2$)	: 1.10

15.4.3 Modified Superposition

The modified superposition method has been outlined in Section 14.2.2. This differs from Powell's method in the calculation of the aerodynamic component for hybrid performance. A comparison of the results from the finite difference solution with the results from the modified superposition method are shown in Figures 15.12 (a)→15.12 (e). For the superposition method, the finite difference analysis has been used for the calculation of both the aerostatic load and the aerodynamic load components.

The ratio of the load capacity from the modified superposition method to that obtained by the finite difference solution is tabulated below.

Throughout d /D = 0.03 and n = 8 and unless otherwise specified in the table below:

$$C_n = 2$$

$$L/D = 2$$

$$a/L = 0.25$$

$$P_o/P_a = 5$$

pocketed compensated orifices

Figure No.	C_n	L/D	a/L	P_o/P_a	compens'n	Load Ratio	
						ε=0.5	ε=0.7
15.12(a)	1					0.97	0.93
15.12(a)	2					0.94	0.91
15.12(a)	6					0.91	-
15.12(b)		1				0.98	0.97
15.12(c)			0.5			0.85	0.85
15.12(d)				2		0.85	0.83
15.12(d)				8		0.97	0.94
15.12(e)					inherently	0.86	0.81

It can be seem that the results from the modified superposition method in all cases are lower than that obtained from the finite difference analysis, and are within 15% of the finite difference predictions up to $\varepsilon \leqslant 0.5$.

15.5 Conclusions

The finite difference analysis has been used to determine the effects of various design parameters on the hybrid characteristics. It has been shown that in addition to the compressibility number, supply pressure ratio and L/D ratio, the land width ratio has a significant effect on the aerodynamic contribution to the hybrid performance. This characteristic was not apparent from the current literature, and indicates that the superposition method of calculating the aerodynamic contribution is related to the a/L ratio. The feeding parameter and the type of compensation, although influencing the aerostatic load, has only a marginal effect on the hybrid performance.

Reverse flow through the orifices in the low clearance side of the bearing is predicted for high eccentricities. The computer program does not take this effect into account but assumes that under these conditions, the downstream film pressure at these orifices is at supply pressure. It has been shown that the eccentricity ratios where reverse flow is predicted are high ($\varepsilon > 0.7$) for typical hybrid bearings compared with normal running eccentricities. ($\varepsilon \leqslant 0.5$).

A comparison has been made between the results from the finite difference solution with other theoretical models. For the method proposed by Powell, an empirical factor k′has been suggested in Reference 7.5 of 0.70 for L/D = 2, a/L = 0.5. This compares well with that obtained by comparing this method with the results from the finite difference solution where k′was found to be 0.74 for $\varepsilon = 0.5$. For L/D equal to unity, or with a/L = 0.5

comparison between the two theoretical models indicates a much lower value of $k'(0.20 - 0.40)$ is more appropriate.

The results from the M.T.I. method has been shown to correlate with the results from the finite difference solution to within 10% for both aerostatic and hybrid conditions.

The modified superposition method has also been examined. This method has been presented in the previous section and follows closely that proposed by Powell, but differs in the manner in which the aerodynamic component is calculated. It has been shown that the predictions from this method are within 15% of those obtained from the finite difference analysis for a wide range of L/D, supply pressure ratios and a/L values.

16. EXPERIMENTAL STUDY

16.1 Aim and Scope of this Work

The aim of the experimental effort was to obtain for varying bearing configurations the load/deflection characteristics and attitude angle/journal locus for differing C_n values. The bearing configurations tested include plain cylindrical aerodynamic and orifice compensated (pocketed) journal bearings.

It was realised that the presence of the holes in the bearing affects the aerodynamic performance. For this reason, the aerodynamic bearings were manufactured initially with inserts present and subsequent tests with them removed and replaced with orifices provides quantitive data from which the influence of the holes on the aerodynamic performance can be determined.

16.2 Selection of Experimental Variables

The experimental values of the test bearings are given below:

* 1. $L/D = 1$; $h_o = 12.3\ \mu m$

* 2. $L/D = 2$; $h_o = 12.7\ \mu m$

3. $L/D = 2$; $h_o = 17.9\ \mu m$

* initially fitted with inserts in place of orifice

All bearings were manufactured to $a/L = 0.25$, with a nominal diameter of 50 mm. The orifice geometry was common to all bearings. Watch-makers jewels were press-fitted into a pocket to provide pocketed orifice compensation.

The orifice geometry is listed below:

$n = 8$

$d_o = 0.09$ mm

$d_R = 1.80$ mm

$b = 0.10$ mm

16.3 Test Rig Design

The test rig arrangement is shown schematically in Figure 16.1, and a photograph of the rig is shown in Plates 1 and 2.

The test shaft (1) and close fitting sleeves (2) were supported in hydrostatic slave bearings (3). These bearings were of the recessed type having combined journal and thrust faces. The test bearing (4), positioned between the slave bearings was loaded upwards by a pneumatic load cylinder (5) which housed a piston supported by an aerostatic journal bearing to minimise friction. The loading mechanism (6) provided adjustment in order that the test bearing could be loaded to give parallel motion in the bearing clearance.

The load cylinder pressure wss monitored by a pressure transducer (7). Adjusting the pressure in the load cylinder by a pressure regulator enabled the load to be applied to the test bearing with relative ease and in a continuously variable manner. Wayne Kerr capacitance probes (8) were mounted at both ends of the test bearing to monitor bearing deflections. Two probes were mounted in line with the load as shown in Figure 16.1 to record vertical movement and two other probes mounted orthogonal to the load line to record horizontal deflections. Their signals were fed into a purpose-built analogue computer which calculated the resultant deflection e_{res} and attitude angle ϕ as shown in Figure 13.1. Bearing supply pressure was monitored by a pressure transducer.

The test shaft was driven by an electric motor via a belt and pulley (9) and its speed was monitored by a tacho generator.

Provision was made for displaying bearing supply pressure, bearing load, shaft speed, e_x , e_y , e_{res} and ϕ in a digital form.

The test bearing was restrained to prevent axial movement or rotation without influencing the radial loading shown in Figure 16.2.

16.4 Instrumentation

The instrumentation of the test rig was required to measure the following parameters.

1. Bearing load
2. Bearing deflections and journal locus
3. Bearing supply pressure
4. Bearing flow rate
5. Rotational speed of the shaft

The test rig instrumentation used is shown in Figure 16.3 and a photograph of the instrumentation panel is shown in Plate 3.

16.4.1 Bearing Load

The pressure transducer used to monitor the air pressure in the pneumatic load cell was a Bell and Howell, type 4-326-L101. This was used in conjunction with a transducer amplifier, type 91D, supplied by Strainstall.

The diameter of the load piston housed in the load cylinder was 46.94 mm. The applied load is a product of the pressure X area, which gives:

$$W \equiv 173 \text{ Newtons/bar}$$

(at 7 bars, $W \equiv 1211$ Newtons)

The system was calibrated using a dead weight tester as supplied by Barnet Instrumentation Ltd. The gain of the transducer amplifier was adjusted to give 1.211 volts at 7 bars. In doing so, output voltage gave:

$$1 \text{ m V} \equiv 1 \text{ Newton}$$

The calibration curve is given in Figure 16. 4. The non-linearity from zero to 7 bars was found to be within ± 2 mV. This corresponds to ± 2 Newtons or approximately ± 0.1% .

16.4.2 Bearing Deflections

Bearing deflections were monitored by four capacitance probes, type MB1 as supplied by Wayne Kerr, and a Wayne Kerr meter type TE600B. This gave a range of measurement of 127 μm for all four probes simultaneously. The probes were mounted in the bearing sleeves as shown below:

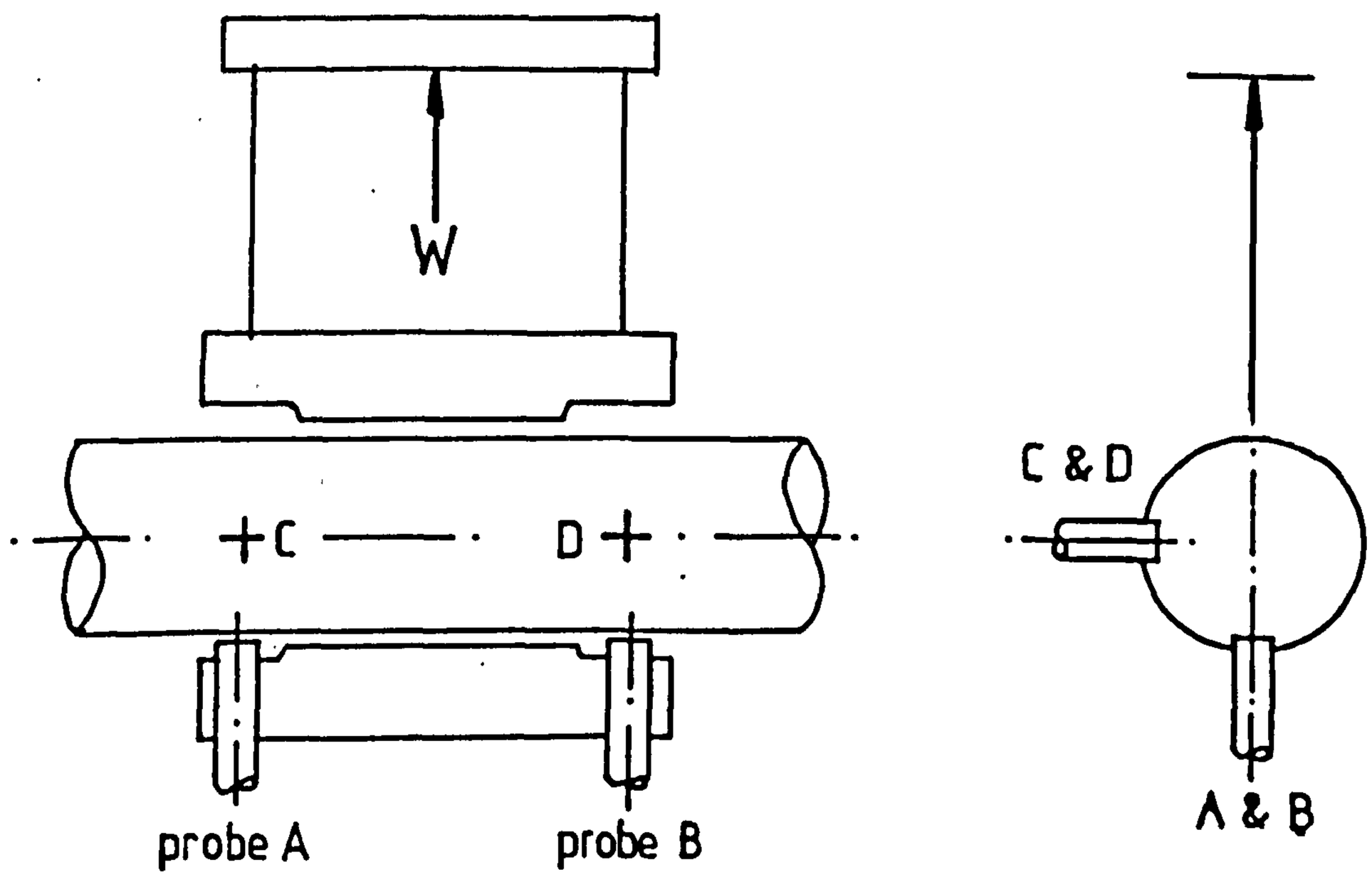

A calibration fixture was used to calibrate the probes, as shown diagrammatically overleaf:

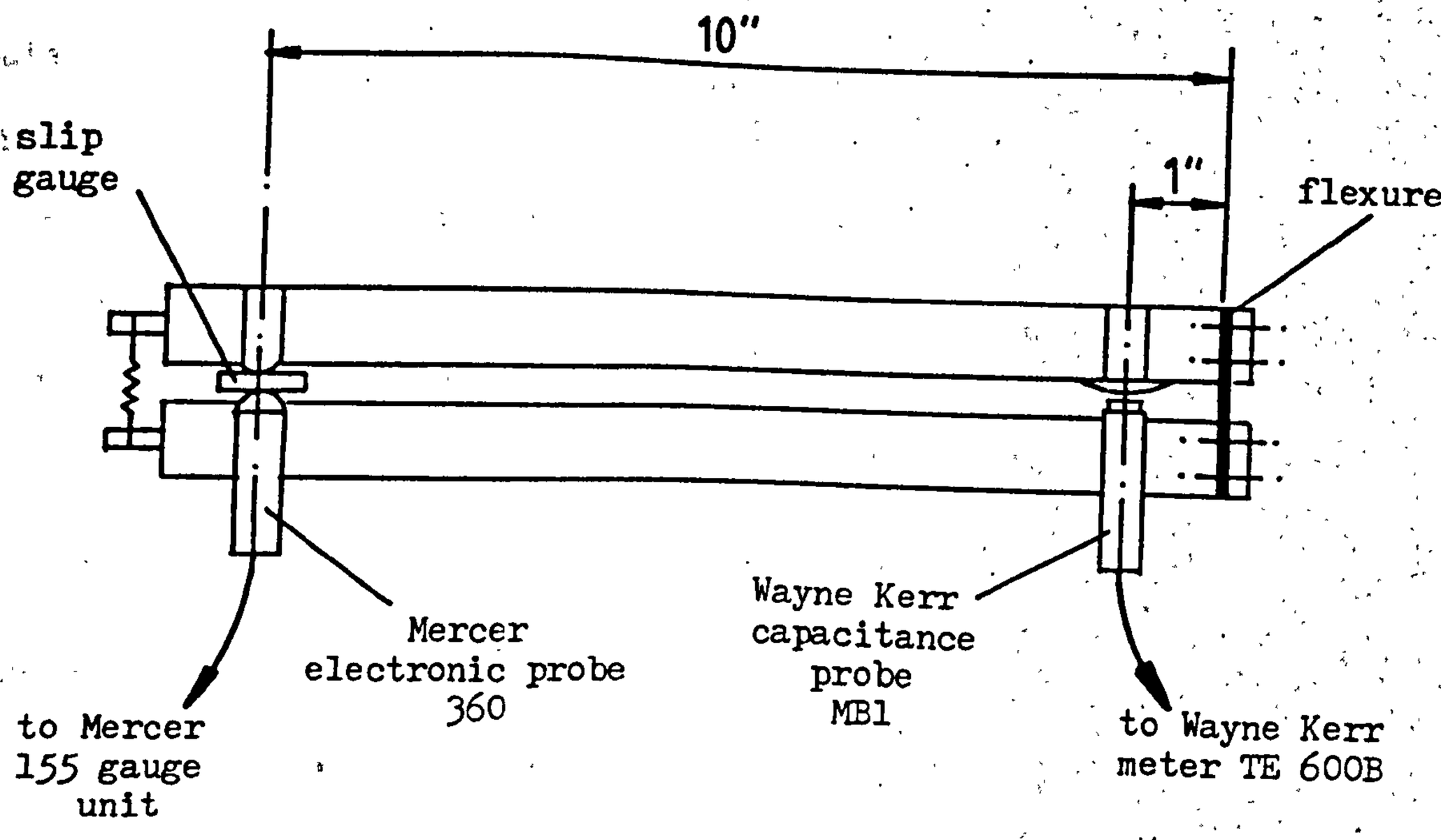

A photograph of the calibration fixture is shown in Plate 4. The face of the insert from which the probe was calibrated incorporated a curved surface - the radius of which corresponded to the radius of the test shaft.

A typical calibration curve for the output from a Wayne Kerr amplifier is shown in Figure 16.5, and gives a calibration of: 1 mV $\equiv$ 0.118 μm. The non-linearity was found to be within $\pm$ 4 mV for deflections of 12 μm $\rightarrow$ 81 μm. This corresponds to $\pm$ 0.5 μm.

16.4.3 Analogue Computer for Calculation of Shaft Locus

The signals from the Wayne Kerr meter circuits A+B, C+D were fed into a purpose-built analogue computer which calculated the resultant deflection e_{res} and attitude angle ϕ thus:

$$e_{res} = \sqrt{e_x^2 + e_y^2}$$

$$\phi = \tan^{-1}\left[\frac{e_y}{e_x}\right]$$

where e_x is the deflection in the vertical plane measured by circuit A+B

e_y " horizontal " C+D

The computational circuit exploits the characteristics of operational amplifiers with semi-conductors in their feed back circuits. This circuit produces an output dependent on the logarithm of the input. Any mathematical expression can be built electronically using this principle. Further reference to this method is given by Graeme in Reference 16.1.

The circuit diagrams used are shown in Figure 16.6. Figure 16.6 (a) refers to the $\sqrt{X^2+Y^2}$ circuit and operates by initially multiplying the input signals to give a convenient calibration of:

$$X', Y' \; ; \quad 1 \text{ mV} \equiv 0.025 \; \mu\text{m}$$

A facility has also been incorporated to zero an input signal without affecting the calibration, achieved by potentiometers. This has been done in order that the condition of bearing zero eccentricity can be used as a zero datum. This is also necessary in any case for the subsequent $\sqrt{X^2+Y^2}$ and $\tan^{-1}$ circuits.

The output from X' is shown in Figure 16.5. This gives 1 mV $\equiv$ 0.025 μm with a non-linearity error of within $\pm$ 0.2 μm or $\pm$ 8 mV for probe deflections of 12 μm $\rightarrow$ 81 μm.

After the X' and Y' circuits the modulus of the signals are found. This has the effect of converting the signals to positive values: positive to positive, negative to positive, given by /X'/, /Y'/. These signals are then converted to logarithmic form, their logs doubled, added together and anti-logged. As shown in Figure 16.6 the reader can see that many additional sub-circuits were added. Some of these circuits were added to eliminate instabilities and others added to improve the accuracy.

The output from the $\sqrt{X^2+Y^2}$ circuit is shown in Figure 16.7(a).

This has been drawn directly onto an X-Y plotter. The errors have been found to be within ± 0.5% for a wide range of values of X' and Y'. Compounded with non-linearity errors for the X' and Y' circuits gives a total error in reading of within ± 13 mV or ± 0.3 μm for probe deflections of 12 μm → 81 μm.

The $\tan^{-1}$ circuit follows closely that suggested by Graeme in Reference 161. It is an iterative circuit, with finite difference methods employed electronically. The technique is to approximate the tan function thus:

$$\tan(Z) \simeq \frac{Z^{1.21}}{1 + Z^{1.21}}$$

The difference between the output and the tan (Z) circuit is used to calculate an error in Z, which is added to the old value and so on. The circuit has been modified to give a convenient output thus:

$$1\text{mV} \equiv 0.1^{\circ}$$

The output from the $\tan^{-1}$ circuit is shown in Figure 16.7(b). This has been drawn directly onto an X-Y plotter. For a wide range of values of X' and Y', the error has been found to be within ± 0.8° or 8 mV.

16.4.4 Rotational Speed

The shaft speed was monitored by a tacho-generator (Evershed and Vignoles type FBF 102A) giving a nominal output of 24V per 1000r.p.m. This was used so that the analogue signal could be fed directly into one of the axis of an X-Y plotter. This cannot be achieved using a computing counter as the output is in a digital form.

The system was calibrated using the set up shown in Figure 16.8. A magnetic pick-up (Orbit Controls type 70D-1101) sensed the flux changes of a gear wheel connected to the drive motor output shaft. A Racal 9525 frequency meter was used to record motor speed. The electric motor was run to 2341 rp.m. as indicated by the frequency counter.

The pulleys and belting to the test shaft had a ratio of motor/shaft speed of 26/60. The motor speed for 2314 r.p.m. corresponds to a test shaft speed of 5340 r.p.m. The 10kΩ potentiometer across the output terminals of the tacho-generator was adjusted to give an output of 5.340V. Thus 1mV from the output of the potentiometer corresponds to a shaft speed of 1 r.p.m. The non-linearity errors were found to be within ± 5mV or ± 5r.p.m.

16.4.5 Bearing Supply Pressure

A pressure transducer was used to adjust and monitor the bearing supply pressure. The transducer was a Bell and Howell type 4-326-L101 and was used in conjunction with a Strainstall transducer amplifier type 91D. The system was calibrated using a dead weight tester as supplied by Barnet Instruments Ltd. Non-linearity from zero to 7 bars was found to be within ± 0.1%.

16.5 Air Supply Circuit

The test rig air supply circuit is shown diagrammatically in Figure 16.9. The air supply to the test rig was initially filtered using 5 μm elements. The air supply to the test bearing and to the pneumatic load cell was further filtered by 2 μm elements downstream of which pressure regulators were used to adjust the test bearing pressure, pneumatic load cell pressure and piston bearing pressure.

The air flow to the test bearing was measured using a 'Gapmeter Lab-Kit'

as supplied by G.A. Platon Ltd. The appropriate tube/float combination was used so that large scale readings were obtained.

16.6 Oil Supply Circuit

Figure 16.10 shows the oil supply circuit used for the hydrostatic slave bearings. The oil pump used was as follows:

Keelavite Power Pack

Electric motor	:	7.5 kW
Flow at 100 bar	:	30 litre/min
Tank capacity	:	140 litres
Oil used	:	Light HT32, 24Cp

As shown, the manifold distributes the oil supply to the diaphragm valves. These valves were used to control the fluid pressure to the 4 recesses in each of the slave bearings.

Details of the diaphragm valves are shown in Figure 16.11. The valves were originally designed to incorporate a thin diaphragm to improve bearing stiffness. However, as the applied loads to these bearings were low, the thickness of the diaphragm used was large so that the valves operated as rigid viscous restrictors. A photograph of a diaphragm valve used is shown in Plate 5.

16.7 Slave Bearings

The hydrostatic slave bearings were designed to give minimum total power dissipation following the design procedure given by Stout and Rowe (Ref. 16.2).

The bearing geometry was as follows:

4 - recessed bearing

$a/L = 0.25$

$\theta = 30$

$D_i = 40$ mm nominal

$D_o = 60$ mm "

$L = 50$ mm "

h_o (radial) = 70 → 95 μm

h_o (axial) = 70 → 95 μm

supply pressure = 30 Bars

A photograph of a slave bearing is shown in Plate 6.

16.8 Test Bearings

A typical design of a test bearing is shown in Figure 16.12. The material chosen was lead bronze LB9 due its good anti-seizure properties and because the coefficient of linear expansion of this material is similar to that of the material used for the test shaft, and is specified below:

Lead Bronze LB9 : 18.0×10^{-6} mm/°C mm

Stainless Steel EN58BM : 16.8×10^{-6} mm/°C mm

A photograph of the test bearings are shown in Plate 7.

16.8.1 Manufacture

The aerodynamic bearings (1) and (2) were turned and the holes which were to be subsequently used for mounting the orifices , were drilled to a diameter of 1.70 mm. Brass plugs, which were slightly tapered, were press-fitted into the holes from the bore as shown overleaf :

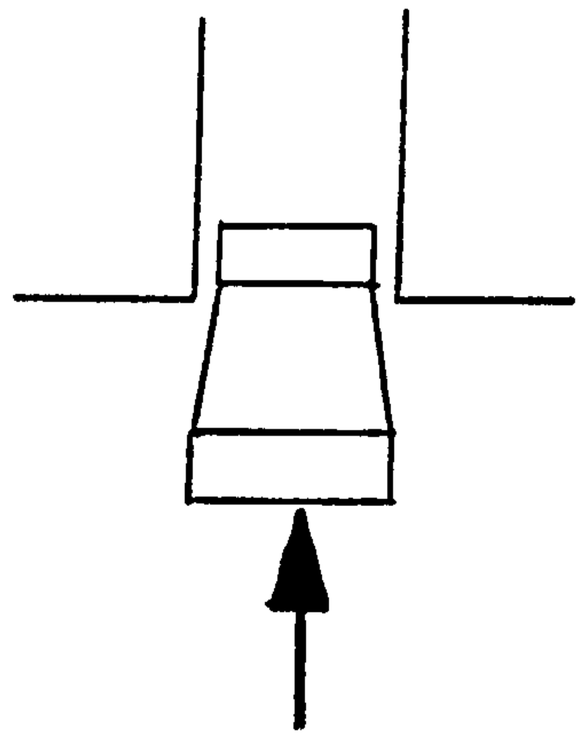

The hybrid bearing (3) was turned and the holes for the orifices were drilled and reamed and the jewels mounted prior to grinding. Sufficient allowance was made in the pocket depth for grinding.

The bores were ground and finished lapped to improve their geometry and to achieve finished size. For this purpose, cast iron helical laps were used as supplied by Engis Ltd. Proir to lapping, the laps were themselves lapped to eliminate their geometric inaccuracies. The lapping compound used was A03 (850 grid size) as supplied by English Abrasives Ltd. A photograph of the lapping equipment used is shown in Plate 8.

After the aerodynamic tests were completed on the plain cylindrical bearings their inserts were removed, the holes reamed to 1.80 mm and the jewels mounted. In doing so, the same bearing could be operated aerodynamically to determine the effect of the presence of the holes on the performance characteristics. As the bearings would have identical clearances, meaningful conclusions can be drawn as to their comparative performance.

The holes were drilled prior to grinding so that the bore would not be subjected to radial drilling after it was machined to finished size.

It was thought that this could deform the wall of the bearing and therefore this effect was prevented.

16.8.2 Mounting Jewels in Pockets

Figure 16.13 shows the procedure adopted for mounting the jewels in the pockets to the required depth. It was found that if the jewel O/D and reamed hole diameter gave an interference fit that was excessive, the jewel would either crack or smash. The former case could easily be observed by a microscope.

16.8.3 Metrology

The technique used to measure the bore profiles were similar to that employed in a previous study undertaken by the Author reported in Reference 2.2.

(a) Air Gauge Measurements

The bore diameters were measured by air gauging equipment as supplied by Thomas Mercer Ltd. The equipment consisted of a 2-Jet Nitralloy air plug gauge, setting masters and a 155 electronic unit. The range of diameter measurements afforded by the equipment was 50.0130-50.043 mm with the display readable to 0.1 μm. The accuracy of the setting masters as quoted by a Certificate of Calibration was within ± 1.0 μm. A photograph of the equipment used is shown in Plate 9.

The bores were measured after allowing the bearings, setting masters and the plug gauge to stand overnight in a controlled temperature environment of 20°C. The bearing and setting masters were handled during measurement with thick cotton gloves to ensure that a minimum of hand heat was transferred.

The parallelism of the bores after lapping was found to be within the range of 0.7-1.5 μm. This figure refers to the deviation in size, as measured in two orthogonal planes, along a span between two axial planes which were 5 mm inside the bore from the ends of the bearing. The ovality was found to be less than 1.0 μm.

(b) Talyrond Measurements

The air gauging equipment used only provided measurements of absolute size, parallelism and ovality. A Talyrond 200 with a straightness attachment was used to obtain the complete geometric form, i.e. roundness, straightness and parallelism. From these readings, a measure of cylindricity was obtained. This is defined as the radial difference between two concentric cylinders which encompass the complete bore profile. Also, errors in parallelism obtained from the Talyrond 200 can be compared with the air gauge readings.

The results for the L/D = 1 bearing used initially for aerodynamic tests are presented. Figure 16.14 shows the roundness traces at differing axial planes (at both ends of the bearing and at the centre plane). Figure 16.15 shows axial profile traces of the bore obtained for two orthogonal planes, from which parallelism and straightness have been deduced.

All the test bearings were manufactured in the same manner. It was confirmed that form errors for the bearing shown was typical for all the test bearings.

Roundness

The roundness achieved was of the order of 0.4 μm MSC. From the roundness traces, it can be seen that out-of-roundness took the form of a two lobed shape, i.e. oval. This was also confirmed by the fact that the ovality as measured by the air plug gauge compared well with the out-of-roundness deduced from the Talyrond traces.

Parallelism

The table below compares the parallelism deduced from the air gauge readings with that obtained from the Talyrond traces. The values given correspond to the deviation in the diameter along the bearing length compared to the diameter measured mid-way along the bearing length.

Distance along bearing from 'Top' mm	Deviation in Diameter μm			
	Plane A		Plane B	
	Talyrond	Air Gauge	Talyrond	Air Gauge
5	+ 1.5	+ 1.3	+ 1.0	+ 1.5
9	+ 0.3	+ 0.5	+ 0.1	+ 0.5
13	0	+ 0.1	- 0.1	+ 0.3
17	- 0.1	+ 0.3	- 0.1	+ 0.1
21	- 0.1	0	- 0.3	+ 0.1
25	0	0	0	0
29	+ 0.4	+ 0.5	+ 0.6	+ 0.6
33	+ 0.6	+ 0.7	+ 0.6	+ 0.8
37	+ 0.3	+ 0.4	+ 0.6	+ 0.5
41	+ 0.4	+ 0.2	+ 0.4	+ 0.4
45	+ 0.8	+ 0.5	+ 1.0	+ 0.8

It can be seen that good agreement exists between the parallelism errors as deduced by the Talyrond and air gauge equipment. The discrepancies between the two sets of results can be accounted for by temperature effects and drift which results in non-repeatability of the readings of the order of $\pm$ 0.3 μm.

Both sets of results indicate that the bore is slightly bell mouthed. At a distance of 5 mm in from each end, the bore diameters are approximately 1-1.5 μm larger in size than the mid-plane diameters whilst at a distance of 10 mm in from the ends, the bore diameters are approximately 0.5 μm larger.

Straightness

The straightness of the bore between the central 40 mm length has been deduced from the axial profile traces by plotting the deviation of the mean geometric axis with respect to the surface profiles. This has been found to be:

Plane A : 0.25 um

Plane B : 0.22 um

Cylindricity

The cylindricity over the central 32 mm is composed of:

Parallelism and straightness : 0.65 μm maximum variation in radius

" roundness : 0.45 μm MZC maximum

As the roundness has been shown to be of a consistent form along the bore length, the cylindricity is obtained by summing the two errors above to give a cylindricity of 1.1 μm.

Absolute Size

The diameters attributed to the bearings were an average value of the air gauge readings measured along the bearing lengths. These are given below:

1. L/D = 1 : 50.0234 mm
2. L/D = 1 : 50.0242 mm
3. L/D = 2 : 50.0346 mm

16.9 Test Shaft

The test shaft assembly is shown in Figure 16.16. The material chosen was EN58BM due to its good anti-corrosion properties.

The main body of the test shaft (1) consists of a step at each end. Onto these diameters, close fitting sleeves (2) butt up to each face by tightening the nuts (5). To the outward faces of (2) are bolted rings (3) which provide the axial thrust faces. The distance between these faces can be adjusted by the spacer (4).

The design overcomes the problem of producing a right-angle corner for the combined journal and thrust faces. This problem would have occurred if one component was used rather than the two components (2) and (3). Also, the design allows for axial adjustment between the thrust faces.

A slip ring assembly was used in order to earth the shaft. This was necessary for the Wayne Kerr capacitance probes for the measurement of shaft deflections. A photograph of the test shaft is shown in Plate 10.

16.9.1 Manufacture

To ensure dimensional stability and the squareness of faces, the following manufacturing and heat treatment sequence was adopted:

1. Initial stress relieve at 500° C, air cool
2. Face and centre both ends and skin
3. Turn all diameters to + 0.25 mm
4. Stress relieve at 500° C, air cool
5. Grind steps and shoulders
6. Fit sleeves (2)
7. Grind bearing diameters 40 mm and 50 mm nominal and grind outward faces on conponent (2)
8. Dismantle and finish lap 50 mm diameter
9. Assemble and fit sleeves (3) and spacer (4)

The rings (8) and the spacer (4) were ground on a surface grinder to ensure their faces were parallel.

The test shaft was lapped to improve geometric form and to achieve finished size. Cast iron helical laps as supplied by Engis Ltd. were used, in conjunction with lapping compound A03 (850 grid size). A photograph of the lapping equipment is shown in Plate 8.

16.9.2 Metrology

The shaft diameter was measured by air gauging equipment as supplied by Thomas Mercer Ltd. The equipment consisted of a 2-Jet Nitralloy air ring gauge, setting masters and a 155 electronic unit. The range of diameter measurements afforded by the equipment was 49.978 - 50.008 mm with the display readable to 0.1 μm. The accuracy of the setting masters as quoted by a Certificate of Calibration was within ± 1.0 μm. A photograph of the equipment used is shown in Plate 9.

The table overleaf gives the parallelism deduced from the air gauge readings. The values given correspond to the deviation in the diameter along the shaft compared to the diameter measured mid-way.

Distance from one end mm	Deviation in Diameter μm	
	Plane A	Plane B
15	+ 0.9	+ 0.1
30	+ 0.6	+ 0.1
45	+ 0.1	- 0.1
60	- 0.1	- 0.1
75	0	0
90	0	0
105	+ 0.4	+ 0.1
120	+ 0.4	0
135	- 0.1	- 0.7
150	+ 0.5	- 0.7
165	+ 1.0	+ 0.5

Over the central 120 mm, the shaft diameter is parallel to within 1.0 μm and the ovality was found to be within 1.2 μm. The averaged size over the central 120 mm was found to be 49.9988 mm.

16.10 Determination of $\varepsilon = 0$

16.10.1 Cancelling Applied Loads

The applied load to counter-balance the weight of the test bearing, load piston, etc. was determined by the following procedure:

Hybrid Bearings

(a) Counter-balance the weight of the bearing by the application of appropriate pneumatic load cell pressure

(b) Set bearing supply pressure to 5 bar gauge

(c) Note capacitance probe readings (A+B)

(d) Reduce bearing supply pressure to 1 bar gauge

(e) Note capacitance probe readings (A+B)

(f) Adjust cylinder load pressure such that readings (e) equal to (c)

(g) Repeat (b) - (f) until readings (e) and (c) are equal

A final applied load was obtained for which a change of supply pressure gave no change in capacitance probe readings.

Aerodynamic Bearings

(a) Counter-balance the weight of the bearing by the application of appropriate pneumatic load cell pressure

(b) Set shaft speed to 5000 r.p.m.

(c) Note capacitance probe readings (A+B)

(d) Reduce shaft speed to 2000 r.p.m.

(e) Note capacitance probe readings (A+B)

(f) Adjust cylinder load pressure such that readings (e) equal to (c)

(g) Repeat (b) - (f) until readings (e) and (c) are equal

A final applied load was obtained for which a change of speed gave no change in capacitance probe readings.

16.10.2 Cancelling Applied Torques

A torque was applied to the test bearing to cancel the influence of the capacitance probe leads, and for hybrid bearings, the bearing air supply tube. It was assumed that this torque was constant for all supply pressures and bearing eccentricities. This applied torque was initially cancelled in the vertical plane by the following procedure:

Hybrid Bearings

(a) Apply counter balance load

(b) Switch display on Wayne Kerr to (A-B)

(c) Set bearing supply pressure to 5 bar gauge

(d) Note capacitance probe readings (A-B)

(e) Reduce bearing pressure to 1 bar gauge

(f) Note capacitance probe readings (A-B)

(g) Add weights to one side of the load adjusting mechanism such that readings (f) equal to (d)

(h) Repeat (c) - (g) until readings (f) and (d) equal

Aerodynamic Bearings

(a) Apply counter balance load

(b) Switch display on Wayne Kerr to (A-B)

(c) Set shaft speed to 5000 r.p.m.

(d) Note capacitance probe readings (A-B)

(e) Reduce shaft speed to 2000 r.p.m.

(f) Note capacitance probe readings (A-B)

(g) Add weights to one side of the load adjusting mechanism such that readings (f) equal to (d)

(h) Repeat (c) - (g) until readings (f) and (d) equal

For obtaining parallel motion in the film clearance during loading, the load adjusting mechanism was adjusted so that readings A-B were equal from $\varepsilon = 0.5$.

The condition of $\varepsilon = 0$ as used in this investigation is defined as folows:

Hybrid Bearings

The condition at which a change in supply pressure from 1 to 5 bars resulted in a deflection less than 0.8 μm either radial or as a tilt.

Aerodynamic Bearings

The condition at which a change in shaft speed from 2000 - 5000 r.p.m. resulted on a deflection less than 0.8 μm either radial or as a tilt.

16.11 Data Acquisition

The results obtained were in the form of curves produced on an X-Y plotter. This approach has several advantages:

(a) As there was a large number of tests required, continuous curves overcome tedious and time-consuming manual graph plotting.

(b) Bearing stiffness can be obtained relatively accurately from the load/deflection curves.

The following parameters were plotted on an X-Y plotter:

(i) Load/deflection for various speeds

(ii) Shaft locus for various speeds

(iii) Speed/deflection for various loads

(iv) Speed/attitude angle for various loads

16.12 Initial Tests

The coefficient of discharge for the orifices was found by free-jetting the orifices (with the shaft withdrawn) and recording the mass flow rates for various supply pressures.

The isentropic flow for choked conditions is given in Section 2.4.5 as:

$$\dot{m}_T = N C_d^* \frac{\pi d_o^2}{4} \rho_o \left[\frac{2\gamma}{(\gamma-1)RT} \left\{ \left(\frac{p^*}{\rho_o} \right)^{2/\gamma} - \left(\frac{p^*}{\rho_o} \right)^{\frac{\gamma+1}{\gamma}} \right\} \right]$$

$$\frac{p^*}{\rho_o} = \left[\frac{2}{\gamma+1} \right]^{\frac{\gamma}{\gamma-1}}$$

Substituting for $\gamma = 1.4$, $R = 287 \frac{m^2}{sec^2\ ^oK}$, $T = 293^o$ K

gives:

$$\dot{m}_T = 1.87 \times 10^{-4} N C_d^* d_o^2 \frac{\rho_o}{\rho_a}$$

where N = total number of orifices

d_o = orifice diameter (mm)

The coefficient of discharge was obtained by dividing the recorded mass flow with the theoretical mass flow rate to give:

$$C_d^* = \frac{\text{Actual mass flow rate in kg/sec.}}{1.87 \times 10^{-4} N d_o^2 \rho_c/\rho_a}$$

The values of the experimental C_d^* are given below:

P_o/P_a	L/D = 1	L/D = 2
2	0.69	0.72
5	0.71	0.74
8	0.72	0.73

These values correspond to those obtained by the Author in Reference 2.2, where for the orifice diameter of 0.09 mm, C_d^* was found to be in the range 0.73 - 0.74. In this investigation, a mean value of 0.7 was assumed.

17. COMPARISON OF EXPERIMENTAL DATA WITH THEORETICAL PREDICTIONS

17.1 Introduction

In this section, experimental data is compared with theoretical predictions. The various theoretical models have been previously presented in Section 14. The experimental data used for comparison includes that obtained from this study in addition to other published results.

17.2 Experimental Results Obtained from the Study

The experimental results were obtained in the form of continuous curves. The outputs from the appropriate electronic circuitry were connected to the axes of a Bryans 26000 series X-Y plotter.

17.2.1 Experimental Technique

Various bearing characteristics have been investigated by the following techniques:

(i) Load /Deflection

The output from the bearing load transducer circuit was fed into the Y axis of the X-Y plotter; e_{res} into the Y axis. Shaft speed was adjusted to the required value and the bearing was loaded continuously by increasing the pressure in the load cylinder.

(ii) Shaft Locus

The output from the vertical capacitance probes (X') was fed into the Y axis of the X-Y plotter; the output from the horizontal capacitance probes (Y') into the X axis. Shaft speed was adjusted to the required value and the bearing was loaded continuously by increasing the pressure in the load

cylinder. From the diagram produced, the attitude angle and maximum bearing eccentricity could be obtained directly.

(iii) Deflection /Speed

The output from the analogue computer, e_{res} , was fed into the Y axis of the X-Y plotter; the output from the tacho-generator into the X axis. Bearing load was adjusted to the required value and shaft speed increased.

(iv) Attitude Angle /Speed

As above but with the output $\tan^{-1}$ from the analogue computer.

17.2.2 Aerodynamic Performance of Plain Cylindrical Bearings

The experimental and theoretical (finite difference) results for the aerodynamic performance of plain cylindrical bearings are shown in Figures 17.1 and 17.2 for L/D = 1 and 2 respectively. At low eccentricities, the bearing was prone to synchronous whirling. (This was observed on the high - speed storage oscilloscope).

As load was increased, whirling was suppressed due to higher film stiffnesses. This feature has been reported extensively in the literature. Typical references have been made by Sternlicht and Elwell (Ref. 17.1) and McCann (Ref. 17.2).

Up to $\varepsilon \leqslant 0.5$, experimental and theoretical load capacities correlate to within $\pm$ 20% whilst for attitude angle to within 5°.

17.2.3 Aerodynamic Performance of Orifice Bearings

The experimental and theoretical results for the aerodynamic performance of bearings having orifices present are shown in Figures 17.3, 17.4 and 17.5. The theoretical results shown have been calculated by the theoretical

analysis presented in Section 14.1.2 . This assumes that the orifice planes represent atmospheric boundaries which provide a pressure source on the high clearance side of the bearing and a pressure sink on the low clearance side. In other words, the bearing has been assumed to be comprised of three separate elements - a central section and the two outboard sections.

Under low loading conditions, these bearings were prone to synchronous whirling as was the case for the plain cylindrical bearings. When a small load was applied to the bearing, whirling was suppressed.

Up to $\varepsilon = 0.5$ experimental and theoretical load capacities correlate to within 15% and attitude angle to within $\pm 4^{\circ}$. It is pointed out that the theoretical results for load capacity are consistently lower than for experiment. This could be explained by the fact that the row of orifices do not provide a line boundary and/or some restriction is afforded to prevent efficient sinking or pressurising to atmospheric conditions in this plane.

The bearings shown in Figures 17.1 and 17.3 are identical bearings except that for the latter figure holes exist in the bearing wall into which orifices have been press-fitted. The same also for Figure 17.2 and 17.4. The presence of these holes derates the experimental load carrying capacity at $\varepsilon = 0.5$ by the following factors:

L/D	$\frac{\text{load capacity with holes}}{\text{load capacity without holes}}$
1	0.28
2	0.50

17.2.4 Hybrid Performance

The experimental and theoretical results for the aerostatic and hybrid performance are shown in Figures 17.6 to 17.10. The results from two theoretical models are shown - the finite difference solution and the results from the modified superposition method as outlined in previous sections. The theoretical results for the modified superposition method has been calculated using the finite difference solution for the aerostatic condition. The various bearing configurations are shown below:

Figure No.	L/D	P_o/P_a	h_o μm
17.6	1	2	12.3
17.7	2	2	12.7
17.8	"	5	"
17.9	"	8	"
17.10	"	5	17.9

For the aerostatic performance, theoretical and experimental results correlate to within 10% for $\varepsilon \leqslant 0.5$. For the hybrid performance the results show, as expected, that by increasing L/D ratio and/or decreasing supply pressure, increases the aerodynamic effect.

The discrepancies between theoretical and experimental load capacities for $\varepsilon = 0.5$ are tabulated overleaf:

L/D	P_o/P_a	h_o μm	discrepancy*	
			finite difference	modified superposition
1	2	12.3	+ 20% *	+ 10%
2	2	12.7	+ 10%	- 6%
2	5	12.7	+ 6%	+ 1%
2	8	12.7	+ 9%	+ 7%
2	5	17.9	+ 5%	+ 14%

* refers to the maximum discrepancy. The figure of + 20% means that the finite difference solution over-estimated load capacity as compared with experimental values.

The experimental and theoretical values of attitude angle correlate to within $\pm 5^{\circ}$. The theory generally gives predictions lower than that observed experimentally.

17.3 Other Published Data

17.3.1 Powell

A comparison of experimental data obtained by Powell (Ref. 13.7) for central admission bearings with theoretical predictions from this study are shown in Figure 17.11. It can be seen that the finite difference results correlate well with experiment for both aerostatic and hybrid performance. The modified superposition method, based on the aerostatic load capacity from the finite difference solution, predicts a slightly lower hybrid load capacity than that observed experimentally.

The discrepancy between the finite solution and experiment is within 6% for

both aerostatic and hybrid operation. The modified superposition theory and experiment correlate to within 6% for hybrid performance.

17.3.2 Cunningham et.al.

Figure 17.12 shows a comparison between the experimental results obtained by Cunningham et.al. (Ref. 13.8) and the finite difference solution. Figure 17.12 (a) refers to the load deflection characteristics; Figure 17.12 (b) to shaft locus. The finite difference solution correlates well with experiment for both aerostatic and hybrid modes of operation. The discrepancy in load capacity for the aerostatic performance is within 10% and for the hybrid performnace within 15%. Attitude angle is predicted to within 5^{o} at $\varepsilon > 0.2$.

17.3.3 McFarlane and Reason

The experimental data recently presented by McFarlane and Reason (Ref. 13.10) is compared to the finite difference solution in Figure 17.13. Figure 17.13 (a) compares theoretical pressure profiles with experimental results obtained from pressure tappings in a bearing. Theory and experiment correlate to within 8 kN/m^2 (1.2 lbf/in^2) for a supply pressure of 138 kN/m^2(20 lbf/in^2)

Figure 17.13 (b) compares theoretical and experimental results for eccentricity ratios and attitude angle against speed. At aerostatic conditions, theoretical and experimental eccentricity ratios agree to within 0.07 (14%), and for hybrid conditions, to within 0.09 (18%). For all cases, experimental eccentricities are lower than that predicted, which implies that the finite difference solution under-estimates the bearing load capacity. Attitude angle is predicted to within 5^{o} for the complete range of speeds.

17.4 Conclusions

The finite difference solution gives predictions for load carrying capacity within 20% for L/D = 1, 15% for L/D = 1.5 and within 18% for L/D = 2 compared to that measured experimentally by this and other studies for $\varepsilon \leqslant 0.5$. Attitude angle is predicted to within $\pm 5^{o}$.

The modified superposition method, based upon the finite difference solution for the aerostatic performance, gives predictions for hybrid load capacity to within 15% of that measured experimentally up to $\varepsilon = 0.5$.

18. GENERAL CONCLUSIONS

It has been demonstrated that the performance characteristics of aerodynamic, aerostatic and hybrid bearings are accurately predicted from the finite difference analysis.

For plain cylindrical bearings, theory and experiment correlate to within 20% for load capacity up to $\varepsilon = 0.5$.

In the case of an orifice bearing operating aerodynamically, it was assumed that the orifice plane acts as atmospheric boundaries. Theoretical and experimental load capacity correlate to within 15% up to $\varepsilon = 0.5$. Greater accuracy could be obtained if the analysis took account of these holes. A similar analysis to that used for aerostatic conditions could be employed to take account of the source/sink dispersion effects local to these holes. However, the assumptions made in the present study give a reasonable approximation.

For aerostatic and hybrid operation, the type of grid network used in computation accounts largely for the dispersion effects often ignored in previous theoretical modelling. The predictions for aerostatic load capacity up to $\varepsilon = 0.5$ is predicted to within 14% of experimental values, whilst for hybrid operation up to $\varepsilon = 0.5$ predictions are within 20% for L/D = 1, 15% for L/D = 1.5 and 18% for L/D = 2.

The computer results suggest that reverse flow can exist through some orifices at high eccentricities. The analysis used in this study does not take this into account and for this condition, supply pressure is assumed at these orifices. Further refinements could be made in the analysis to account for this effect.

For all modes of operation, the finite difference solution gives predictions for attitude angle within 5^{o}.

An approximate method for the calculation of hybrid performance is outlined. This follows closely that proposed by Powell and involves superposition of aerostatic and aerodynamic load components. It is shown that this method gives predictions within 15% of those obtained from the finite difference analysis. When compared to experimental values, it is shown that the predictions for hybrid load capacity, based on the finite difference solution for the aerostatic load component, are within 14% of those measured experimentally up to $\varepsilon = 0.5$.

Due to its simplicity, this method is a useful design aid. The results give a good approximation for hybrid operation without recourse to lengthy computation.

In contrast, the finite difference solution is particularly useful in the analysis of manufacturing errors such as those discussed in the previous Part . Other instances where this method is more applicable is for the effects of misalignment on the hybrid bearing performance.

PART E

OVERALL CONCLUSIONS

PART E - OVERALL CONCLUSIONS

19. CONCLUSIONS

Various theoretical treatments have been examined in this thesis and compared with experimental data. Where necessary, new data have been presented on bearing characteristics and new design procedures have been proposed.

A method is presented which employs complex potential theory for the analysis of externally pressurised bearings. Using this theory, a corrected line feed model has been obtained from which the influence of the line feed parameters on bearing performance has been demonstrated. The data presented considered a wide range of λ values which is an advancement on the results given by M.T.I. for which one specific value of λ was considered.

Finite difference methods have also been examined. This provides a versatile method for the solution of bearing film pressures, particularly for condition of non-parallel film clearances, such as eccentric journal bearings. Other instances where the finite difference methods are particularly useful is in the analysis of manufacturing errors, such as mis-matched orifices, errors in form or misaligned bearing surfaces.

For the case of journal bearings, the corrected line feed analysis was used to demonstrate the effects of various design changes on aerostatic performances. It was shown that this method gives results to an accuracy of within $\pm$ 15% when compared with experiment.

The results from the complex potential theory and those from the finite difference method were compared to experimental pressure profiles for concentric conditions. It was shown that the bearing film pressures local to the source are accurately predicted by finite difference methods, which validates the modelling technique employed. The finite difference model was shown to give predictions for the aerostatic performance within 10% for load capacity, flow rate, stiffness and restoring torque.

This method was used to examine the effects of manufacturing errors on aerostatic performance. The errors considered included errors in orifice diameter, errors in clearance, mis-matched orifices, form errors, bearing tilt and local burring at the edge of pockets. Each of these errors were examined independently and their effects presented. Also, by accounting for the tolerances in measurement and form, experimental bearings were analysed and a theoretical error band established. It was shown that the experimental results fall within this band. This indicated that differences between theory and experiment can be largely attributed to the effect of manufacturing errors.

The finite difference analysis was extended to include speed effects. For plain cylindrical and hybrid orifice bearings, theory and experiment correlated to within 20% for load capacity up to $\varepsilon = 0.5$ and within 5° for attitude angle. For an orifice bearing operating aerodynamically, it was assumed that the orifice planes act as atmospheric boundaries for which theory and experiment correlated to within 15% up to $\varepsilon = 0.5$. Although greater accuracy could be obtained by improving the analysis to account for the influences of the feed holes, and to account for reverse flow during hybrid operation at high eccentricities, the assumptions made in this study leads to results which give a good approximation to the experimental results.

An approximate design method for the evaluation of hybrid performance has been outlined. This method involves vector addition of the aerostatic and aerodynamic loads and follows closely that proposed by Powell. The difference lies in the calculation of the aerodynamic component. It was shown that this method gives predictions for hybrid load capacity within 15% of those from the more elegant finite difference method and within 14% of experimental values for $\varepsilon \leq 0.5$. As this method can be used without recourse to lengthy computation it is a useful design aid.

20. RECOMMENDATIONS FOR FUTURE WORK

The finite difference method used in this study has been the intermediate relaxation technique. Another method, which has recently been developed at Southampton University, is the A.D.I. scheme. A comparison of the results from these methods has been made in this study.and it has been found that good correlation exists. However, only a limited comparison has been made and a more detailed study is necessary in order to achieve more generalised conclusions. It would also be useful to compare process time necessary for the two methods.

It was found that for hybrid simulations, under relaxation was necessary to prevent numerical instabilities. This technique overcame instabilities but did not represent an optimum to minimise process time. Useful work could be achieved by evaluating the effects of relaxation on computer process time.

For the analysis of an orifice compensated bearing operating in an aerodynamic mode, it was assumed in this study that the orifice planes act as atmospheric boundaries. The finite difference solution applicable for aerodynamic bearings could be modified to account for the effect of the supply holes. The equations relating to the viscous flow from the holes have been presented in this study and with some modification to account for either forward or reverse flow, the effects of these holes on performance characteristics can be determined.

For the hybrid analysis in this study, it was observed that the film pressure immediately below the orifice can exceed the bearing supply pressure in the low clearance side when very high aerodynamic conditions prevail. These can occur at conditions of high eccentricity ratios, high compressibility numbers or low supply pressures. It is assumed in the analysis that the inlet film pressure at the orifices cannot exceed supply pressure conditions and therefore reverse flow

was not accounted for. However, this effect could be included in the analysis with the assumption that the orifice characteristics are identical regardless of the flow direction. This would allow higher pressures to exist at the positions of the orifices than the supply pressure. A higher load capacity would therefore be predicted than that from the existing analysis.

The finite difference solution could also be applied to other bearing geometries such as annular thrust bearings and rectangular thrust bearings. In doing so, the effects of dispersion due to the influence of discrete sources could be determined and, in the case of rectangular thrust bearings, the so-called 'end effects' could be examined.